

Modeling of III-nitride alloys

by *ab-initio* methods

DISSERTATION

zur Erlangung des akademischen Grades
doctor rerum naturalium (Dr. rer. nat.)

FRIEDRICH-SCHILLER-UNIVERSITÄT JENA



seit 1558

vorgelegt dem Rat der Physikalisch-Astronomischen Fakultät
der Friedrich-Schiller-Universität Jena
von M. Sc. Luiz Cláudio de Carvalho
geboren am 31.07.1970 in São João del Rei - MG - Brazil

Jena

Dezember - 2012

Gutachter

1. Prof. Dr. sc. nat. Friedhelm Bechstedt, Friedrich-Schiller-Universität Jena
2. Prof. Dr. rer. nat. Wolf Gero Schmidt, Universität Paderborn
3. Prof. Dra. Luísa Maria Ribeiro Scolfaro, Texas State University, Texas

Tag der Disputation: 4. Dezember 2012

To Tânia, my wife.
Galdino and Zenite, my parents,
Cláudia Luiza and Cátia Regina my sisters.

*"A verdadeira felicidade está,
na própria casa, entre as alegrias da família"*

Tolstoi

Contents

	Page
1 Introduction	3
2 First-principles methods and approximations	7
2.1 Ground-state properties	8
2.1.1 Many-body problem	8
2.1.2 Density functional theory (DFT)	9
2.1.2.1 Hohenberg-Kohn theorems	9
2.1.2.2 Kohn-Sham method	12
2.1.2.3 Spin-polarized DFT	14
2.1.3 Exchange and correlation	15
2.1.3.1 Local density approximation (LDA)	16
2.1.3.2 Generalized gradient approximation (GGA)	16
2.1.3.3 AM05 functional	17
2.1.3.4 Hybrid functional (HSE)	19
2.1.3.5 LDA+ U method	20
2.2 Excited electronic state properties	20
2.2.1 Green's function	21
2.2.2 Self-energy	22
2.2.3 Bethe-Salpeter equation (BSE)	25
2.2.4 Excitonic Hamiltonian	26
2.2.5 Dielectric function	26
2.3 Alloy description	27
2.3.1 Cluster expansion	27
2.3.2 Generalized Quasichemical Approximation	28
2.3.3 Limiting cases	30
2.3.3.1 Strict-regular solution model	30
2.3.3.2 Microscopic decomposition model	30
2.4 Numerical approaches	31
2.4.1 PAW method	31
2.4.2 Brillouin zone sampling	33
2.4.3 Exchange and correlation	34
2.4.4 HSE06 hybrid functional	35
2.4.5 Spin-orbit interaction and cristal-field splitting	35
2.4.6 Screening in W	35
2.4.7 Number of bands	36
2.4.8 Equation of state	36

2.4.9	LDA+ $U+\Delta$ scheme	36
2.4.10	Excitonic effects	37
3	AlN, GaN and InN polytypes as binary end components: Influence of exchange and correlation on structural and electronic properties	38
3.1	Energetic, structural and elastic ground-state parameters	40
3.2	Quasiparticle electronic structure	41
3.2.1	Band structures and DOS	42
3.2.2	Band alignment and cubic inclusion in wurtzitic structures	43
3.2.3	Fundamental gaps and their volume/pressure dependence	46
3.2.4	Valence band splittings and spin-orbit interaction	48
3.2.5	Band dispersions	51
3.2.6	Effective masses	52
4	InAlN and InGaN alloys: Energetics, structures, and cation distribution	57
4.1	Cluster approach and alloy statistics	58
4.2	Structural and thermodynamic properties	58
4.3	Bowing parameters	62
4.4	Lattice parameters and bulk modulus	62
5	InAlN and InGaN alloys: Quasiparticle electronic structure	65
5.1	Energy zero and alignment	66
5.2	Density of states	66
5.3	Aproximate band edges	68
5.4	Fundamental gap and its bowing	69
6	InAlN and InGaN alloys: Excitonic effects and optical properties	73
6.1	Frequency-dependent dielectric function	75
6.2	LDA+ $U+\Delta$ as start approach	75
6.3	Spectra of the binary-end components	76
6.4	Overall absorption spectra	78
6.5	Interband critical points	80
6.6	Excitonic effects	83
6.7	Dielectric properties	85
7	Summary	87
8	Future perspectives	90
A	Appendix	A.1
A.1	Atomic arrangement of the 22 cluster classes	A.1
A.2	Cluster expansion for the wurtzite alloys	A.2
A.3	Parameters of calculations	A.3
A.3.1	Scissors operator (Δ)	A.3
	Bibliography	92

1

Introduction

"Sabemos o que somos, mas não sabemos o que poderemos ser."

William Shakespeare

Since the first experimental findings of semiconducting effects in the early years of the 19th century, the research for new materials with interesting electric and optical properties has become an important field in both theoretical and experimental physics. Although noticed in the literature that the term *semiconducting* or *materials of semiconducting nature* had been already used by Alessandro Volta [1, 2], one century before, only after the experimental discovery of basic effects – *Semiconducting properties in Galena* (PbS) by T. J. Seebeck (1821) [3] and – *Dependence of the temperature with conductivity in Silver Sulfide* (Ag₂S) by M. Faraday (1833)[4] the new field had, indeed, an impetus and was established in the scientific community. From there, the development of the research on semiconductors was mainly driven by experimental findings. By 1885, three important properties of the semiconductors had been observed - *the rectification of alternating current* [5], *the generation of a photo-voltage* [6], and *the increase of conductivity in the presence of light* [7]. These findings, although notable, were not immediately appreciated and remained unexplained for long time due to the lack of consistent theories.

By the end of the 19th century and the beginning of the 20th century, J. J. Thomson in the Cavendish Laboratory in Cambridge and Rutherford in Manchester, respectively, discovered *the electron* and its positive counterpart, *the nuclei*. Their findings caused great impact on the scientific community and gave rise to questions that could be answered only with the formulation of a new theory. Then a new era considering *the electron as a fundamental particle constituent in matter* started and emerged into a new research field, *electronic structure of matter*. Several theories were developed and new experiments were performed in order to explain the phenomena of conduction of electricity based on electrons. In fact, this field

became so comprehensive and complex that, in 1914, J. Königsberger suggested to divide solid-state materials in three different classes[1, 8]. However, only in the 1930s with the work of A. W. Wilson [9, 10] all crystals were classified into the three classes metals, semiconductors, and insulators according to their conductivity.

For a long time, the theoretical description and understanding of the electronic structure of atoms as well as molecules and solids were very troublesome and obscure. Significant advantages occurred especially in the early years of the 20th century when theoretical physics overcame the critical divergences and countless doubts on the explanation of the electrical conduction in matter. In 1911 Niels Bohr, based on Planck's postulate of 1900, investigated the electronic structure of atoms and the radiation emanating from them. As a consequence he discovered basic laws of a new theory – *the quantum mechanics*. Later, between 1923 and 1925, after the advent of Bohr's idea, Louis de Broglie, Erwin Schrödinger and Werner Heisenberg developed a novel theoretical formalism that revolutionized the physics and has become one of the pillars of modern physics. Until nowadays, the quantum mechanics became a key role in the solution of many physical phenomena, especially for many-body systems such as matter, that the classical physics has not been able to explain sufficiently. Concomitantly, significant progress was possible in understanding of the electronic structure of atoms, molecules and solids.

Interestingly, indeed in the late thirties of the last century, when the theoretical and experimental advances of the basic research on new materials were enhanced and established, the semiconductor technology took a giant leap forward. High investments occurred during World War II, especially in the research for semiconducting properties of germanium and silicon for application in radar technology. Already at that time, researchers started to grow group-IV semiconductors with a high degree of purity. As a consequence, the transistor based on Ge has been discovered [11]. In the 1960s and 1970s silicon-based electronic circuits with an increasing integration according to Moore's law have been developed. This fact was the starting point for an ongoing revolution in society, economy, and, finally, also of theoretical physics. A new field, computational physics is rapidly developing.

This also holds for theoretical studies of the electronic structure of matter. However, the progress in the development of the computational hardware was also accompanied by rapid advances in computational methods. Parameter-free calculations based on *ab-initio* methods, for instance the density functional theory (DFT)[12, 13] or many-body perturbation theory (MBPT)[14], become a promising complement to experiments. Theoretical studies allow the investigation of not only crystal structures but also arbitrary arrangements of atoms. Now they can help to understand or predict properties of many materials using feasible methods. Nevertheless, the solution of the underlying many-body problem and the treatment of correlation among electrons were, are, and will be challenges for the theoretical description of the physics of electronic structure. Several theoretical and numerical approaches have been

developed in order to describe the electronic properties of the solids including the correlation among electrons. DFT together with local or semilocal approximations of exchange and correlation (XC) is now the method of choice to treat energetic, structural and elastic properties of materials. The most successful approximations used to compute the electronic excited-state properties of solids such as single-particle band structures and related spectra are based on the concept of *quasiparticles* (QPs) whose mathematical description is based on studies of the single-particle *Green function* (G). The exact determination of G requires complete knowledge of the QP *self-energy* (Σ) which, however, can be calculated only approximately in practice. Because of the high computational costs, the enormous progress in the application of such many-body methods in the last 15 years was only possible with new generations of computers and silicon-based processors.

About 20 years after the first silicon transistor a new group of semiconducting materials, the group-III nitrides and their alloys, stand out due to their promising properties for application in electronic, especially optoelectronic, semiconductor devices such as light emitting diodes (LEDs), laser diodes (LDs), high-power amplifiers, and solar cells. Aluminum nitride (AlN), gallium nitride (GaN) and indium nitride (InN) nowadays play a key role in devices operating in the spectral range from the deep ultraviolet to the near infrared wavelength region. Currently, the high quality of the sample growth by molecular beam epitaxy (MBE) or metalorganic vapor phase epitaxy (MOVPE)[15–17] provides the possibility to combine binary III-nitrides in ternary alloy systems $\text{Al}_x\text{Ga}_{1-x}\text{N}$, $\text{In}_x\text{Ga}_{1-x}\text{N}$, and $\text{In}_x\text{Al}_{1-x}\text{N}$ whose direct band gap energies in wurtzite (wz) structures can be tailored from ~ 0.64 eV (InN)[15–17] to 3.52 eV (GaN) [18] or 6.24 eV (AlN) [18] at room temperature. These alloy systems are promising candidates for fabrication of highly-efficient multijunction solar cells [19], terahertz quantum cascade lasers operating at room temperature via intersubband transitions [19], chemical sensors [20], and even green laser diodes by the use of In-rich $\text{In}_x\text{Ga}_{1-x}\text{N}$ quantum wells (QWs)[20].

Among these ascending III-nitride ternary alloys, particular attention has been addressed to the $\text{In}_x\text{Ga}_{1-x}\text{N}$ and $\text{In}_x\text{Al}_{1-x}\text{N}$ systems, owing their novel properties that cover the gaps left by the binary compounds, especially for band-gap engineering in optoelectronic devices. However, so far, the majority of their properties, e. g. structural, electronic and optical ones, are not very well understood and fully explored. This specially holds for the relation of the microscopic structure, e. g. the cation distribution in the alloys, to the resulting properties. Despite the fact that recently research groups [21] have achieved "direct" green laser diodes based on $\text{In}_x\text{Ga}_{1-x}\text{N}$ alloys, the performance of these devices is still lower when compared with the red and blue semiconductor LD counterparts. In order to achieve high performance of green LDs, Hiroaki et al. [22] suggest that the research should focus on improving the internal quantum efficiency (IQE) of green spontaneous emission from $\text{In}_x\text{Ga}_{1-x}\text{N}$ quantum wells. Furthermore, for high electron mobility transistors (HEMTs) based on $\text{In}_x\text{Al}_{1-x}\text{N}$, high

power operation has been demonstrated using GaN active layers without lattice mismatch in an InN composition of about 17% [23]. Then, the properties of the applied alloy layers need a deeper understanding in order to be better explored.

Despite to the already explored wide range of interesting properties and applications, still there are many challenges for theoretical and experimental researchers on In-containing ternary nitride alloys still remain. It is known [24] that emission efficiency of LEDs and LDs can be varied as a function of the In-atom molar fraction in the III-nitride active layers [25]. Notwithstanding, the high density of defects, e. g. threading dislocations, lattice mismatch, atom clustering, and segregation occurring in the active layers still reduce the performance of the devices. The intense research and the commercial interest in the nitride semiconductors will, however, give rise to substantial further progress. For instance, a remarkable breakthrough in the growth of InN films by means of molecular beam epitaxy (MBE) has been recently achieved which makes luminescence and absorption studies of pure InN possible. Theory and computational physics, however, also give rise to significant progress in the field. One prominent example in the last years was the theoretical prediction of an InN gap of about 0.7 eV and its experimental confirmation [15–17]. However, still electronic band parameters such as fundamental gaps, effective electron and hole masses, valence-band dispersions (as well as their variation with strain), and wave-vector-induced band splittings due to spin-orbit interaction are less precisely known for the binary nitride materials. Moreover, the nitride alloys are still a playground for theoretical numerical methods.

The present work is motivated to bridge the lack of knowledge for group-III nitrides and their alloys. It is based on systematic theoretical studies using state-of-the-art of *ab-initio* methods and theoretical spectroscopy techniques to describe the properties of ground and excited states of these compounds and their alloys. In chapter 2, the fundamental methods and approximations are described. All formalisms necessary to predict and understand the properties of the semiconducting materials under consideration are described. In chapter 3, different XC functionals and QP approach are used to obtain structural and electronic properties of binary AlN, GaN, and InN polytypes. The properties of these binary compounds combined in different ternary alloys are described in chapters 4, 5, and 6. Pseudoternary isostructural $\text{In}_x\text{Ga}_{1-x}\text{N}$ and $\text{In}_x\text{Al}_{1-x}\text{N}$ alloys are analysed for wurtzitic starting geometries. The influence of the cation distribution in the alloys on energetics, geometries and electronic structures is studied. The modeling covers different distributions of In and Ga/Al atoms on the cation sublattices in order to simulate different growth conditions. The electronic properties, especially the fundamental gaps and their bowing are investigated in chapter 5. The chapter 6 is focused on optical properties and excitonic effects. The DFs, absorption spectra, and dielectric constants are studied in details. Results of the QP method and the solution of the Bethe-Salpeter equation are combined with statistical treatment of the alloys. Finally, chapters 7 and 8 contain a brief summary and future perspectives.

2

First-principles methods and approximations

*"Estou convencido das minhas
próprias limitações - e esta convicção
é minha força "*

Mahatma Gandhi

The great power of the most modern first-principles methods and approximations on electronic structure of matter are based on the density functional theory for the ground state of an inhomogeneous electron gas [12, 13] and Hedin's *GW* approximation (GWA) for the XC self-energy of excited electrons. [26] It is due their asset to provide new insights and also a better understanding of relevant critical problems in solid-state physics, particularly semi-conducting bulk crystals, surfaces, nanostructures, and alloys. In addition, taken together they have created a new perspective of research, not only in solid-state but in all fields of physics making it possible to treat many body interactions in real electron systems, as found in nature, as well as idealized model problems for ground and excited states.

With the advance in computing technology that occurred during the last decades, these methods and approximations have consolidated to be reliable and tractable tools in the field of theoretical condensed matter physics. However, even with the ample successes of theses theoretical approaches, some challenges still remain. Actually, e. g., the biggest challenge for theoretical research in electronic structure is to provide universal methods that accurately describe the electronic structure and related properties of systems with arbitrary bonding, including Van der Waals and hydrogen-bridge bonding [27, 28].

This chapter reports a brief discussion of the first-principles methods and approximations applied to modeling electronic ground states and excited state properties of the group-III nitrides alloys.

2.1 Ground-state properties

2.1.1 Many-body problem

In quantum mechanics, all possible information about a given system is contained in their wavefunction Ψ . In atom-, molecule- and solid-like systems, the nuclear degrees of freedom are taken into account only in the form of an external potential $v_{ext}(\mathbf{r})$ acting on the electron at position \mathbf{r} . It contains the positions \mathbf{R}_i of the nuclei if several nuclei are present or only one. The so-called Born-Oppenheimer approximation is applied [29]. A time independent single-particle state $\psi(\mathbf{r})$ depends only on the coordinate \mathbf{r} of an electron and can be calculated directly from the Schrödinger equation,

$$H\psi(\mathbf{r}) = \left[-\frac{\hbar^2}{2m}\nabla^2 + v(\mathbf{r}) \right] \psi(\mathbf{r}) = \varepsilon\psi(\mathbf{r}). \quad (2.1)$$

Here, H is the Hamiltonian for a single electron, ε the eigenvalues of the system, and $v(\mathbf{r})$ is the potential acting on the electron. It contains the external potential. However, for a system with N -electrons a more accurate and realistic calculation of the electronic properties must be the Schrödinger equation for N -particles that accounts for all N -electrons of the system as

$$\hat{H}\Psi_0(\mathbf{r}) = \left[\sum_{i=1}^N \left(-\frac{\hbar^2}{2m}\nabla_i^2 + v(\mathbf{r}_i) \right) + \sum_{i<j} U(\mathbf{r}_i, \mathbf{r}_j) \right] \Psi_0(\mathbf{r}_1, \dots, \mathbf{r}_N) = E\Psi_0(\mathbf{r}_1, \dots, \mathbf{r}_N). \quad (2.2)$$

N is the total number of electrons and $U(\mathbf{r}_i, \mathbf{r}_j)$ accounts for the Coulomb interaction between the electrons which correlates the motion of the electrons, such that

$$\hat{U} = \sum_{i<j} U(\mathbf{r}_i, \mathbf{r}_j) = \sum_{i<j} v(\mathbf{r}_i, \mathbf{r}_j), \quad (2.3)$$

where $v(\mathbf{r}) = \frac{e^2}{|\mathbf{r}|}$ and e is electron's charge. Now, the external potential $v(\mathbf{r})$ depends on the positions \mathbf{R}_i of all nuclei in the system. It may be the equilibrium coordinates or arbitrary ones.

As a consequence, the so-called *many-body problem* for N -electrons emerges. The exact description of $\Psi_0(\mathbf{r})$ in real-space representation is computationally complex. $\Psi_0(\mathbf{r})$ becomes a function of $3N$ coupled spatial coordinates (neglecting spin, and taking $\Psi_0(\mathbf{r})$ to be real). For instance, in a macroscopic system whose the number of electrons N is $\approx 10^{23}$ electrons/cm³ (Avogadro's number) the solution of Eq. (2.2) becomes impossible. Even using symmetry conditions the wavefunction remains unaccessible for real systems and the solution of Eq. (2.2) should be approximate.

2.1.2 Density functional theory (DFT)

Many powerful theoretical methods in order to solve exactly or approximately Eq. (2.2) have been developed during decades of efforts handling with the *many-body problem*. Though the solution of Eq. (2.2) has been possible for simple systems, e. g., hydrogen atoms, for many-electron systems such as solids the exact description of their electronic structure by means of Eq. (2.2) remains somewhat challenging or impossible. According W. Kohn [30], it holds owing the exponential increase of parameters and informations contained in the interacting N -electrons wavefunction that cannot adequately be described without $\approx 10^{23}$ parameters, and it has also the complication of possessing a phase as well as a magnitude.

A modern theory called *Density Functional Theory* (DFT), based on Hohenberg-Kohn theorems [12], is actually the simplest and most effective state-of-the-art method that overcomes the *many-body problem* for ground-state properties. It is based on ground-state electronic density $\rho_0(\mathbf{r})$ constituting a special role as "*basic variable*" of the problem. Thus, all information and properties of an electronic system can be considered as unique functionals of $\rho_0(\mathbf{r})$ [31] providing an enormous simplification of the problem. However, even as an exact theory for ground-state properties, the Hohenberg-Kohn theorems [12] do not provide an explicit mathematical form for systems of N interacting electrons influenced by $v_{ext}(\mathbf{r})$, and approximations are still necessary.

The DFT's fundamentals of quantum systems started in the early twentieth century with L. H. Thomas and E. Fermi. [32, 33] Their theories predicted the electronic kinetic energy per unit volume of an idealized electron system following the ideas of Lord Kelvin and Paul Drude of treating electrons in metal as electrons gas. The Thomas-Fermi models were idealized for a homogeneous non-interacting electron-gas, whose electronic density $\rho_0(\mathbf{r})$ is the same in any point of the system. This approximation was, however, the most rudimentary and crude form of DFT due to neglect XC interaction among electrons, becoming of little avail for complex systems. Years later, concomitantly, Dirac [34] introduced XC formulating the local approximation for exchange and Slater showed that the Hartree-Fock method applied to metals gives the exchange energy density proportional to $\rho^{\frac{1}{3}}$ [35].

By the 1964's-1965's the works "*Inhomogeneous Electron Gas*" of Hohenberg-Kohn [12] and "*Self-Consistent Equations including Exchange and Correlation Effects*" of Kohn-Sham [13] were the pillars of contemporary DFT. Its formalism was developed based on Hohenberg-Kohn and Kohn-Sham concepts and implemented in several codes largely used in solid state physics until now.

2.1.2.1 Hohenberg-Kohn theorems

The concept of Hohenberg and Kohn is the fundament for an exact theory describing the ground-state of N interacting electrons. Two theorems have made possible this theory in order to find the exact $\rho_0(\mathbf{r})$ and total energy E_0 of N interacting electrons in $v_{ext}(\mathbf{r})$ (cf. Eq.

(2.2) and Eq. (2.3)). In their first theorem, Hohenberg and Kohn prove the equivalence of $\Psi_0(\mathbf{r})$ and $\rho_0(\mathbf{r})$ for any system consisting of electrons moving under the influence of $v_{ext}(\mathbf{r})$. In other words, the ground-state $\rho_0(\mathbf{r})$ and the ground-state $\Psi_0(\mathbf{r})$ can be used alternatively as full description of the ground state of the system. With that, Hohenberg-Kohn mean that, if the density of electrons [31]

$$\rho_0(\mathbf{r}) = \frac{\langle \Psi_0(\mathbf{r}) | \hat{\rho} | \Psi_0(\mathbf{r}) \rangle}{\langle \Psi_0(\mathbf{r}) | \Psi_0(\mathbf{r}) \rangle} = N \frac{\int d^3 r_2 \cdots d^3 r_N \hat{\rho}(\mathbf{r}) |\Psi_0(\mathbf{r}, \dots, \mathbf{r}_N)|^2}{\int d^3 r_1 d^3 r_2 \cdots d^3 r_N |\Psi_0(\mathbf{r}_1, \dots, \mathbf{r}_N)|^2}, \quad (2.4)$$

and the total energy is the expectation value of the Hamiltonian

$$E_0 = \frac{\langle \Psi_0(\mathbf{r}) | \hat{H} | \Psi_0(\mathbf{r}) \rangle}{\langle \Psi_0(\mathbf{r}) | \Psi_0(\mathbf{r}) \rangle} \equiv \langle \hat{H} \rangle = \langle \hat{T} \rangle + \langle \hat{U} \rangle + \int d^3 r v_{ext}(\mathbf{r}) \rho_0(\mathbf{r}), \quad (2.5)$$

where the expectation value of the external potential is explicitly written as integral over $\rho_0(\mathbf{r})$. For the proof one can suppose in a opposite way. We consider two different external potentials $v_{ext}(\mathbf{r})$ and $v'_{ext}(\mathbf{r})$ that differ from each other by more than a constant and lead to the same ground-state $\rho_0(\mathbf{r})$. These two potentials $v_{ext}(\mathbf{r})$ and $v'_{ext}(\mathbf{r})$, however, lead to two different Hamiltonians \hat{H} and \hat{H}' that have ground-state wave functions $\Psi_0(\mathbf{r})$ and $\Psi'_0(\mathbf{r})$ that, by hypothesis, describe the same ground-state $\rho_0(\mathbf{r})$. Then, since $\Psi'_0(\mathbf{r})$ does not describe the ground state of \hat{H} ,

$$E_0 = \langle \Psi_0(\mathbf{r}) | \hat{H} | \Psi_0(\mathbf{r}) \rangle < \langle \Psi'_0(\mathbf{r}) | \hat{H} | \Psi'_0(\mathbf{r}) \rangle. \quad (2.6)$$

From the last term in Eq. (2.6) and assuming that the ground state is non-degenerate, the inequality strictly holds. Due the identical $\rho_0(\mathbf{r})$ for the two Hamiltonians, one can write the expectation value in Eq. (2.6) as

$$\begin{aligned} \langle \Psi'_0(\mathbf{r}) | \hat{H} | \Psi'_0(\mathbf{r}) \rangle &= \langle \Psi'_0(\mathbf{r}) | \hat{H}' | \Psi'_0(\mathbf{r}) \rangle + \langle \Psi'_0(\mathbf{r}) | \hat{H} - \hat{H}' | \Psi'_0(\mathbf{r}) \rangle \\ &= E'_0 + \int d^3 r \left[v_{ext}(\mathbf{r}) - v'_{ext}(\mathbf{r}) \right] \rho_0(\mathbf{r}). \end{aligned} \quad (2.7)$$

In Eq. (2.7), the difference among \hat{H} and \hat{H}' is also an operator. Therefore its matrix elements can be expressed exactly via the electron density $\rho_0(\mathbf{r})$ corresponding to $\Psi'_0(\mathbf{r})$, and Eq. (2.6) can be written as

$$E_0 < E'_0 + \int d^3 r \left[v_{ext}(\mathbf{r}) - v'_{ext}(\mathbf{r}) \right] \rho_0(\mathbf{r}). \quad (2.8)$$

Similarly we can write E'_0 as

$$E'_0 < E_0 + \int d^3 r \left[v'_{ext}(\mathbf{r}) - v_{ext}(\mathbf{r}) \right] \rho_0(\mathbf{r}). \quad (2.9)$$

Adding Eq. (2.8) and Eq. (2.9) one finds the following inconsistency,

$$E_0 + E'_0 < E'_0 + E_0. \quad (2.10)$$

From Eq. (2.10), by contradiction, one concludes that the same density $\rho_0(\mathbf{r})$ can not satisfy different external potentials. Then, $v_{ext}(\mathbf{r})$ is uniquely determined by $\rho_0(\mathbf{r})$ to within a constant. Therefore, it means that $\rho_0(\mathbf{r})$ can be taken to be the principal variable. On the second theorem the density $\rho(\mathbf{r})$ that minimizes the energy E_0 of the system is the exact $\rho_0(\mathbf{r})$. In other words, the E_0 that is obtained from the $\rho_0(\mathbf{r})$ is the lowest energy compared to any other density $\rho(\mathbf{r})$. It can be shown that the energy E as a functional of the electron density $\rho(\mathbf{r})$ can be written in terms of the $v_{ext}(\mathbf{r})$ as

$$E[\rho(\mathbf{r})] = F[\rho(\mathbf{r})] + \int d^3r \rho(\mathbf{r}) v_{ext}(\mathbf{r}), \quad (2.11)$$

where $F[\rho(\mathbf{r})]$ is an *unknown* universal functional of the density $\rho(\mathbf{r})$ that includes all internal energies, kinetic and potential, of the interacting electron system, i. e., according Eq. (2.5) and (2.11)

$$F[\rho(\mathbf{r})] = \langle \hat{T} \rangle + \langle \hat{U} \rangle \quad (2.12)$$

with $\langle \hat{T} \rangle$ the kinetic energy of the system. From the first theorem, $\Psi_0(\mathbf{r})$ is a functional of the $\rho_0(\mathbf{r})$, then, the expectation value of $\hat{F} = \langle \hat{T} \rangle + \langle \hat{U} \rangle$ is also a functional of $\rho_0(\mathbf{r})$, i. e.,

$$F[\rho_0(\mathbf{r})] = \langle \Psi_0(\mathbf{r}) | \hat{F} | \Psi_0(\mathbf{r}) \rangle. \quad (2.13)$$

Writing Eq. (2.11) as a functional of density $\rho'(\mathbf{r})$ we thus have

$$E[\rho'(\mathbf{r})] = F[\rho'(\mathbf{r})] + \int d^3r \rho'(\mathbf{r}) v_{ext}(\mathbf{r}). \quad (2.14)$$

According to the variational principle and taking into account that,

$$E[\rho_0(\mathbf{r})] = \langle \Psi_0(\mathbf{r}) | \hat{H} | \Psi_0(\mathbf{r}) \rangle \quad (2.15)$$

and

$$\hat{H} = \hat{F} + \hat{v}_{ext} \quad (2.16)$$

we obtain

$$\langle \Psi'(\mathbf{r}) | \hat{F} | \Psi'(\mathbf{r}) \rangle + \langle \Psi'(\mathbf{r}) | \hat{v}_{ext} | \Psi'(\mathbf{r}) \rangle > \langle \Psi_0(\mathbf{r}) | \hat{F} | \Psi_0(\mathbf{r}) \rangle + \langle \Psi_0(\mathbf{r}) | \hat{v}_{ext} | \Psi_0(\mathbf{r}) \rangle. \quad (2.17)$$

Combining Eq. (2.13) with Eq. (2.17) one obtains

$$\begin{aligned} F[\rho'(\mathbf{r})] + \langle \Psi'(\mathbf{r}) | \hat{v}_{ext} | \Psi'(\mathbf{r}) \rangle &= F[\rho'(\mathbf{r})] + \int d^3r \rho'(\mathbf{r}) v_{ext}(\mathbf{r}) > \\ F[\rho_0(\mathbf{r})] + \langle \Psi_0(\mathbf{r}) | \hat{v}_{ext} | \Psi_0(\mathbf{r}) \rangle &= F[\rho_0(\mathbf{r})] + \int d^3r \rho_0(\mathbf{r}) v_{ext}(\mathbf{r}). \end{aligned} \quad (2.18)$$

From Eq. (2.18) and Eq. (2.14) one identify the inequality,

$$E[\rho'(\mathbf{r})] > E[\rho_0(\mathbf{r})]. \quad (2.19)$$

Thus, the ground-state density $\rho_0(\mathbf{r})$ minimize the functional $E[\rho_0(\mathbf{r})]$ and the minimum is the ground-state electronic energy.

2.1.2.2 Kohn-Sham method

The realistic and practical treatment of DFT was provided by Kohn and Sham in 1965 [13]. Their *ansatz* was a formulation of DFT that maps the problem of N interacting electrons using a fictitious system of N non-interacting "electrons" moving in an effective potential so-called Kohn-Sham potential ($\nu_{KS}(\mathbf{r})$) [26]. This $\nu_{KS}(\mathbf{r})$ was constructed in such way that the $\rho_{KS}(\mathbf{r})$ of fictitious N non-interacting "electrons" is the same $\rho_0(\mathbf{r})$ of N interacting electrons. Otherwise, the two systems are directly related by the same electron density $\rho_{KS}(\mathbf{r}) = \rho_0(\mathbf{r})$. However, the $\nu_{KS}(\mathbf{r})$ and $\nu(\mathbf{r})$ are not the same. These fundamentals provide a set of independent-fictitious "electron" equations for the fictitious Kohn-Sham system that can be solved exactly [31].

The Thomas-Fermi model, as said before, fails to provide the total kinetic energy as a functional of density $T[\rho(\mathbf{r})]$. Indeed, the most complete model describing the total kinetic energy $T[\rho(\mathbf{r})]$ of one system is that which accounted by the kinetic energy of non-interacting "electrons" ($T_{KS}[\rho(\mathbf{r})]$) and the difference between the total kinetic energy and the kinetic energy of non-interacting "electrons". The remaining part taken by that difference gives a contribution to electron correlation,

$$T_c[\rho(\mathbf{r})] = T[\rho(\mathbf{r})] - T_{KS}[\rho(\mathbf{r})]. \quad (2.20)$$

However, $T_{KS}[\rho(\mathbf{r})]$ is not exact known as a functional of $\rho(\mathbf{r})$ but can be expressed in terms of single-particle orbitals $\phi_i(\mathbf{r})$ so-called Kohn-Sham orbital of non-interacting system with density $\rho(\mathbf{r})$. The total kinetic energy of this system is given by the sum over all individual kinetic energies [36] as

$$T_{KS}[\rho(\mathbf{r})] = -\frac{\hbar^2}{2m} \sum_{i=1}^N \int d^3r \phi_i^*(\mathbf{r}) \nabla^2 \phi_i(\mathbf{r}). \quad (2.21)$$

The Eq. (2.21) is an implicit equation related to $\rho(\mathbf{r})$, but explicit in orbital functional, since the orbitals ϕ_i are functionals of $\rho(\mathbf{r})$. Thus, the kinetic energy can be expressed as

$$T_{KS}[\rho(\mathbf{r})] = T_{KS}[\phi_i[\rho(\mathbf{r})]]. \quad (2.22)$$

Here, $T_{KS}[\rho(\mathbf{r})]$ depends on the complete set of occupied orbitals ϕ_i in that each orbital is a functional of $\rho(\mathbf{r})$. Then, it follows from Eqs. (2.11) and (2.12) that, we have

$$E[\rho(\mathbf{r})] = T[\rho(\mathbf{r})] + U[\rho(\mathbf{r})] + v[\rho(\mathbf{r})] \quad (2.23)$$

or,

$$E[\rho(\mathbf{r})] = T_{KS}[\phi_i[\rho(\mathbf{r})]] + U_H[\rho(\mathbf{r})] + E_{xc}[\rho(\mathbf{r})] + v[\rho(\mathbf{r})], \quad (2.24)$$

with

$$E_{xc}[\rho(\mathbf{r})] = U[\rho(\mathbf{r})] - U_H[\rho(\mathbf{r})] + T_c[\rho(\mathbf{r})] \quad (2.25)$$

where the exchange-correlation energy $E_{xc}[\rho(\mathbf{r})]$ contains T_c (cf. Eq. (2.20)) energy and the classical Hartree energy $U_H[\rho(\mathbf{r})]$ of the electrons is introduced.

From Eq. (2.24) T_{KS} is not a direct functional of $\rho(\mathbf{r})$. Its minimization directly with respect $\rho(\mathbf{r})$ is not possible. However, the Kohn-Sham method [13] is a tool that apply the minimization via functional derivation of Eq. (2.24) by

$$\frac{\delta E[\rho(\mathbf{r})]}{\delta \rho(\mathbf{r})} = \frac{\delta T_{KS}[\phi_i[\rho(\mathbf{r})]]}{\delta \rho(\mathbf{r})} + v_H(\mathbf{r}) + v_{xc}(\mathbf{r}) + v_{ext}(\mathbf{r}) = 0, \quad (2.26)$$

where $v_H(\mathbf{r})$ is the Hartree potential defined by

$$v_H(\mathbf{r}) = e^2 \int d^3 r' \frac{\rho(\mathbf{r}')}{|\mathbf{r} - \mathbf{r}'|} \quad (2.27)$$

that describes the Coulomb repulsion between the electrons. In Eq. (2.26) the XC potential ($v_{xc}(\mathbf{r})$) can be formally defined as a functional derivative of the exchange-correlation energy $\frac{\delta E_{xc}[\rho(\mathbf{r})]}{\delta \rho(\mathbf{r})}$. However, that functional derivative has no explicit form and approximations are necessary.

According Kohn-Sham, if ones consider a non-interacting "electrons" system moving in a potential $v_{KS}(\mathbf{r})$, the procedure is simple since the electron-electron does not explicitly occur due non-interacting "electrons". Then,

$$\begin{aligned} \frac{\delta E[\rho(\mathbf{r})]}{\delta \rho(\mathbf{r})} &= \frac{\delta T_{KS}[\rho(\mathbf{r})]}{\delta \rho(\mathbf{r})} + \frac{\delta v_{KS}[\rho(\mathbf{r})]}{\delta \rho(\mathbf{r})} \\ &= \frac{\delta T_{KS}[\rho(\mathbf{r})]}{\delta \rho(\mathbf{r})} + v_{KS}(\mathbf{r}) \\ &= 0. \end{aligned} \quad (2.28)$$

If we assume that the potential $v_{KS}(\mathbf{r})$ containing the sum

$$v_{KS}(\mathbf{r}) = v_{ext}(\mathbf{r}) + v_H(\mathbf{r}) + v_{xc}(\mathbf{r}), \quad (2.29)$$

the Eqs. (2.26) and (2.28) have the same solution and

$$\rho_{KS}(\mathbf{r}) \equiv \rho_0(\mathbf{r}) \equiv \rho(\mathbf{r}). \quad (2.30)$$

Clearly the solution of Eq. (2.26) and Eq. (2.28) also points out that one can compute $\rho(\mathbf{r})$ described by Eq. (2.2) solving the equations of a system of non-interacting "electrons" in $v_{KS}(\mathbf{r})$.

The Schrödinger-like equation to find the orbitals $\phi_i(\mathbf{r})$ is the Kohn-Sham equation

$$\left[-\frac{\hbar^2}{2m}\nabla^2 + v_{KS}(\mathbf{r}) \right] \phi_i(\mathbf{r}) = \varepsilon_i \phi_i(\mathbf{r}), \quad (2.31)$$

where ε_i represent Lagrange multipliers, which guarantee that the wave functions are normalized. For a Kohn-Sham system of non-interacting "electrons" the equation

$$\rho(\mathbf{r}) \equiv \rho_{KS}(\mathbf{r}) = \sum_i^N |\phi_i(\mathbf{r})|^2 \quad (2.32)$$

and Eqs. (2.28)-(2.31) are considered, with the constrain (cf. Eq. (2.29)) Kohn-Sham[13] equations. This procedure replaces the problem of minimizations of the total energy of a system of N interacting electrons by that solving the Schrödinger equation of a system of non-interacting "electrons".[26, 31, 36]

2.1.2.3 Spin-polarized DFT

Spin-polarized calculations within the framework of DFT constitute a powerful tool in order to describe the magnetic properties of matter. So far, we have not taken spin into account, only solution for single electron in a non-relativistic Hamiltonian.

In spin-density DFT, the two basic variables, electronic density $\rho(\mathbf{r})$ and vector of magnetization density $\mathbf{m}(\mathbf{r})$ are replaced by a 2×2 matrix whose spin density $\rho^{\alpha\beta}(\mathbf{r})$ is taken into account. α and β are the spin indices that can have two values, either (+) spin up or majority spin and (−) spin down or minority spin.

In the framework of the Hohenberg-Kohn-Sham spin density functional the Eq. (2.24) is given by [37, 38]

$$E[\rho^{\alpha\beta}(\mathbf{r})] = T_s[\rho^{\alpha\beta}(\mathbf{r})] + U_H[\rho^{\alpha\beta}(\mathbf{r})] + E_{xc}[\rho^{\alpha\beta}(\mathbf{r})] + v[\rho^{\alpha\beta}(\mathbf{r})], \quad (2.33)$$

with

$$\rho^{\alpha\beta}(\mathbf{r}) = \frac{1}{2} \left(\rho(\mathbf{r})\delta^{\alpha\beta} + m_x(\mathbf{r})\sigma_x^{\alpha\beta} + m_y(\mathbf{r})\sigma_y^{\alpha\beta} + m_z(\mathbf{r})\sigma_z^{\alpha\beta} \right) \quad (2.34)$$

and the electron density $\rho(\mathbf{r})$ as well as the vector of the magnetization density

$$\rho(\mathbf{r}) = \sum_{\alpha} \rho^{\alpha\alpha}(\mathbf{r}), \quad \mathbf{m}(\mathbf{r}) = \sum_{\alpha\beta} \boldsymbol{\sigma}^{\alpha\beta} \rho^{\alpha\beta}(\mathbf{r}). \quad (2.35)$$

Here, the upper greek symbols ($\alpha\beta$) describe the elements of the vector $\boldsymbol{\sigma} = (\sigma_x, \sigma_y, \sigma_z)$ of the 2×2 Pauli spin matrices

$$\sigma_x = \begin{pmatrix} 0 & 1 \\ 1 & 0 \end{pmatrix}, \quad \sigma_y = \begin{pmatrix} 0 & -i \\ i & 0 \end{pmatrix}, \quad \sigma_z = \begin{pmatrix} 1 & 0 \\ 0 & -1 \end{pmatrix}. \quad (2.36)$$

For validation of Eq. (2.33) by means of single-particle wave functions, one can compute the

energy minimum. Taking spin up (+) and spin down (−) orbitals into account that leads to the following Kohn-Sham equations

$$\left[-\frac{\hbar^2}{2m}\nabla^2(\mathbf{r}) + v_{KS}^\pm(\mathbf{r}) \right] \phi_i^\pm(\mathbf{r}) = \varepsilon_i^\pm \phi_i^\pm(\mathbf{r}). \quad (2.37)$$

The spin-density-functional theory, in principle, is exact. However, the XC functional E_{xc} and the XC potential v_{xc}^\pm contained in v_{KS}^\pm are not known and need to be approximated as within the spin-less DFT.

In a few cases, specially discussing the valence band structure, the spin-orbit interaction is taken into account. In principle, it requires the inclusion of non-collinear spins. However, in the used VASP code [39, 40] it only occurs in spheres around the nuclei. There, locally one can restrict the treatment to collinear spins. The axis of quantization of the spin is assumed to be the same at all points in space. Other so-called scalar relativistic effects, such as the mass and Darwin terms, are taken into account by their inclusion in the pseudopotentials describing their action for the atom case.

2.1.3 Exchange and correlation

As pointed out before, the main problem to calculate the electronic structure of matter is related to electrons interacting in a many-body system whose wave function is given by Eq. (2.2). For this system the Eq. (2.23) is, in principle, formally exact. However, by definition, in the Eq. (2.24) the term $E_{xc}[\rho(\mathbf{r})]$ contains all Coulomb exchange and correlation effects beyond the Hartree approximation and also part of correlation owing the difference among T of a interacting and T_{KS} of a non-interacting kinetic energies. Although Hohenberg-Kohn theorems guarantee that $E_{xc}(\mathbf{r})$ is a functional of $\rho(\mathbf{r})$, it is not explicitly known.

Decomposing $E_{xc}(\mathbf{r})$ in exchange E_x and E_c energies

$$E_{xc}[\rho(\mathbf{r})] = E_x[\rho(\mathbf{r})] + E_c[\rho(\mathbf{r})], \quad (2.38)$$

the Pauli principle is directly related with E_x . Then, using the results of a Kohn-Sham scheme, we can express E_x by the so-called exact exchange energy for spin-parallel electrons and occupied states [31]

$$E_x[\{\phi_i[\rho(\mathbf{r})]\}] = -\frac{e^2}{2} \sum_{jk} \int d^3r \int d^3r' \frac{\phi_j^*(\mathbf{r})\phi_k^*(\mathbf{r}')\phi_j(\mathbf{r}')\phi_k(\mathbf{r})}{|\mathbf{r}-\mathbf{r}'|}, \quad (2.39)$$

which is based on the Fock term for exchange. However Eq. 2.39 is no functional of $\rho(\mathbf{r})$, rather an orbital-dependent functional. The E_c case more complicated because there are no known expressions in terms of ϕ_i or $\rho(\mathbf{r})$.

In the following it is analyzed the most used approximation to the XC and the spin dependence is omitted. Many ideas and concepts in order to improve correlation beyond the

usual approaches are also mentioned.

2.1.3.1 Local density approximation (LDA)

Up to now, the idea was to looking for consistent XC approximations where both terms are treated in a consistent way. The simplest and successful approach is the so-called *Local Density Approximation* (LDA) proposed by Kohn-Sham [13] that considers a system of correlated electrons based on the homogeneous electron gas. A simplified model used in metallic systems that is widely used nowadays.

The XC energy functional Eq.(2.24) such that

$$E_{xc}[\rho(\mathbf{r})] = \int d^3r \rho(\mathbf{r}) \epsilon_{xc}(\mathbf{r}, [\rho(\mathbf{r})]) \quad (2.40)$$

is related to the XC energy $\epsilon_{xc} = \epsilon_x + \epsilon_c$ per electron with a exchange contribution given by $\epsilon_x = -\frac{3}{4} \left(\frac{3}{\pi}\right)^{1/3} \int d^3r \rho(\mathbf{r})^{4/3}$ [41]. Within the LDA $\epsilon_c(\mathbf{r}, [\rho(\mathbf{r})])$ is replaced by the corresponding quantity of the homogeneous electron gas $\epsilon_c^{hom}(\rho)$ with the local replacement $\rho = \rho(\mathbf{r})$.

Many approximations for ϵ_c have raised as a consequence of different treatment for the exact correlation energy [38, 42]. For a three-dimensional homogeneous electron gas Ceperley and Alder [43] have determined the functional dependence $\epsilon_c^{hom}(\rho)$ on ρ by means of quantum Monte Carlo calculations (QMC). Later this dependence has been parametrized by Perdew and Zunger [44]. Therefore, the functional

$$E_{xc}^{LDA}[\rho(\mathbf{r})] = \int d^3r \rho(\mathbf{r}) \epsilon_{xc}(\rho)|_{\rho=\rho(\mathbf{r})} \quad (2.41)$$

is available.

It easily allows a generalization to the case with spin polarization. The additional dependence on the fractional spin polarization is then usually determined by an interpolation, e. g. that suggested by von Barth and Hedin [45].

2.1.3.2 Generalized gradient approximation (GGA)

Several functionals have been developed in order to overcome the known failure of the LDA approximation [46–48]. Among them, the Generalized Gradient Approximation (GGA) has been considered to highlight due to improve LDA approximations taking partly into account the inhomogeneity of the electronic density $\rho(\mathbf{r})$, for instance, in molecules and surfaces. Although the term generalized implies in a general formulation for variations of $\rho(\mathbf{r})$, it provides a way of improvements of the desired properties or, at least agree with LDA when the inhomogeneity is very low.

The generalized form of Eq. (2.41) in GGA approximation takes the form,

$$\begin{aligned} E_{xc}^{GGA}[\rho(\mathbf{r})] &= \int d^3 r \rho(\mathbf{r}) \epsilon_{xc}(\rho(\mathbf{r}), \nabla \rho(\mathbf{r})) \\ &\equiv \int d^3 r \rho(\mathbf{r}) \epsilon_x^{hom}(\rho(\mathbf{r})) F(\rho(\mathbf{r}), \nabla \rho(\mathbf{r})), \end{aligned} \quad (2.42)$$

F is a dimensionless function and $\nabla \rho(\mathbf{r})$ the gradient of the electron density.

The several GGA approximations differ each other by the choose of the function F . Actually, the simplest and most widely used by physicists is the so-called Perdew-Burke-Ernzerhof form (PBE-GGA) [49]. This PBE functional accounts for the exchange part as

$$F_x(s) = 1 + k - \frac{k}{1 + \frac{\mu s^2}{k}} \quad (2.43)$$

with $s \sim \nabla \rho(\mathbf{r})$, so the term $s = 0$ guarantee that $F_x(0)=1$ the LDA is recovered or $F_x \rightarrow \text{constant}$ if s is too large. The quantity k is chosen in order to guarantee the Lieb-Oxford rule[50], and μ is chosen to cancel the term from correlation[31, 49].

In case of correlation, F_c , it is based on exact properties, and do not take into account empirical parameters. Also, it is expressed in terms of the local correlation in addition of terms that depends on the gradients as

$$E_c(\rho(\mathbf{r}), \nabla \rho(\mathbf{r})) = \int d^3 r \rho(\mathbf{r}) [\epsilon_c^{hom} + H(r_s, t)], \quad (2.44)$$

whith

$$t = \frac{|\nabla \rho(\mathbf{r})|}{2\rho k_s}, \quad k_s = \sqrt{\frac{4k_f}{\pi}}, \quad k_f = \left(\frac{9\pi}{4}\right)^{1/3} r_s, \quad r_s = \left(\frac{3}{4\pi\rho}\right)^{1/3} \quad (2.45)$$

and

$$H(r_s, t) = \gamma \log\left(1 + \frac{\beta}{\gamma} t^2 \left[\frac{1 + At^2}{1 + At^2 + A^2 t^4}\right]\right) \quad (2.46)$$

where

$$A = \frac{\beta}{\gamma} [\exp(\epsilon_c^{hom}/\gamma) - 1]^{-1}. \quad (2.47)$$

r_s is the local value of density parameter and t is scaled by the screening wave number k_s .

2.1.3.3 AM05 functional

With the aim of overcome several of the problems unsolved or introduced by LDA or GGA-PBE approaches, the field of research in new XC approximations for electronic structure of matter became huge. Then, several modified functionals were developed. The novel AM05 functional, despite to be a GGA-based functional, it is based on ideas to divide the system in subsystems. This functional improves some lack of LDA and GGA-PBE.

The idea to develop an improved and more comprehensive XC functional than LDA and

GGA started in 1998 with the work –*Edge Electron Gas* – of Kohn and Mattson [51]. In this work, they considered the variations of ρ in different regions of a physical systems, mainly that with electronic edge surface-like regions where the exponentially decay of the electron concentration accounts for a reduction of ρ [52]. So far, the homogeneous electron gas had been, the start point for LDA and all GGA-based functionals. However, in real physical systems this approach is somewhat unrealistic.

According Eq. (2.38) and Eq. (2.41) the treatment of XC can be separated into exchange (X) and correlation (C) parts and treated individually. In such way Kohn and Mattsson[51] concomitantly developed a suitable model for electronic surfaces so-called Airy gas that was expressed by means of electrons in a linear potential. Following that ideas Armiento and Mattsson, some years latter, formalized and generalized the AM05 XC functional [53] using the idea of subsystem functionals. Its involves two subsystem models: i) regions locally bulk-like for which the uniform electron gas based on the LDA scheme is used and ii) regions locally surface-like, for which the Airy gas combined with jellium surfaces provides a surface functional.

Using the, Local Airy Approximation (LAA), an XC functional was developed such that the equation,

$$\epsilon_x^{LAA}(\mathbf{r}; [\rho]) = \epsilon_x^{LDA}(\rho(\mathbf{r})) [X + (1 - X)F_x^{LAA}(s)], \quad (2.48)$$

is the exchange energy, and

$$\epsilon_c^{LAA}(\mathbf{r}; [\rho]) = \epsilon_c^{LDA}(\rho(\mathbf{r})) [X + (1 - X)\gamma], \quad (2.49)$$

is the correlation energy.

In Eq. (2.48) F_x^{LAA} is a refinement function

$$F_x^{LAA}(s) = (cs^2 + 1)/(cs^2/F_x^b + 1) \quad (2.50)$$

where c is a least-square fit to the true Airy gas exchange [53], s is the scaled density gradient computed as

$$s = |\nabla\rho(\mathbf{r})|/[2(3\pi^2)^{1/3}\rho^{4/3}(\mathbf{r})] \quad (2.51)$$

and F_x^b is an analytical interpolation constructed in order to satisfy two known limits of the Airy refinement function [53]. The parameter X from Eq. (2.48) and Eq.(2.49) is a density index as

$$X = 1 - \alpha s^2/(1 + \alpha s^2) \quad (2.52)$$

that depends on γ , a scaling factor, and α . Both quantities are obtained from the XC jellium surface energies.

A realistic approximation for E_{xc} should use an E_c that also fitted from the Airy gas system instead of the jellium surface. However, there is no available data in such way. So far, the

more compatible way adopted in [53] was to derive a semicompatible surface correlation from the XC data available for jellium surfaces model that have worked very well in that approximation.

In this work, we will show the efficiency of AM05 subsystem functional, at least for structural properties of the AlN, GaN and GaN, over the pure LDA and GGA-PBE functionals. The AM05 is found for geometries to be as accurate as the most advanced hybrid functionals. [54]

2.1.3.4 Hybrid functional (HSE)

The combination of orbital-dependent Hartree-Fock description and explicit density functionals raised a new class of XC functionals called *hybrid functionals*. By means of this combination, the approximated solution of the *many-body problem* via "pure" local or semi-local functionals is improved and more realistic owing spatial non-locality of XC is being taken into account. Usually, in these functionals, the hybrid screened Coulomb potential overcomes the exact exchange problem allowing the delocalization of the exchange hole [55].

Based on arguments of Becke [56, 57] for hybrid functionals, Perdew-Ernzerhof-Burke [58] proposed a new XC expression

$$E_{xc} = E_{xc}^{\beta} + \frac{1}{4} \left(E_x^{HF} - E_{xc}^{\beta} \right), \quad (2.53)$$

where $\beta =$ LDA or GGA (or a mix of them) XC energy and $\frac{1}{4}$ is the contribution of Hartree-Fock exchange that is taken into account.

A different form was presented by Ernzerhof and Scuseria [59], and Adamo and Barone [60], the so-called PBE0 hybrid functional. This functional was based on the GGA-PBE XC parametrized by Perdew et. al [49] such that,

$$E_{xc}^{PBE0} = aE_x^{HF} + (1 - a)E_x^{PBE} + E_c^{PBE} \quad (2.54)$$

whose parameter a is $\frac{1}{4}$ estimated by perturbation theory [56, 57].

Heyd et. al [55] applying arguments of long range (LR) and short range (SR) on the screening Coulomb potential proposed the HSE03 hybrid functional expressed as

$$E_{xc}^{HSE03} = aE_x^{HF,SR}(\omega) + (1 - a)E_x^{\omega PBE,SR}(\omega) + E_x^{\omega PBE,LR}(\omega) + E_c^{PBE}, \quad (2.55)$$

whose range-separation parameter ω accounts for the LR and SR terms taken the error function [55] into account. If $\omega = 0$ it provides the full Coulomb operator, otherwise if $\omega \rightarrow \infty$, the GGA-PBE is achieved. For semiconductors the reliable band gap value is accounted using $\omega \leq 0.15 \text{ \AA}^{-1}$ that provides accuracy and satisfactory time computer consuming. [61]

In practice, the Coulomb potential $v(\mathbf{r})$ is replaced by $v(\mathbf{r})\text{erfc}(\mu|v|)$ with $\mu = 0.3 \text{ \AA}^{-1}$ or slight modifications [see discrimination in HSE06 by J. Paier et al. in [62] and [63]].

In the present work the hybrid functionals HSE03/HSE06 is used but not to perform ground state calculations. Rather, the eigenvalues and eigenfunctions of the Kohn-Sham equation Eq. (2.31) with a non-local potential, the Kohn-Sham equation of the so-called generalized DFT [61, 64] are used as starting electronic structure to describe electronic single-particle and neutral pair excitations. Due to the spatial non-locality of the XC potential one important feature of the XC self-energy is already taken into account.

2.1.3.5 LDA+ U method

Calculating optical properties the required density of mesh points for the sampling of the Brillouin zone is too high, so that, the necessary quasiparticle computations starting with a non-local potential derived from an hybrid functional are forbidden owing of the computational effort. In order to describe, at least, partially the limitations in XC due the LDA and possible self-interaction corrections for the Ga-3*d* and In-4*d* electrons, inspired by the Hubbard model [65], a different approach has been developed, which is to add a Hubbard like on-site repulsion on top of the usual Kohn-Sham Hamiltonian using an effective U parameter. This gives rise to an orbital-dependent modification of the DFT total energy

$$E^{LDA+U} = E^{LDA} + \frac{U}{2} \sum_m \left[\sum_i n_{ii}^m - \sum_{i,j} n_{ij}^m n_{ji}^m \right] \quad (2.56)$$

with n_{ij}^m as the elements of the density matrix of the corresponding d -shell for a given spin orientation m . In practice we use a scheme proposed by Dudarev et al. [66]. All d -states derived from Kohn-Sham levels are shifted by an energy $-U(n_{ij}^m - \frac{1}{2}\delta_{ij})$.

2.2 Excited electronic state properties

In spite of DFT to be an exact theory for ground state properties, there are failures in the description of the excited states properties. It means that the energy differences between occupied and empty states in the quasiparticle bandstructures and optical properties are significantly underestimated in the framework of the DFT (see Aulbur et al. [26]). For instance, the eigenvalues computed into the Kohn-Sham formalism [13] and also, excitations energies are determined by the static charge density. However, It is known that excitation processes can lead to perturbations of the system introducing changes in the electron density.

The electronic system reacts to the excitations with a redistribution of electrons whose consequences can be described by screening of the Coulomb interaction. These effects [67] can be treated within the framework of many-body perturbation theory [26, 68–70]. This leads to an accurate numerical modeling of theoretical quasiparticle bandstructures contained in several spectroscopies and optical properties.[67] It is usually based on the so-called GW approximation, in that G denotes the Green's function of the system and W accounts to the screened Coulomb interaction derived from the bare Coulomb interaction and

represents the response of the system owing an excitation.

2.2.1 Green's function

The many-body properties of the excited state of a system such a semiconductors constituted of strongly interacting particles can be approximated by means of properties of weakly interacting "particles" so-called quasiparticles. The figurative term quasiparticle describes the bare electron and the positive screening charge that surrounds its owing the presence of an other electron. The quasiparticle lifetime is finite due the approximated eigenstate character of the N -electron Hamiltonian in Eq. (2.2). Several properties of the quasiparticles that are defined by expectation values, for instance, their density and even the total energy of a many-body system can be evaluated by means of the single-particle Green function [26, 71]. However, in spite of G to be known exactly [72] and to give much more information than the electronic density, its application to ground state properties is somewhat rare.

The main variable is the time-ordered Green function $G(\mathbf{r}t, \mathbf{r}'t')$ whose poles yield excitation energies and also the excitation lifetimes. The single-particle Green function [26] is defined as

$$\begin{aligned} G(\mathbf{r}t, \mathbf{r}'t') &= -i\langle\Psi_0|\hat{T}[\hat{\psi}(\mathbf{r}t)\hat{\psi}^\dagger(\mathbf{r}'t')]| \Psi_0\rangle \\ &= \begin{cases} -i\langle\Psi_0|\hat{\psi}(\mathbf{r}t)\hat{\psi}^\dagger(\mathbf{r}'t')| \Psi_0\rangle, & t > t', \\ i\langle\Psi_0|\hat{\psi}(\mathbf{r}t)\hat{\psi}^\dagger(\mathbf{r}'t')| \Psi_0\rangle, & t' > t, \end{cases} \end{aligned} \quad (2.57)$$

with $|\Psi_0\rangle$ the ground state of the N -electron Hamiltonian (cf. Eq. (2.2)), T is the Wick time-ordering operator,

$$\hat{\psi}(\mathbf{r}t) = \exp(i\hat{H}t)\hat{\psi}(\mathbf{r})\exp(-i\hat{H}t) \quad (2.58)$$

is the Fermion annihilation operator and $\hat{\psi}^\dagger(\mathbf{r}t)$ the corresponding creation operator. According to Eq. (2.57) the propagation of particles (antiparticles) or still the dynamics of excitations in N -electrons system is given by G taking for $t > t'$ ($t < t'$). It means the probability to find the particle at time t and position \mathbf{r} after its creation at time t' and position \mathbf{r}' (or vice-versa).

Interestingly, the Fourier-transformed G is related to experimental photoemission spectra [26] via its imaginary part,

$$A(\mathbf{r}, \mathbf{r}'; E) = \pi^{-1}|\text{Im}G(\mathbf{r}, \mathbf{r}'; E)|. \quad (2.59)$$

Eq. (2.59) defines the so-called *spectral function* A , i. e., the density of the excited (or quasiparticle) states that contribute to the electron or hole propagation. Especially quasiparticles can be identified in the spectral function due their narrow peak that by means of position and width can account to the energy and inverse lifetime of the quasiparticles. Experimentally those properties of quasiparticles are measured by direct or inverse photoemission spec-

troscopy by adding to or taking out an electron of the system.[26]

2.2.2 Self-energy

The treatment of electronic single-particle excitations is based on the knowledge of the single-particle Green function G .

Using the Heisenberg equation of the motion for an electron (annihilation) field operator $\psi(x) = \psi(r, t)$ we have

$$i \frac{\partial \hat{\psi}(x)}{\partial t} = [\hat{\psi}(x), \hat{H}] \quad (2.60)$$

with \hat{H} as the many-electron Hamiltonian Eq. 2.2 rewritten in second quantization [73]

$$\hat{H} = \int d^3 r \hat{\psi}^\dagger(\mathbf{r}) h_0(x) \hat{\psi}(\mathbf{r}) + \frac{1}{2} \int d^3 r d^3 r' \hat{\psi}^\dagger(\mathbf{r}) \hat{\psi}^\dagger(\mathbf{r}') v(\mathbf{r} - \mathbf{r}') \hat{\psi}(\mathbf{r}') \hat{\psi}(\mathbf{r}), \quad (2.61)$$

where h_0 is the kinetic operator of an individual electron plus a local external potential $v(\mathbf{r})$. Then, we obtain the equation of the motion for the Green function Eq. (2.57) such as

$$\left[i \frac{\partial}{\partial t} - h_0(x) \right] G(x, x') - \int dx'' M(x, x'') G(x'', x) = \delta(x - x'). \quad (2.62)$$

Here M is an operator so-called mass operator that contains the Hartree potential Eq. (2.27) and the XC self-energy. It is defined as

$$\int dx_1 M(x, x_1) G(x_1, x') = -i \int d^3 r_1 v(\mathbf{r} - \mathbf{r}_1) \times \langle \Psi_0 | T[\hat{\psi}^\dagger(\mathbf{r}_1, t) \hat{\psi}(\mathbf{r}_1, t) \hat{\psi}(\mathbf{r}, t) [\hat{\psi}^\dagger(\mathbf{r}', t')]] | \Psi_0 \rangle \quad (2.63)$$

The right side, it is accounted for a special case of the Green function for two-particles [74]

$$G_2(1, 2, 3, 4) = (i)^2 \langle \Psi_0 | T[\hat{\psi}(1) \hat{\psi}(3) \hat{\psi}^\dagger(4) \hat{\psi}^\dagger(2)] | \Psi_0 \rangle \quad (2.64)$$

where $1 \equiv x_1 = (\mathbf{r}_1, t_1)$, etc.

From Eq. (2.64), the $v_H(\mathbf{r})$ Eq. (2.27) is obtained and the Σ can be defined as

$$\Sigma = M - v_H(\mathbf{r}) \delta(\mathbf{r} - \mathbf{r}'). \quad (2.65)$$

The equation of motion (cf. Eq. 2.62) is replaced by

$$\left[i \frac{\partial}{\partial t} - H_0(x) \right] G(x, x') - \int dx'' \Sigma(x, x'') G(x'', x) = \delta(x, x') \quad (2.66)$$

with

$$H_0 = h_0 + v_H(\mathbf{r}). \quad (2.67)$$

From Eq.(2.66) it follows formally

$$G^{-1} = i \frac{\partial}{\partial t} - H_0 - \Sigma. \quad (2.68)$$

Using the functional derivative method [75, 76] we introduce a varying field $\phi(\mathbf{r}, t)$ used as mathematical tool in order to evaluate the Σ and it will be set to zero once the Σ is obtained. [74] It follow, in Dirac notation, that

$$|\psi_D(\mathbf{r}, t)\rangle = \hat{U}(t, t_0)|\psi_D(\mathbf{r}, t_0)\rangle \quad (2.69)$$

the \hat{U} operator counts for the time development by

$$\hat{U}(t, t_0) = T \exp[-i \int_{t_0}^t d\tau \hat{\phi}(\tau)] \quad (2.70)$$

and

$$\hat{\phi}(\tau) = \int d^3 r \phi(\mathbf{r}, \tau) \hat{\psi}_D^\dagger(\mathbf{r}, \tau) \hat{\psi}_D(\mathbf{r}, \tau). \quad (2.71)$$

According Heisenberg and Dirac representation,

$$\hat{\psi}(\mathbf{r}, t) = \hat{U}^\dagger(t, 0) \hat{\psi}_D(\mathbf{r}, t) \hat{U}^\dagger(t, 0). \quad (2.72)$$

The field operator $\hat{\psi}$ satisfies

$$i \frac{\partial}{\partial t} \hat{\psi}_D = [\hat{\psi}_D, \hat{H}(\phi = 0)]. \quad (2.73)$$

The Eq. (2.73) agrees with Heisenberg operator for unperturbed conditions where $\phi = 0$. Then, the Green function can be written in such way

$$iG(1, 2) = \frac{\langle \Psi_0 | T[\hat{U}(\infty, -\infty) \hat{\psi}_D(1) \hat{\psi}_D^\dagger(2)] | \Psi_0 \rangle}{\langle \Psi_0 | \hat{U}(\infty, -\infty) | \Psi_0 \rangle}. \quad (2.74)$$

Applying the functional derivative of G related to ϕ we obtain

$$\frac{\delta G(1, 2)}{\delta \phi(3)} = G(1, 2)G(3, 3^+) - G_2(1, 2, 3, 3^+) \Big|_{\phi=0}. \quad (2.75)$$

Using the identity

$$\frac{\partial}{\partial \phi} (G^{-1}G) = G^{-1} \frac{\partial G}{\partial \phi} + \frac{\partial G^{-1}}{\partial \phi} G = 0 \quad \rightarrow \quad \frac{G}{\phi} = -G \frac{\delta G^{-1}}{\delta \phi} G \quad (2.76)$$

By means of $\frac{\delta G^{-1}}{\delta \phi}$, one a the set of integro-differential equations, the so-called Hedin's equations.

In principle the exact self-energy can be determined iteratively combining the five integro-differential equations: (here: using the short-hand notation $1 := (\mathbf{r}_1, t_1)$, $1^+ = (\mathbf{r}_1, t_1 + \delta)$, $\delta > 0$

infinitesimal, $v(1,2)$ the bare coulomb interaction)

$$\Sigma(1,2) = i \int d(3,4) G(1,4) W(1^+,3) \Gamma(4,2;3), \quad (2.77)$$

$$W(1,2) = v(1,2) + \int d(3,4) W(1,3) P(3,4) v(4,2), \quad (2.78)$$

$$P(1,2) = -i \int d(3,4) G(2,3) G(4,2) \Gamma(3,4;1), \quad (2.79)$$

$$\Gamma(1,2;3) = \delta(1,2)(1,3) + \int d(4,5,6,7) \frac{\delta \Sigma(1,2)}{\delta G(4,5)} G(4,6) G(7,5) \Gamma(6,7;3), \quad (2.80)$$

where both quantities P and Γ satisfy Bethe-Salpeter equation with P the irreducible polarizability and Γ the vertex function. The fifth equation is the equation of motion Eq. 2.66.

The Dyson Eq. 2.66 or Eq. 2.68 can be rewritten starting from the Green function G .

$$G_0^{-1} = i \frac{\partial}{\partial t} - H_0 - v_{xc}, \quad (2.81)$$

which partly combines XC effects in a XC potential v_{xc} . It follows

$$G^{-1} = G_0^{-1} - \Sigma + v_{xc} \quad (2.82)$$

where Σ accounts for all XC effects beyond the Hartree approximation.[26] The poles of G yield the excitation energies. G_0 is also a Green's function beyond the Hartree approximation, where XC is already included via an approximate potential v_{xc} .

Neglecting the XC self-energy in a first step of interaction Eq. (2.80) is reduced to the first term, such as $\Gamma(1,2;3) = \delta(1,2)(1,3)$. It results Hedin's GW approximation for the XC self-energy

$$\Sigma(1,3) = G(1,2) W(1^+,2), \quad (2.83)$$

which may be interpreted as a linear expansion of the XC self-energies in terms of the dynamically screened Coulomb potential W . [71]

In these work, we are mainly interested in energetical quasiparticle properties, especially in QP band structures. Therefore, we neglect satellite structures in the spectral function Eq. (2.59) and replace it approximately by one δ -function at the corresponding QP energy. Instead of solving the full Dyson equation Eq. (2.81) we only solve the so-called QP equation [26]

$$[h_0(\mathbf{r}) + v_H(\mathbf{r})] \phi_i^{QP}(\mathbf{r}) + \int d\mathbf{r}' \sigma(\mathbf{r}\mathbf{r}', \varepsilon_i^{QP}) \phi_i^{QP}(\mathbf{r}') = \varepsilon_i^{QP} \phi_i(\mathbf{r}) \quad (2.84)$$

with the XC self-energy usually taken within the GW approximation Eq. 2.83. Its solution depends on the quasiparticle self-energy (Σ) that is a non-local, non-Hermitian and energy-dependent operator [26]. We solve this equation iteratively. In a first step we replace Σ by v_{xc} from the HSE06 hybrid functional [for details see Ref. [64]] to determine the starting electronic structure and compute the changes of the QP eigenvalues by first order perturbation

theory.

2.2.3 Bethe-Salpeter equation (BSE)

The electron-hole interaction or excitonic effects are essential to improve the description of the spectral behavior of response functions, especially if they are related to neutral electronic excitations. This especially holds for optical spectra and hence the frequency-dependent dielectric function. Including excitonic effect by means of the BSE, the evaluation of the macroscopic DF in order to compute measurable quantities, e. g., absorption and energy-loss spectra are much closer to the experimental ones. The BSE can also describe the bound-states of two-particle electron-hole excitations.

Using the definition of the polarization P Eq. (2.79) the BSE for the vertex function Γ Eq. (2.80) can be rewritten to a BSE for P . Commonly, its kernel is further approximated within the GW approximation Eq. (2.83). One nearly sets $\delta\Sigma/\delta G \sim -W$. Terms related to the functional derivative of W are neglected. In addition, also the dynamics of the screening in W is omitted [70].

However, the resulting polarization function P only yields the microscopic dielectric function, $\varepsilon = 1 - \nu P$. Instead the macroscopic dielectric function $\varepsilon_M(\omega)$ also accounts for optical local field effects (LFEs). For translational invariant systems with reciprocal lattice vectors \mathbf{G}, \mathbf{G}' it can be written in the optical limit $\mathbf{q} \rightarrow 0$ in the form [77, 78]

$$\varepsilon_M(\hat{\mathbf{q}}, \omega) = \hat{\mathbf{q}} \varepsilon_M(\omega) \hat{\mathbf{q}} = \lim_{\mathbf{q} \rightarrow 0} \frac{1}{\varepsilon^{-1}(\mathbf{q} + \mathbf{G}, \mathbf{q} + \mathbf{G}'; \omega)} \Big|_{\mathbf{G}=\mathbf{G}'=0} \quad (2.85)$$

with $\hat{\mathbf{q}} = \frac{\mathbf{q}}{|\mathbf{q}|}$, where ε is the macroscopic dielectric function. The effect of the LFEs can be also described by a modified kernel of the BSE (for a modified P , the polarization function of the macroscopic dielectric function) which contains besides the attractive screened interaction $-W$ of the excited electrons and holes also an unscreened Coulomb repulsion \bar{v} whose short range part has been omitted with respect to ν [79, 80].

The inhomogeneous BSE derived from Eq. (2.80) is numerically difficult to handle. For that reason the appearing space and energy dependences are usually expressed by the appropriate solutions $\varepsilon_i^{QP}, \phi_i^{QP}$ or ε_i, ϕ_i of the QP equation (2.84), even using only a zero'th order approximation for the XC self-energy. In this work only translational invariant systems, e. g. zinc-blende and wurtzite crystals as well as systems whose unit cell consists of several wurtzite cells. The single-particle eigenstates can be described by Bloch functions $|\nu\mathbf{k}\rangle$ and Bloch energies $\varepsilon_\nu(\mathbf{k})$ with band index ν (conduction band index $\nu = c$, valence band index $\nu = v$) and Bloch wave vector \mathbf{k} of the corresponding Brillouin zone.

2.2.4 Excitonic Hamiltonian

In the Bloch representation the inhomogeneous BSE for the modified P function, in practice can be solved by the diagonalization of the two-particle Hamiltonian (excitonic Hamiltonian) $\hat{H}(c\nu\mathbf{k}, c'\nu'\mathbf{k}')$. The corresponding Schrödinger-like equation is

$$\hat{H}(c\nu\mathbf{k}, c'\nu'\mathbf{k}')A_\Lambda(c'\nu'\mathbf{k}') = E_\Lambda A_\Lambda(c\nu\mathbf{k}), \quad (2.86)$$

which provides excitonic eigenvalues (E_Λ) and eigenstates (A_Λ). It can be also interpreted as a homogeneous BSE.

In Eq. 2.86 the excitonic Hamiltonian can be expressed for single pairs as [81, 248]

$$\hat{H}_{c\nu\mathbf{k}, c'\nu'\mathbf{k}'} = (\varepsilon_{c\mathbf{k}}^{QP} - \varepsilon_{\nu\mathbf{k}}^{QP})\delta_{cc'}\delta_{\nu\nu'}\delta_{\mathbf{k}\mathbf{k}'} - W_{c\nu\mathbf{k}}^{c'\nu'\mathbf{k}'} + 2\bar{v}_{c\nu\mathbf{k}}^{c'\nu'\mathbf{k}'}. \quad (2.87)$$

The first term on the right side of Eq. (2.87) describes the non-interacting quasielectron-quasihole pairs, the second term represents the screened Coulomb attraction of pairs $c\nu\mathbf{k}$ and $c'\nu'\mathbf{k}'$ as

$$W_{c\nu\mathbf{k}}^{c'\nu'\mathbf{k}'} = \frac{4\pi}{\Omega} \sum_{\mathbf{G}\mathbf{G}'} \frac{\varepsilon_{\mathbf{G}\mathbf{G}'}^{-1}(q)}{|\mathbf{G}|^2} \langle c\mathbf{k} | e^{i(q+\mathbf{G})\cdot\mathbf{r}} | c'\mathbf{k}' \rangle \langle \nu'\mathbf{k}' | e^{-i(q+\mathbf{G}')\cdot\mathbf{r}} | \nu\mathbf{k} \rangle, \quad (2.88)$$

while the third contribution describes their electron-hole exchange interaction and, hence, the LFEs as

$$\bar{v}_{c\nu\mathbf{k}}^{c'\nu'\mathbf{k}'} = \frac{4\pi}{\Omega} \sum_{\mathbf{G} \neq 0} \frac{1}{|\mathbf{G}|^2} \langle c\mathbf{k} | e^{i\mathbf{G}\cdot\mathbf{r}} | \nu\mathbf{k} \rangle \langle \nu'\mathbf{k}' | e^{-i\mathbf{G}\cdot\mathbf{r}} | c'\mathbf{k}' \rangle, \quad (2.89)$$

The direct diagonalization of the excitonic Hamiltonian is expensive in both memory and computer time owing the high number of electron-hole states given by $N = N\nu \times Nc \times NKP$, with numbers $N\nu$ of all VBs, Nc all CBs, and NKP all \mathbf{k} points. Eq. (2.87) can be solved numerically by several different methods. One is the iterative-diagonalization scheme where optical properties from lowest optical transitions can be evaluate [64].

In this work we use the time-development method [83], where instead of Eq. (2.86) the corresponding time-dependent Schrödinger equation is solved. The Fourier transformation directly gives the optical spectra, more precisely the frequency-dependent dielectric function. The advantage of the method is related to the reduced computational cost since the method only scales quadratically with the rank of the matrix (2.87), since only matrix-vector operations occur. The disadvantage of the method is that the pair eigenvalues E_Λ and pair eigenstates $A_\Lambda(c\nu\mathbf{k})$ are not anymore directly be computed.

2.2.5 Dielectric function

In order to describe linear optical properties the frequency-dependent macroscopic dielectric function (DF), $\varepsilon_{\perp, \parallel}(\omega)$, has to be computed.

Using the relation of P to $\varepsilon_M(\hat{\mathbf{q}}, \omega)$ and the described Bloch representation, the components of the dielectric tensor $\hat{\varepsilon}(\omega)$ can be directly determined in the limit of vanishing photon wave vectors. Here, we usually study uniaxial hexagonal systems with two independent tensor components for ordinary/extraordinary light polarization $\mathbf{e}_{\perp/\parallel}$ perpendicular/parallel to the c -axis.

The eigenvalues E_Λ and eigenvectors $A_\Lambda(c\nu\mathbf{k})$ of the pair Hamiltonian in Eq. (2.87) lead to the macroscopic DF [81]

$$\varepsilon_{\perp,\parallel}(\omega) = 1 + \frac{8\pi e^2 \hbar^2}{Vm^2} \sum_{\Lambda} \left| \sum_{c,\nu,\mathbf{k}} \frac{\langle c\mathbf{k} | \mathbf{e}_{\perp,\parallel} \cdot \hat{\mathbf{p}} | \nu\mathbf{k} \rangle}{\varepsilon_{c\mathbf{k}} - \varepsilon_{\nu\mathbf{k}}} A_{\Lambda}^*(c\nu\mathbf{k}) \right|^2 \times \sum_{k=+,-} \frac{1}{E_{\Lambda} - k\hbar(\omega + i\gamma)} \quad (2.90)$$

with the momentum operator $\hat{\mathbf{p}}$. V denotes the crystal volume, whereas γ describes the inverse electron-hole pair lifetime chosen to be $\gamma = 0.1$ eV.

2.3 Alloy description

This theoretical approach is devoted to the underlying properties of pseudoternary alloys and their constituent compounds. It is based on the cluster expansion method [84, 85] that provides the necessary background for a comprehensive and detailed study of alloys using statistical models. Here the cluster statistics is described within the so-called generalized quasi-chemical approximation model (GQCA) [86] and their limiting cases the strict-regular solution model (SRS) and the microscopic decomposition model (MDM).

2.3.1 Cluster expansion

The cluster expansion method [87, 88] is one of the central descriptions of chemically disordered solids such as isostructural $A_xB_{1-x}C$ alloys. An alloy $A_xB_{1-x}C$ consists of N atoms on the C anion sublattice and a total of N cations of type A or B on the other sublattice. For the cluster expansion the macroscopic alloy is divided into M clusters, each of which consists of $2n$ atoms (n anions and n cations) [85, 89, 90] (see Fig. 2.1). Consequently, the total number of cations and anions is $N = nM$. Due to the symmetry of the crystal lattice, all possible clusters can be grouped into $J + 1$ different classes. Each class j ($j = 0, \dots, J$) comprises g_j clusters of the same total energy ε_j . The number of cations of species A in each class is denoted by n_j . The macroscopic alloy is built of a set of $\{M_0, M_1, \dots, M_j\}$ clusters. Hence, a single class j contributes with its cluster fraction $x_j = M_j/M$. Since the x_j describe the statistical weights of all clusters, it holds $\sum_{j=0}^J x_j = 1$. For the wz polymorph of the nitrides studied in this work 16-atom supercells ($n = 8$) are constructed from four wurtzite cells (see Fig. 2.2) and used to simulate the clusters. Thus, 256 clusters occur in total for each ternary nitride

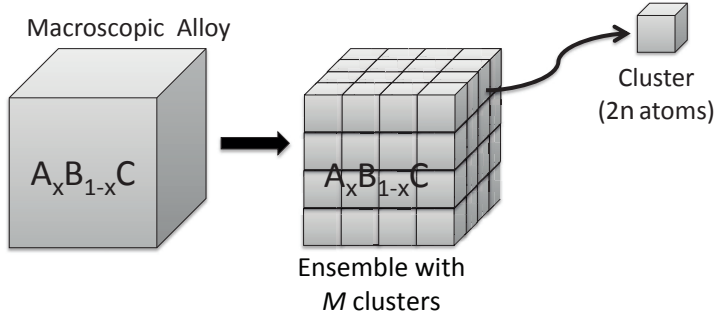


Figure 2.1: Illustration of the cluster expansion. The macroscopic alloy is divided into an ensemble with M clusters, each of which consists of $2n$ atoms (n anions (C) and n cations (A),(B) or (A+B)).

and are grouped in $J + 1 = 22$ classes due to their point-group symmetries. More specifically, the atomic geometries described in Appendix A.1 are employed in this work. The 16-atom cell (see Fig. 2.2) can be chosen in such a way that in the case of $\text{In}_x\text{Ga}_{1-x}\text{N}$ and $\text{In}_x\text{Al}_{1-x}\text{N}$ mostly N atoms occupy the surface sites of the cell (see Fig. 2.2). Since the N sublattice (although somewhat deformed after atomic relaxation) is present in all cluster materials, the clusters with such a surface may roughly be considered to be statistically independent.

Within this framework any property P of the macroscopic alloy is connected to the respective properties P_j of the individual clusters via the Connolly-Williams formula [89, 91]

$$P(x, T) = \sum_{j=0}^J x_j(x, T) P_j, \quad (2.91)$$

and fluctuations around the configurational averages can be described via the mean-square deviations

$$\Delta P(x, T) = \sqrt{\sum_{j=0}^J x_j(x, T) P_j^2 - P^2(x, T)}. \quad (2.92)$$

Such a property P_j for a certain cluster class could be, e. g. one component of the dielectric tensor. Since the weights $x_j(x, T)$ depend on the average composition x of the alloy as well as under certain circumstances on the temperature T , it is possible to account for the influence of different preparation conditions [84]. Here three cluster statistics are distinguished: i) Generalized Quasichemical Approximation and their limiting cases ii) Strict-regular solution model, and iii) Microscopic decomposition model.

2.3.2 Generalized Quasichemical Approximation

In this approach, the thermodynamic equilibrium is described by cluster fractions that lead to a minimum of the Helmholtz free energy $F(x, T)$. In this case, the so-called generalized quasi-chemical approximation [85, 89], the weights x_j^{GQCA} can be derived from the

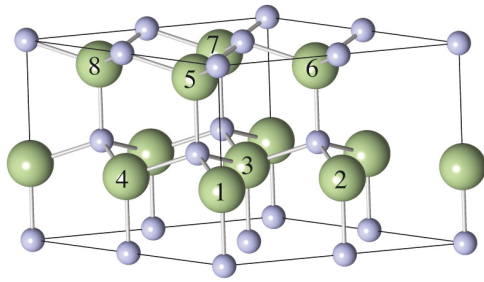


Figure 2.2: Illustration of atomic sites in the 16-atom clusters consisting of four wz cells. Anions (N atoms) are depicted as blue (small) balls, cations (In, Ga, or Al atoms, respectively) as green (large) balls with labels. The cell boundaries are indicated by thin solid lines.

free-energy contribution of the solution/at the mixture

$$\Delta F(x, T) = \Delta U(x, T) - T\Delta S(x, T), \quad (2.93)$$

where $\Delta S(x, T)$ is the mixing entropy and $\Delta U(x, T)$ is the contribution of the mixing internal energy obtained from the ensemble with M clusters as

$$\begin{aligned} \Delta U(x, T) &= \sum_{j=0}^J M_j \varepsilon_j - M[(1-x)\varepsilon_0 + x\varepsilon_J] \\ &= M(\sum \Delta \varepsilon_j x_j), \end{aligned} \quad (2.94)$$

whose term $\Delta \varepsilon_j$ accounts for the excess energy for each class j as

$$\Delta \varepsilon_j = \varepsilon_j - \left(\frac{n_j}{n} \varepsilon_J + \frac{n - n_j}{n} \varepsilon_0 \right). \quad (2.95)$$

According Eq. (2.93) it is also necessary an expression to the ΔS in order to compute of the free-energy of the alloy system. Then, the mixing entropy can be calculated using the Boltzmann definition

$$\Delta S = k_B \ln W \quad (2.96)$$

with W the number of possible configurations of cation arrangements.

In a cluster expansion the set of clusters whose $\sum_{j=0}^J x_j = 1$ constraint is fulfilled, have a W that counts for all possible ways of arranging all A and B atoms in one given set on the, $N = N_A + N_B$ cation sites. To determine W , the number of ways of arranging the M_0, M_1, \dots, M_J clusters to form the alloy, the number of probability $M! / \prod_{j=0}^J M_j!$, needs to be multiplied by the number of possibilities of arranging the cations in each cluster. Since one cluster of class j can be occupied by cations in g_j ways, all M_j clusters lead to $g_j^{M_j}$ possibilities. Ones have

$$W = \frac{M!}{\prod_{j'=0}^J M_{j'}!} \prod_{j'=0}^J g_{j'}^{M_{j'}}. \quad (2.97)$$

Combining Eq. (2.96) with Eq. (2.97) and taking the Stirling limit, it follows for the mixing entropy

$$\Delta S(x, T) = -k_B \left\{ N \left[x \ln x + 1(1-x) \ln(1-x) \right] + M \sum_{j=0}^J x_j \ln \left(\frac{x_j}{x_0} \right) \right\}. \quad (2.98)$$

Thus, In the GQCA the x_j are determined by the requirement that $\Delta F(x, T)$ takes a minimum with respect to the cluster distribution, i.e., $\partial \Delta F(x, T) / \partial x_j = 0$. Hence, the Lagrange formalism with the constraint $\sum_{j=0}^J x_j = 1$ yields

$$x_j^{\text{GQCA}}(x, T) = \frac{g_j \eta^{n_j} e^{\beta \Delta \varepsilon_j}}{\sum_{j'=0}^J g_{j'} \eta^{n_{j'}} e^{-\beta \Delta \varepsilon_{j'}}}, \quad (2.99)$$

where $\beta = 1/k_B T$, $\Delta \varepsilon_j$ is the excess energy of cluster j , and η is determined by minimizing $\Delta F(x, T)$ with respect to x under the constraint $\sum_{j=0}^J n_j x_j = nx$ [84, 89]. The excess energies are defined by relation of the cluster energy ε_j with respect to the end components ε_j ($j = 0$ and $j = J$) with $n = 8$ and $J = 21$ as described in Eq. 2.95.

2.3.3 Limiting cases

Besides the thermodynamic equilibrium described above, the experimental situation also suggests the studying of certain non-equilibrium preparation conditions, for which the actual cluster statistics may be modified by kinetic barriers, frozen high-temperature states, as well as interface or surface influences. In order to simulate a dependence of the cluster distribution on the preparation conditions we study two limiting cases of Eq. 2.99 [92].

2.3.3.1 Strict-regular solution model

Within the strict-regular solution model [85] the ideal fractions,

$$x_j^0 = g_j x^{n_j} (1-x)^{n-n_j}, \quad (2.100)$$

are employed, which arise from a purely stochastic distribution of the clusters. They are independent of the temperature and the clusters' excess energies. This case can be interpreted as the high-temperature limit of the GQCA. The degeneracy factor in each cluster class is given by $g_j = \binom{n}{n_j}$ leading to a total number $\sum_{j=0}^J g_j = 2^n$.

2.3.3.2 Microscopic decomposition model

The microscopic decomposition model assumes that the cations of type In (Ga, Al) are more likely to occur close to cations of the same type In (Ga, Al). This is realized by cluster fractions that interpolate linearly between the binary end components, i.e.,

$$x_j^{\text{MDM}} = \begin{cases} 1-x & \text{for } j=0 \\ x & \text{for } j=J \\ 0 & \text{otherwise} \end{cases} . \quad (2.101)$$

Within the MDM mixing does not lead locally to a gain of internal energy, which can be the case under certain preparation conditions. The MDM represents the low-temperature limit

of the GQCA.

2.4 Numerical approaches

In this work, a systematic study of the group-III nitrides and their alloys are performed using DFT-based methods as implemented in the Vienna *Ab initio* Simulation Package (VASP)[39, 40], more specifically the version 5.1.39. The solution of the Kohn-Sham (KS) equation of DFT (cf. sec. 2.1.2.2) provides the ground-state electron density of the interacting electrons as well as eigenvalues and eigenstates of non-interacting KS particles. However, experimental techniques such as photoelectron emission, inverse photoelectron spectroscopy, or tunnel spectroscopy, that measure band structures or densities of states (DOS), involve electronic excitations and rather probe single-QP energies. Also in transport experiments, QP phenomena of charged carriers (electrons or holes) and, therefore, electronic excitation effects, may play a role, e.g. via the carrier masses.

DFT, however, suffers from the so-called band-gap problem: The KS gaps calculated for semiconductors and insulators significantly underestimate the QP gaps derived from measurements.[26] The band-gap problem is here solved within the framework of the many-body perturbation theory,[70] which yields a QP equation[26] that properly includes the XC self-energy of the electrons and, hence, accounts for the excitation aspect. The non-Hermitian, non-local, and energy-dependent self-energy is usually described by means of Hedin's *GW* approximation[68, 69], (cf. sec. 2.2.2). The computation of properties of the excited states within the MBPT is possible combining this technique with DFT and PAW methods in the VASP code. In a last step the single-particle results are used to describe electron-hole pair excitations.

2.4.1 PAW method

In molecules and solids there are different atomic species, each one constituting of both ion cores and valence electrons. Owing the very deep Coulomb potential of the nuclei the wavefunctions of the core electrons are very localized around the nuclei occupying a very small volume. However, their KS eigenvalues ε_i Eq. (2.31) are large and negative. Concomitantly, on the other hand, the valence electrons experience a much weaker Coulomb potentials due the nuclei because they are screened by the core electrons. Consequently, the valence electrons possess more spread wavefunctions. Thus, in ensemble of bonded atoms one may approximate the change of the single-particle potentials in almost constant. It means that one may also consider that the changes in one-electron energies of the core electrons are almost vanishing. Hence, the core wavefunctions for a given atomic specie in a molecule or solid are approximately the same as for the isolated atomic species. Then, in the so-called *frozen-core approximation* the wavefunctions of the core electrons are assumed to

be identical to that of the isolated atoms, while the wavefunctions of the valence electrons are considered variationally. [93]

However, the *frozen-core approximation* leads to complications concerning to the orthogonality of the valence electrons related to the core electrons, i. e., the valence wavefunctions tend to have rapid oscillations in the ion cores region due to the requirement that they be orthogonal to core states. In other words, in the atomic core regions the valence electron orbitals have oscillations minima, maxima and nodes. This entails that a huge number of plane waves (PWs) $\phi_{\mathbf{K}+\mathbf{G}(\mathbf{r})} = \frac{1}{\sqrt{V}} e^{i(\mathbf{K}+\mathbf{G})\mathbf{r}}$ have to be used in order to reproduce the correct oscillations within the ion core regions with short length scale. If all PWs with large values of the reciprocal lattice vector (\mathbf{G}) such that $|\mathbf{G}| \leq G_{max}$ where G_{max} is accounted by the cut-off energy, $E_{cut} = \frac{\hbar^2 G_{max}^2}{2m}$, are included, the total number of PWs will be scaled by G_{max}^3 . The accompanying numerical efforts make forbidden the use of PWs to expand core electron wavefunctions and true valence electron wavefunctions in the core regions. Consequently, pseudopotentials methods are applied which lead to pseudowavefunctions for the valence electrons. However, such techniques based on energy-independent pseudopotentials either denominate "hard" (norm-conserving) [94, 95] or "ultrasoft" [96] pseudopotentials fail in order to restore the actual valence wavefunctions. The *pseudofunctions* $\tilde{\psi}_v$ are chosen to be smooth inside the ion core regions, i. e., ignoring its oscillation there. However, in the same time they should be identical to the actual wave functions outside the atomic core regions. Since this is the necessary condition for correct description of the chemical bonding in order to ensure the realistic predictions of the electronic properties of materials.

Based on that, Blöch [31, 93, 97, 98] suggested a new methodology for "exact" wavefunctions of valence electrons, the so-called *Projector Augmented-Wave* (PAW) method that is a generalization of the pseudopotential and linear augmented-plane-wave methods (LAPW). The underlying Blöch's idea arose from the *exact partitioning* of the wavefunctions [31, 93, 97, 98] and brought new concepts in pseudopotential methods owing their advantages. For instance, the accuracy of the description of full wavefunctions is high and comparable in the same quality of all-electrons methods. Also it has high computational benefits owing the very small number of PWs required to expand the smooth part of the full wavefunctions of the electrons in the valence regions. Such *exact partitioning* splits the true wavefunction ψ_v into three parts

$$\psi_v = \tilde{\psi}_v + \chi_v - \tilde{\chi}_v, \quad (2.102)$$

where $\tilde{\psi}_v$ is smooth in everywhere, but exact outside the core regions. The function χ_v is exact inside the ion core regions, usually called "augmentation regions" in the PAW method, but smooth tending to zero in the valence regions. It means that all necessary nodes of the true all-electron function ψ_v will be incorporated. By the end, the function $\tilde{\chi}_v$ in the "augmentation regions" and the same as χ_v outside of them [93, 97]. This approach accounts for the χ_v and $\tilde{\chi}_v$ as a highly localized functions inside the core and tending to zero outside of

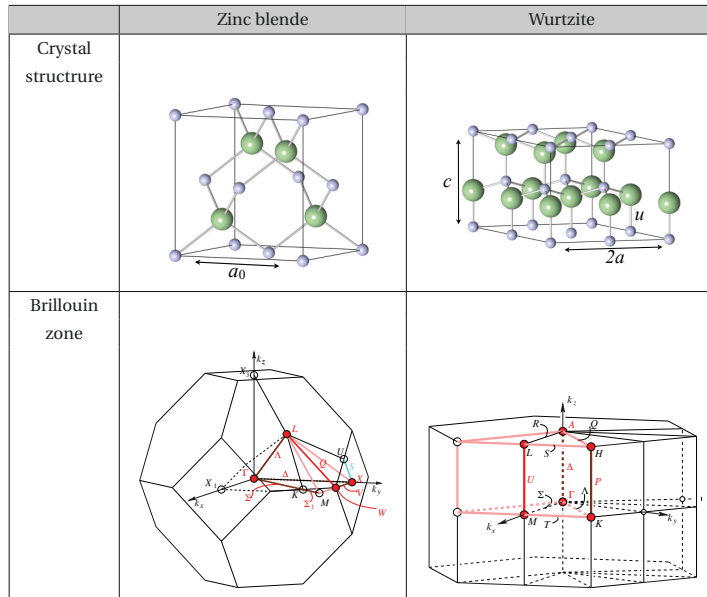


Figure 2.3: Hexagonal (wurtzite) and cubic (zincblende) crystal structures and their respective Brillouin zone [99]. Non-primitive cells that contain four primitive one, in wurtzite case, are displayed. The lattice parameters and high symmetry points are denoted.

them, whereas the $\tilde{\psi}_\nu$ is a pseudowavefunction that can be expanded in PWs. In praxis, to combined the wavefunctions in the PAW sphere regions a projector-technique using wavefunctions from all-electron calculations for free atoms is applied. [40, 97]

In this work the PAW method [40, 97] is used in order to generate the atomic pseudopotentials taking the interaction among core-valence electrons into account. In the region between the atomic cores, the wavefunctions are expanded into plane waves up to 400 eV for the cutoff energy. It is sufficient to yield converged results for wurtzite and zinc-blende AlN, GaN and InN polytypes, as well as $\text{In}_x\text{Al}_{1-x}\text{N}$ and $\text{In}_x\text{Ga}_{1-x}\text{N}$ pseudobinary alloys. Moreover the N $2s$, N $2p$, In $4d$, In $5s$, Ga $3d$, Ga $4p$, Al $3s$ and the Al $3p$ electrons are included in the valence shells of the pseudopotentials for N, In, Ga, and Al, respectively, for the calculation of the structural, electronic, and optical properties of the III-nitride alloys as well as their binaries end components.

2.4.2 Brillouin zone sampling

The exact description of the ground state and excited state properties, in part, depends on the sampling of the Brillouin zone (BZ) Fig. 2.3. Here, in order to obtain converged results for the ground state properties for binaries end components as well as pseudobinary alloys, different \mathbf{k} point meshes were used. A $8 \times 8 \times 8$ ($8 \times 8 \times 6$) Monkhorst-Pack (MP) [100] meshes have been used for *zb*-AlN (*wz*-AlN) and $16 \times 16 \times 16$ ($16 \times 16 \times 12$) meshes for *zb*-GaN and *zb*-InN and (*wz*-GaN and *wz*-InN). In the case of the $\text{In}_x\text{Al}_{1-x}\text{N}$ and $\text{In}_x\text{Ga}_{1-x}\text{N}$ alloys with 16-atom supercells the BZ was sampled using a $2 \times 2 \times 2$ mesh in order to compute the total energy of the 22 cluster classes. However, to ensure converged results for the QP energies, the BZ is sampled by a finer $3 \times 3 \times 3$ \mathbf{k} -point mesh.

For optical properties the calculations of the dielectric function in a wide energy range including excitonic effect require much more refined \mathbf{k} -point meshes in Eq. (2.90) where for

all these mesh points the excitonic matrices Eq. (2.87) have to be constructed. The accuracy requirements are much higher [64, 101] compared to the independent-quasiparticle approximation (IQPA) [102]. At least 10 times more \mathbf{k} -points is needed. The excitonic effects are usually more important for not too high interband and hence low photon energies near the absorption edge. This especially holds for excitonic bound states. Their treatment asks for a further refinement of the BZ sampling. In praxis, in this energy range the calculation of the DFs can be performed for hybrid meshes with varying densities [64]. More in detail: (i) Many MP \mathbf{k} -mesh points of a $9 \times 9 \times 9$ mesh are employed for pair energies below the absorption edge 3.5 eV (6.3 eV) of GaN in InGaN (of AlN in InAlN), respectively. (ii) Up to 10 eV, the DFs are sampled by $6 \times 6 \times 6$ MP \mathbf{k} -mesh points and, (iii) all higher excitations up to 20 eV are computed using a less dense $4 \times 4 \times 4$ MP \mathbf{k} -mesh. In addition, all \mathbf{k} meshes that are used for the calculation of the DFs were shifted by a small random vector. This shift of the entire mesh lifts symmetry induced degeneracies inherently present in MP \mathbf{k} -point sets and, therefore, improves the convergence of the respective optical quantities [103]. Together with the huge number of conduction bands this leads to excitonic Hamiltonians with ranks of up to 150000. Direct diagonalization of such matrices is prohibitively expensive and, hence, we make use of the time-evolution method [83] instead, where only matrix-vector multiplications occur.

2.4.3 Exchange and correlation

Ground-state properties such as the structural, energetic and elastic are derived from total-energy minimizations within DFT [12, 13]. Both the local density approximation (LDA) and the semi-local generalized-gradient approximation (GGA) for the XC functional are common, [13] but, according to the test calculations the choice of the XC functional affects the total energy and consequently the atomic geometry of the system. It has been found that the LDA tends to an overbinding, i.e., leading to lattice constants that are $\approx 1\%$ smaller than found in experiment, whereas the used GGA functional underestimates the binding and yields too large lattice constants (by up to 2%) as will be demonstrated in the next chapter.

In contrast, the recently developed AM05 XC functional seems to overcome some of the shortcomings related to earlier versions of the GGA. It has been designed to treat systems with varying electron densities (for instance systems that are composed of bulk- and surface-like regions) by exploiting the subsystem functional scheme (cf. sec. 2.1.3.3). In this work, the LDA, PBE type GGA and AM05 XC functionals were used in order to compute the ground state properties of the end components AlN, GaN, and InN. More in detail, we have used the Ceperley-Alder parametrization [43] for PAW-LDA whereas for AM05 and GGA the PAW-PBE by Perdew, Burke, and Ernzerhof [49] is applied.

2.4.4 HSE06 hybrid functional

In Sec. 3.2 it was mentioned that computing QP energies by means of first-order of perturbation theory, an initial electronic structure is needed that is closer to the final self-consistent QP solution than the KS eigenvalues and eigenstates computed within LDA or GGA. We followed the idea of Fuchs et al. [61] and used the HSE06 electronic structure as a starting point for the computation of the QP corrections. The HSE06 range parameter $\omega = 0.15 \text{ a.u.}^{-1}$ combined with the one quarter ($\alpha = 0.25$) of the nonlocal Hartree-Fock exchange and with the three quarters of the local exchange of the PBE-GGA functional has proven to work well for nitrides. [61]

2.4.5 Spin-orbit interaction and cristal-field splitting

There is an enormous number of calculations of the crystal-field splittings in semiconductors in geral based on the DFT within the LDA or including GGA. However, only in a few DFT-LDA or -GGA treatments of nitrides [104–107] spin-orbit interaction has been included. In addition, the DFT calculations exhibit the above-discussed band gap problem due to the neglect of the excitation aspect. One has to taken into account QP excitation effects within Hedin's *GW* approximation as well as the spin-orbit interaction. However, a DFT+SOC+*GW* approach demands high computer costs because non-collinear spins have to be taken into consideration. The spin is not anymore conserved and the Green function as well as the self-energy have to be replaced by 2×2 matrices. In order to avoid the related complications we have used an approximate inclusion of SOC effects in the computation of the QP band structures. In the case of group-III nitride (see Sec. 3.2.4) the changes in the DFT eigenvalues due spin-orbit interaction are smaller than, e. g., In(P, As, Sb) in group III-V semiconductors [108]. It means that the SOC influence on the XC self-energy matrix elements and W is small. Furthermore, the used HSE06 method for the zero-order approximation at the QP eigenvalues can be easily handled together with SOC. Hence, the corresponding QP energies including SOC are computed applying a QP shift obtained from the HSE06+*GW* calculation over the HSE06 eigenvalues computed taking SOC in consideration.[109, 110]

2.4.6 Screening in W

The screened potential W in the XC self-energy (see Eq. 2.83) is computed with matrices of the inverse dielectric function that have been computed by means of HSE06 wavefunctions and eigenvalues within the independent-particle approximation. Explicitly we use the implementation described in Ref. [111].

The description of the screening of the attractive electron-hole interaction that enters W in Eqs. (2.87) and (2.88) by means of a model dielectric function[112, 113] requires the static electronic dielectric constant ϵ_∞ for each cluster material. Here we use the values calculated

within the random-phase approximation using the DFT+ U scheme (see below) and averaged over the two independent components of the dielectric tensor.

2.4.7 Number of bands

Within the QP approach the number of bands is essential and must be taken into account. Especially in the case when computing the dielectric matrices for the GW approximation of the Σ . Based on that, in this work, it was used a number of 1250 bands in order to compute the ground state properties and QP bandstructures of the AlN, GaN and InN binaries end components, as well as the $\text{In}_x\text{Al}_{1-x}\text{N}$ and $\text{In}_x\text{Ga}_{1-x}\text{N}$ pseudobinary alloys in 16 atom supercells. However, taken optical properties in account, this number of bands together to the dense \mathbf{k} -point mesh, e. g., $9 \times 9 \times 9$ leads to too large excitonic Hamiltonians Eq. (2.86) and hence is extremely expensive in both memory as well as computer time. Then, a number of up to 210 conduction bands was use in order to predict the optical properties for systems with 16-atom supercells. In this case the excitonic Hamiltonians rank up to 150000 and by means of the time evolution method [83].

2.4.8 Equation of state

The Murnaghan equation of state (EOS) [114] used in this work is a useful and widely used tool in the treatment of pressure effects on the properties of solids state in the low-compression range. By fitting the calculated $E_{tot}(V)$ with E_{tot} as the total energy of the electronic system Eq. (2.24), but increased by the energy of the core-core repulsion. Its derivative with respect to volume (V) one obtains the theoretical equilibrium unit cell volume V_0 and some other properties, such as the isothermal bulk modulus B_0 , and its first derivative B'_0 with respect to pressure. In paxis the total energy is computed by DFT for several cell volumes and fit the resulting volume dependence of the total energy. In each case, it was computed fully relaxed atomic positions, i.e., optimized lattice constants and internal cell parameters, ensuring that the forces acting on the ions are below 5 meV/Å.

2.4.9 LDA+ U + Δ scheme

In order for the LDA+ U + Δ scheme to work, the DFT+ U gap has to be finite for all the cluster materials. Unfortunately this is not the case when the AM05 functional is used for InN [115]. Even, increasing the U parameter to unrealistic values a fundamental gap cannot be opened. For that reason we use the LDA, as parametrized by Ceperley and Alder [43], to describe the XC functional in the LDA+ U method. This procedure opens a gap for InN from LDA, however, the resulting gap values are still too small in comparison to the HSE+ G_0W_0 results. This discrepancy is described by a scissors operator Δ .

The scissors operator Δ to shift rigidly the conduction bands toward higher energy is

adjusted for each cluster j so that the fundamental gap is identical with the HSE+ G_0W_0 result for each cluster published elsewhere [116]. Indeed for each cluster class j such a scissors shift Δ_j has been computed. The shifts vary non-linearly with n_j (cf. Appendix A.3).

2.4.10 Excitonic effects

Concerning to the optical properties, the excitonic and local field effects are essential in order to describe the mutual electron-hole Coulomb interactions. These effects are computed by means of the solution of the BSE as implemented in VASP 4.4, whose solution of the excitonic Hamiltonian as well as the eigenvalues and eigenfunctions depends on the VASP 5.1.39 inputs such as wave functions, optical-transitions matrix elements and QP energies. Details are described in Ref. [117] and references therein.

3

AlN, GaN and InN polytypes as binary end components: Influence of exchange and correlation on structural and electronic properties

*"Ser profundamente amado por
alguém nos dá força; amar alguém
profundamente nos dá coragem"*

Lao-Tse

For modeling III-nitride alloys, in principle, it is necessary to understand the main properties of their constituents. Even though the basic semiconductor alloy concepts are understood at this time, the determination of many properties has been hampered by a lack of definite knowledge of many parameters of their end components. Thus, group III-nitrides compounds and their alloys have received a lot of attention along the last years. The intense research have driven a substantial progress in the knowledge of their properties and material quality from the experimental point of view.[18]

The three group-III nitrides AlN, GaN, and InN crystallize in the wurtzite (wz) structure under ambient conditions, which corresponds to the $P6_3mc$ (C_{6v}^4) space group for vanishing strain in the samples. They can also be grown in the cubic zinc-blende (zb) structure with space group $F\bar{4}3m$ (T_d^2) by means of different epitaxy techniques such as MBE or MOVPE.[15–17] However, even though high-quality films of AlN, GaN and InN have been synthesized, research and applications were limited since large single crystals cannot be grown. Therefore, existing experimental studies are usually restricted to investigations of epitaxial layers and, hence, may be influenced by the respective substrate, the interfaces, and spontaneous as well as piezoelectric fields. Correspondingly, a large variety of experimental results exists. [15–17]

Recently, remarkable progress in the determination of band gaps, effective masses, and $\mathbf{k} \cdot \mathbf{p}$ parameters has been made for the nitrides by applying quasiparticle electronic-structure theory (based on the $OEPx+G_0W_0$ approach[118] or the self-consistent GW method[119]). However, these calculations have not taken spin-orbit coupling (SOC) into account neither

for the wz nor the zb polytype. Such calculations are now possible [54]. For different group-II oxides the influence of SOC has been successfully included in calculations of the electronic structure and proven to be important.[92, 110, 120]

For this purpose, this chapter provides a systematic study of structural energetic and electronic properties of AlN, GaN and InN binary end components. They have been performed using the most modern state-of-art quasiparticle methods upon inclusion of the SOC. The influence owing different XC functionals on wz and zb polytypes of the group-III nitrides AlN, GaN, and InN are investigated and also, lattice parameters obtained from three different approximations to XC within DFT [54] are employed

The resulting lattice parameters a_0 (for zb polytype) as well as a , c , u , and c/a (for wz polytype) as derived from the DFT calculations using three different local and semilocal approximation for the XC functional are reported along with the bulk moduli B_0 and their pressure derivatives B'_0 in Table 3.1. From comparison to experimental values[121–124, 126] it is confirmed that the LDA leads to an overbinding for the group-III nitrides; the optimized lattice constants are smaller than the measured values. In contrast, the lattice parameters turn out to be larger when the PBE-GGA is used to describe XC, which corresponds to the underbinding mentioned before.

Interestingly, the AM05 functional indeed yields lattice constants in close agreement to experiment [121, 123, 124] for AlN and GaN polytypes. The small overestimation of $< 0.6\%$ for the a_0 , a , and c lattice constants obtained for InN using the AM05 functional can be a consequence of the fact that the layers used in the measurements might not be completely unstrained, defect-free, and polytype-pure. Thus, the excellent agreement of the AM05 lattice constants with measured values for AlN and GaN leads us to believe that this functional also gives reliable lattice constants for InN.

In contrast to what is observed for the lattice constants a and c of the wz crystals, the c/a ratio and the u parameter are rather independent of the description of XC (cf. Table 3.1). There are only very small changes along the functionals LDA, AM05, and PBE-GGA. Along the row wz -AlN, wz -GaN, and wz -InN u takes a less pronounced minimum for GaN. The experimental u parameter decreases monotonously towards the ideal tetrahedron value of $u = 0.375$, in agreement with the fact that this parameter is almost indirectly proportional to the bond ionicities calculated as charge asymmetry coefficients $g = 0.794$ (AlN), 0.780 (GaN), and 0.853 (InN)[127]. The non-monotonous behavior of the c/a ratio for both computed and measured values when going from AlN over GaN to InN is because GaN and InN (as opposed to AlN) have shallow d electrons. The values remain below the ideal ratio $c/a = 1.633$ in agreement with the theoretical prediction [128] that for $c/a < 1.633$ a compound crystallizes in wz structure under ambient conditions. A similar non-monotonous behavior is observed for the stability of the polytypes as described by the total energy differences between zb and wz , $\Delta E_{\text{tot}} = E_{\text{tot}}(zb) - E_{\text{tot}}(wz)$. The ΔE_{tot} (cf. Table 3.1) exhibit a minimum for GaN, indicat-

		AM05	LDA	PBE-GGA	Expt.
<i>zb</i> -AlN	a_0	4.374	4.343	4.402	4.37[121]
	Ω_{pair}	20.922	20.482	21.328	
	B_0	204.7	212.0	193.2	202[122]
	B'_0	4.38	3.22	4.16	
	ΔE_{tot}	47	46	41	
<i>zb</i> -GaN	a_0	4.495	4.465	4.547	4.49[123]
	Ω_{pair}	22.710	22.257	23.509	
	B_0	181.9	188.8	172.0	190[122]
	B'_0	4.07	4.44	3.36	
	ΔE_{tot}	15	14	18	
<i>zb</i> -InN	a_0	5.005	4.959	5.059	4.98[121]
	Ω_{pair}	31.346	30.493	32.371	
	B_0	130.8	144.7	120.2	136[122]
	B'_0	4.07	4.95	4.10	
	ΔE_{tot}	24	24	70	
<i>wz</i> -AlN	a	3.112	3.088	3.129	3.11[124]
	c	4.976	4.946	5.018	4.978[124]
	c/a	1.599	1.601	1.603	1.601[124]
	u	0.380	0.379	0.379	0.382[124]
	Ω_{pair}	20.869	20.420	21.276	
	B_0	202.3	210.8	187.2	185[125]
	B'_0	4.36	3.95	4.02	5.7[125]
<i>wz</i> -GaN	a	3.181	3.158	3.217	3.19[124]
	c	5.180	5.145	5.241	5.166–5.185[124]
	c/a	1.628	1.629	1.629	1.627[124]
	u	0.376	0.376	0.376	0.377[124]
	Ω_{pair}	22.698	22.219	23.488	
	B_0	183.2	197.4	172.2	188[125]
	B'_0	4.17	4.23	4.63	4.3[126]
<i>wz</i> -InN	a	3.549	3.517	3.587	3.54[126]
	c	5.736	5.685	5.789	5.718[124]
	c/a	1.616	1.616	1.613	1.613[126]
	u	0.378	0.377	0.378	0.375[122]
	Ω_{pair}	31.293	30.451	32.253	
	B_0	131.3	145.3	120.9	125.5[126]
	B'_0	4.76	4.52	5.37	12.7[126]

Table 3.1: The cubic lattice constant a_0 (in Å) and the hexagonal lattice parameters a , c (in Å) as well as c/a and the internal parameter u are given for AlN, GaN and InN polytypes. The volume per cation-anion pair Ω_{pair} (in Å³) is also listed. In addition, also the bulk moduli B_0 (in GPa) and their derivatives with respect to pressure B'_0 as derived from fits to the Murnaghan equation of state are given. The difference of the total energies ΔE_{tot} in (meV/pair) between the *zb* and the *wz* polymorphs is included. Results are derived from calculations using the LDA, PBE-GGA, and AM05 XC functionals and, for comparison, experimental values are listed.

ing that *zb*-GaN most likely can be grown not too far from equilibrium, whereas that would be more difficult for AlN and InN from an energetical point of view. The ΔE_{tot} in Table 3.1 are in rough agreement with values obtained from DFT-LDA.[128]

3.1 Energetic, structural and elastic ground-state parameters

The pair volumes $\Omega_{\text{pair}}^{zb} = 1/4 a_0^3$ and $\Omega_{\text{pair}}^{wz} = \sqrt{3}/4 a^2 c$, that are occupied by one cation-anion pair, are practically the same for the *zb* or *wz* polytypes of each material. In addition, it is found that they increase along the row AlN, GaN, InN (for instance $\Omega_{\text{pair}}^{zb} = 20.9, 22.7,$ and 31.3 \AA^3 as derived using the AM05 functional), which matches the trend of an increasing sum of the covalent radii of the anion and the cation: 1.93, 2.01 and 2.19 Å.[129] Moreover, due to the aforementioned overbinding, the volumes of the unit cells calculated using the LDA are smaller than the ones obtained with the AM05 functional. The PBE-GGA leads to the largest unit-cell volumes, which is in agreement with the underbinding mentioned above.

Still analyzing the ground state parameters, the inverse compressibility B_0 increases along the row InN, GaN, and AlN when the same XC functional is used. B_0 of one and the same

material also increases when going from PBE-GGA over AM05 to LDA (cf. Table 3.1). Furthermore, there is an influence of the polytype on B_0 : In the case of AlN the values for zb are larger than the wz ones, while the opposite is true for GaN and InN. This seems again to be a consequence of the contributions of the Ga $3d$ or In $4d$ electrons, respectively, to the chemical bonding. Comparing the calculated B_0 to experimental values [125, 126] shows that the agreement is quite good for the zb polymorphs when AM05 is used. For the wz polymorphs of GaN and InN the measured values are in between the PBE-GGA and AM05 ones. The pressure coefficients B'_0 vary between 3–5 and no clear trend for different XC functionals or materials is spotted. The large value of $B'_0 = 12.7$ measured for wz -InN [126] arises probably due to sample-quality issues.

3.2 Quasiparticle electronic structure

Usually it is sufficient to treat the self-energy effects within first-order-perturbation theory.[130] This approach of calculating QP eigenvalues $\varepsilon_v^{\text{QP}}(\mathbf{k})$, where v is the band index and \mathbf{k} the Bloch wave vector in the BZ, is called G_0W_0 . For relatively homogeneous electronic systems the G_0W_0 corrections to the KS eigenvalues from DFT-LDA or DFT-GGA lead to electronic band structures (see Fig. 3.1) that are in reasonable agreement with measurements.[26]

However, for compounds with first-row elements, such as the nitrides, the LDA/GGA+ G_0W_0 procedure still underestimates the band gaps. [61] The idea of an iterative solution of the QP equation seems to be more promising,[130, 131] unfortunately it is inherently linked to a much higher computational cost. Therefore, computing the QP energies from one step of perturbation theory, based on an initial electronic structure that is closer to the final self-consistent solution than the KS eigenvalues and eigenstates are, is an efficient alternative. Here we use an improved starting point by solving a generalized KS equation with a spatially non-local XC potential.[61, 71] More precisely the HSE hybrid functional (cf. sec. 2.1.3.4) is used to be the start point to the GW calculations. It has proven to work well for AlN, GaN, and InN polytypes.[61, 109] It effectively simulates the screened-exchange contribution to the GW self-energy in the zero'th approximation. This contribution substantially opens gaps and other interband distances.

In the precedent section has been shown that the atomic geometries obtained using the AM05 XC functional agree better with measured results than the LDA or PBE-GGA ones. Hence, only results for the electronic QP energies based on the AM05 geometries are presented.

In Bechstedt et al.[133] and Riefer et al.[101] the HSE+ G_0W_0 approach has been applied to the DFT-LDA geometries of InN (AlN). According to Table 3.1, the LDA or PBE-GGA geometries are used to study atomic structures that are hydrostatically strained with respect to the AM05 equilibrium geometries. In these cases the indirect influence of the XC functional used in the ground-state studies within DFT on the electronic structure (via the atomic geometry)

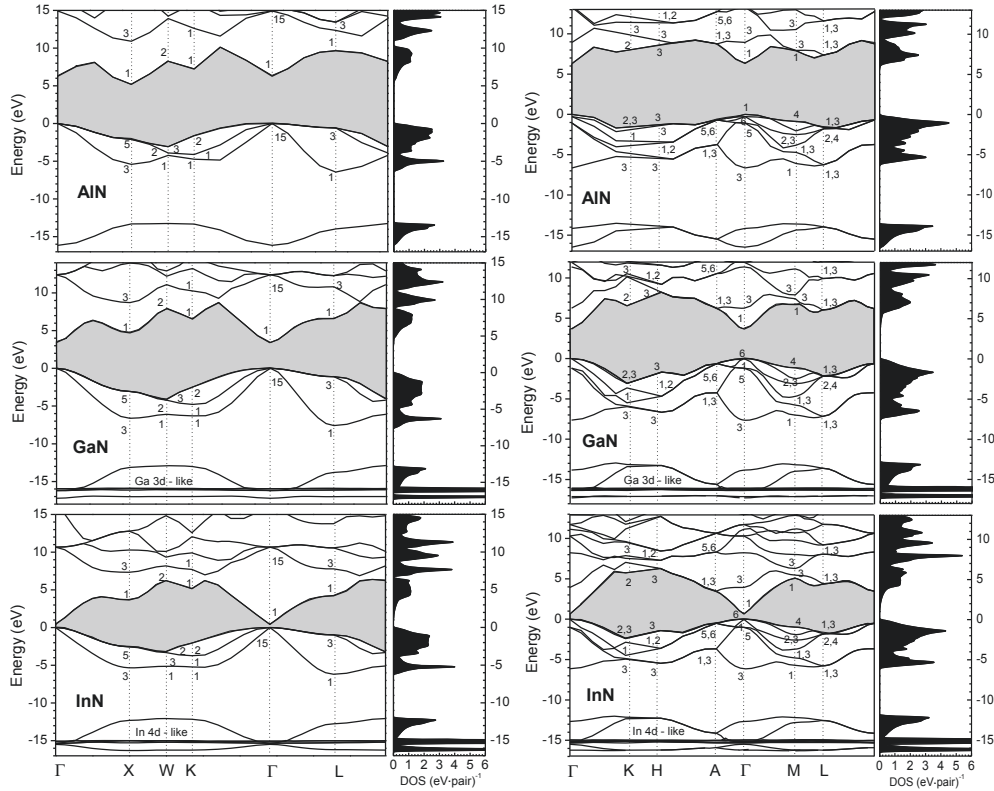


Figure 3.1: QP band structures and DOS without spin-orbit interaction for *zb*-AlN, *zb*-GaN, and *zb*-InN. The numbers indicate the irreducible representations at the respective high-symmetry points using the notation according to Bouckaert, Smoluchowski and Wigner (see Yu et al.[132]). The Γ_{15} VB maximum is used as energy zero. The fundamental band gap is indicated by the shaded region.

and the direct influence of XC according to the GW self-energy are discussed together.

3.2.1 Band structures and DOS

The QP band structures of AlN, GaN, and InN calculated for the *zb* (*wz*) AM05 atomic geometries are shown along with the corresponding DOS in Fig. 3.1. Since the spin-orbit splittings are small, they are not shown in this figure and the notations of the irreducible representations are given accordingly.[132, 134, 135] All band structures show a pronounced minimum of the lowest conduction band (CB) near the BZ center Γ . The dispersion of this band around Γ increases along the row AlN, GaN and InN, thereby closing the fundamental energy gap. This can be explained by the In 5s and Ga 4s levels being lower in energy than the Al 3s one[115] and the reduction of the interatomic interaction along the row AlN, GaN, and InN.[136] The strong CB dispersion is also visible by the low state density in the lowest part of the empty DOS (see Fig. 3.1). Another reason that the gaps of InN and GaN are much smaller than the one of AlN is the remarkable *pd* hybridization in both materials.[137] This effect causes a strong *pd* repulsion at Γ which is not present for AlN and hence renders *zb*-AlN an indirect semiconductor with a CB minimum situated at the X point.

As can be seen in Fig. 3.1, the *d* electrons also influence the VB structure. More specifically, it is observed that the ionic gap between the uppermost three (twofold spin degenerate) *p*-like VBs and the lowest (twofold spin degenerate) *s*-like VB does not follow the trend of the charge asymmetry coefficients *g*.[127] The reason for this behavior is the energetic overlap

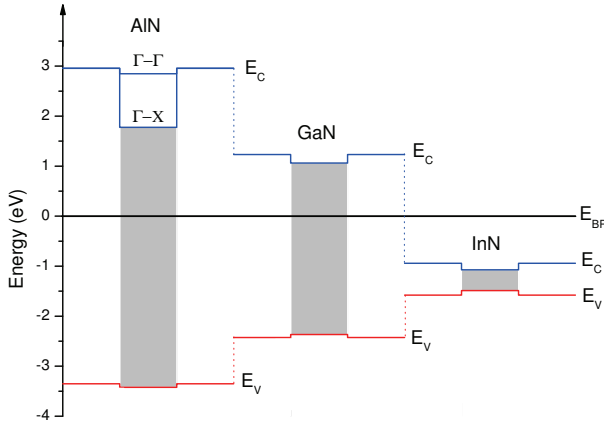


Figure 3.2: Band line-ups for cubic inclusion embedded in hexagonal environment from QP calculations. The branch-point energy (here: energy zero) and the values from Table 3.2 have been used for alignment. The shaded areas illustrate the fundamental gaps in the regions of the cubic inclusions.

of the N $2s$ states and the Ga $3d$ or In $4d$ states, respectively, the so-called sd hybridization. This effect is symmetry-forbidden at Γ , [138] however, for zb -GaN and zb -InN it leads to a splitting into a lower and an upper split-off band for all \mathbf{k} -points away from the BZ center. In addition, four dispersionless low-lying bands appear at -16 eV (GaN) or -15 eV (InN). All these bands give rise to pronounced peaks in the DOS which are clearly visible in photoemission experiments. [139]

3.2.2 Band alignment and cubic inclusion in wurtzitic structures

Recently it has been demonstrated experimentally that nitride nanowires (NWs) (e.g. made by GaN) can be grown as cubic polytype by plasma-assisted MBE despite the wz favorization in bulk. [140] The corresponding luminescence lines in zb -GaN are shifted towards lower energies by 0.2 eV with respect to wz -GaN. However, there is also an intense luminescence peak in between which is attributed to excitons bound to stacking faults that form at the cubic-hexagonal interface. Stacking changes have been also observed by other groups. [141]

The observation of a stacking variation in $[0001]/[111]$ direction suggests the possibility of polytypic superlattices or, in general, heterocrystalline structures [142] also for the group-III nitrides. Their properties are determined by the electronic states in the entire system and the line-up of the allowed empty or occupied bands at the interface between the wz and zb polytypes depicted in Fig. 3.2. The key questions concern the magnitude and sign of the band discontinuities between wz matrix and cubic inclusion, especially the localization of the highest occupied or lowest empty electronic states in a heterocrystalline but homomaterial system.

In this section these questions are answered using our approach to the *ab initio* electronic structure. We calculate the natural band discontinuities ΔE_v and ΔE_c between the valence bands and conduction bands, respectively, of zb and wz nitrides (cf. Tabela 3.2). The positive sign of ΔE_v (or ΔE_c) indicates that the embedded cubic inclusion represents a quantum well for holes (or electrons) in the cubic regions. Thereby, $\Delta E_v \cdot \Delta E_c > 0$ describes a type-

		E_g	E_{BP}	E_c	E_v	ΔE_c	ΔE_v
AlN	zb (Γ - Γ)	6.271	3.422	2.849	-3.422	0.108	-0.069
	zb (Γ - X)	5.198		1.776		1.181	
	wz	6.310	3.353	2.957	-3.353		
GaN	zb	3.427	2.366	1.061	-2.366	0.170	0.062
	wz	3.659	2.428	1.231	-2.428		
InN	zb	0.414	1.487	-1.073	-1.487	0.131	0.093
	wz	0.638	1.579	-0.941	-1.579		

Table 3.2: Energy gap E_g and branch-point energies E_{BP} (with respect to the valence-band maximum) for zb and wz nitrides. For zb -AlN besides the direct Γ - Γ gap also the smaller indirect Γ - X gap is listed. The resulting absolute positions of the conduction band minimum E_c and valence band maximum E_v as well as the natural band discontinuities ΔE_c and ΔE_v between zb and wz are also given. The energy values have been derived from the QP eigenvalues computed within the HSE06+GW approach [71].

I hetero(crystalline)structure while $\Delta E_v \cdot \Delta E_c < 0$ gives rise to a type-II hetero(crystalline) structure. Here we use a "macroscopic" approach [143] which only requires the calculation of the QP band structures of the corresponding bulk compounds. The energy alignment of the two band structures for the cubic and hexagonal nitride polytypes asks for a common universal reference level. Frenslley and Kroemer [144] suggested to use an internal reference level which may be pinned at the interface in the presence of virtual gaps states. It may be identified with the branch-point energy.[145, 146] In the spirit of the Shockley-Anderson model [147] the vacuum level takes over the role of the reference level if no interface states are present. The vacuum level is however strongly influenced by the electrostatic potential.

In a first step the branch-point energy E_{BP} of each material as common energy zero was applied. At the branch-point energy the band states change their character from predominantly acceptor-like (usually valence-band states) to mostly donor-like (usually conduction-band states) electronic states. According to Tersoff [145] the related charge transfer leads to an intrinsic interface dipole that tends to line-up the energy bands at both sides of an interface in a way that the dipole itself vanishes. We compute the reference levels E_{BP} according to an approximate method which was successful for several material combinations. [143, 146] The calculations have been performed using the QP band structure resulting from the full HSE06+GW scheme (Fig. 3.2). Although ionization energies and electron affinities are not explicitly derived, instead only the positions of the band edges E_c and E_v with respect to \bar{V} are determined. This procedure yields the same results as the Shockley-Anderson model with the vacuum-level alignment. [147] We find that the displacements $\Delta \bar{V}$ due to the potential differences between zb and wz are small, $\Delta \bar{V} = 0.15$ eV (AlN), 0.01 eV (GaN), and 0.03 eV (InN). The second type of "natural" band discontinuities ΔE_c and ΔE_v arises from the absolute band-edge positions with respect to \bar{V} in both polytypes.

The results for the band discontinuities ΔE_c and ΔE_v are given in Table 3.2 and Fig.3.2 together with those for the fundamental energy gap E_g and the corresponding relative positions E_c and E_v of the conduction-band minimum (CBM) and the valence-band maximum (VBM), respectively. In the case of zb -AlN the indirect Γ - X gap and the conduction band position E_c at the X point are listed in addition to the direct Γ - Γ gap. The computed values are slightly different from those given in Ref. [143] mostly due to the different atomic geometries used. The geometries optimized here by means of the AM05 XC functional are closer to the experimentally determined structures (cf. Table 3.1). We find that the band discontinuities ΔE_v and ΔE_c between zb and wz are relatively small. Only the CBM at X in zb -AlN exhibits

a large distance of about 1 eV to the CBM at Γ of wz -AlN. Thereby the absolute values of the band discontinuities are in general much larger in the conduction-band case whereas the valence bands are almost aligned (cf. Table 3.2). The important information is that the values are weakly dependent on the procedure. The average deviation of ΔE_c (ΔE_v) amounts to 36 meV for GaN and 32 meV for InN. Only for AlN the variation approaches larger values up to 0.1 eV for Γ - Γ or 0.2 eV for Γ - X . The positive signs indicate type-I heterocrystalline structures apart from the AlN case where the holes should not be localized within the cubic inclusion. In the case of the AlN cubic inclusions represent heterocrystalline structures of type-II where only the electrons are localized in the zb layers. The strength of the localization depends on the Γ or X character of the electrons. The almost vanishing valence band offsets between cubic and hexagonal group-III nitrides do not indicate the validity of the common anion rule. [148] On the contrary, Fig. 3.2 clearly shows large valence band offsets between two different wz group-III nitrides of about 0.93 eV (AlN-GaN) and 0.84 eV (GaN-InN) using the HSE06+GW and the BP alignment of the order of measured values [149, 150] despite the common anion.

The computed energy values in Table 3.2 are in rough agreement with other band structure calculations, especially for AlN and GaN. Examples are the values $\Delta E_c=0.162$ eV (AlN) and 0.154 eV (GaN) at Γ obtained from DFT-LDA computations without QP corrections. [151] Similar values of $\Delta E_c=0.150$ eV (GaN) and 0.120 eV (InN) have been obtained by Yeh et al. [152] The absolute values for the valence-band offsets are much smaller and may vary in sign. For instance, Murayama and Nakayama [151] (assuming that no dipole potential exists across the interface) found $\Delta E_v=-56$ (AlN) and -34 (GaN) meV. Dalpian and Wei derived a value of $\Delta E_v=-22$ meV for GaN [153] by using the (KS) eigenvalues of the core levels as calculated within DFT-GGA. These valence band discontinuities indicate a type-II heterocrystalline behavior which is different from the findings based on the alignment via the branch-point energy (cf. Table 3.2). However, this difference can most likely be attributed to the QP corrections which are missing in Ref. [153] Using the KS eigenvalues of the Ga3d states (calculated within GGA) to perform the energy alignment, we also found $\Delta E_v < 0$ in agreement with Dalpian and Wei. We state that the inclusion of the quasiparticle effects is important.

Using the averaged electrostatic potentials to achieve the energy alignment of the wz and zb band structures, contradictory but also similar results have been derived for the discontinuities within DFT-LDA. Stampfl and Van de Walle [154] predicted a type-II character with $\Delta E_c=0.27$ eV and $\Delta E_v=-0.07$ eV for GaN. The DFT-LDA superlattice calculations of Majewski and Vogl [155] qualitatively agree with our findings for AlN and GaN (cf. Table 3.2 and Fig. 3.2). They also report a band line-up for zb/wz leading to a type-I junction. [140] The values obtained by Majewski and Vogl including (neglecting) atomic relaxations of the interfaces are $\Delta E_v=0.02$ (-0.10) eV and $\Delta E_c=1.30$ (1.40) eV for AlN and $\Delta E_v=0.04$ (0.02) eV and $\Delta E_c=0.12$ (0.14) eV for GaN. The small differences between the values outside and inside the parenthesis indicate a weak sensitivity to the details of the computations. Nevertheless, for

unrelaxed interfaces with ($\Delta E_v = -0.10$ eV) [155] they also found a type-II heterocrystalline character for AlN, in contrast to the relaxed case. In a supercell calculation with slightly strained zb -GaN Majewski and Städele [156] confirmed the previous results with $\Delta E_c = 175$ meV and $\Delta E_v = 35$ meV for a type-I system. The results for GaN by Bandić et al. [157] are shifted with respect to those of Majewski and Vogl [155] since the interface dipole contribution described by the difference in electrostatic potentials is not taken into account.

Taking the accuracy of the band-structure and alignment methods into account, one has to point out that no final conclusion can be made for the valence-band line-up between cubic and hexagonal AlN. We have to point out that our results for GaN and InN, do not follow the simplified argument that the VBM of a pure compound in wz structure is usually higher than that in the zb structure.[153] This should be due to the crystal-field splitting which moves the uppermost occupied wz level toward higher energies. Indeed, this effect is present. However, we claim that the discussion of the band structures of isolated polytypes is insufficient. Rather, one needs an alignment via a reference level that accounts for the electrostatics at the interface.

Thereby, the manifold first-principles results ask for some comments: (i) In general, the (natural) valence-band offsets ΔE_v between zb and wz for the three nitrides are small, $|\Delta E_v| \leq 0.1$ eV, independent which approach has been used for this estimation.[158] Most important is the treatment of XC in the underlying electronic structure calculations. Conventional DFT results using GGA or LDA functionals are less reliable on predicting valence-band offsets than hybrid functionals or, much better, hybrid-functional based QP calculations. [159–161] (ii) The positive or negative values ΔE_v may depend on the internal or external reference level used to align the bulk bands on both sides of the zb/wz interface.

At first glance, the values $\Delta E_v > 0$ in Table 3.2 seem to violate the rule that the VBM in wurtzite should usually be higher in energy than that in zb crystals due to the crystal-field splitting and intervalence band repulsion that exist in wz . [153] However, the same alignment procedure and electronic structure calculations lead to values $\Delta E_v < 0$ for conventional III-V compounds GaAs, InP, InAs, and InSb. [162] We conclude that the crystal field itself with lattice parameters $c/a > 1.633$ and $u < 0.375$ for conventional III-V compounds (crystallizing in zb under ambient conditions) in wurtzite geometry and $c/a \leq 1.663$ and $u > 0.375$ for III-nitrides (usually crystallizing in wz) obviously determines the sign of the small $|\Delta E_v|$ values.

3.2.3 Fundamental gaps and their volume/pressure dependence

The fundamental gaps at the Γ point of the BZ for AlN, GaN, and InN in the zb and the wz structure are summarized in Table 3.3. They separate CB states of Γ_{1c} type from VB states of Γ_{15v} type for the zb crystals as well as Γ_{1c} -like CB states from Γ_{5v} -like (wz -GaN, wz -InN) or Γ_{1v} -like (wz -AlN) VB states. Here, the denotation is changed back from Fig. 3.1 (Γ_6 Rashba

		Geometry: AM05	Geometry: LDA	Geometry: PBE-GGA	Expt.
<i>zb</i> -AlN	E_g	6.271 (5.198)	6.659 (5.265)	6.071 (5.164)	5.93[163] (5.3)[163]
	α_V	-10.11 (-2.40)			
	α_P	49.4 (11.7)			
<i>zb</i> -GaN	E_g	3.427	3.609	3.158	3.3[123]
	α_V	-8.60			-7.9[123]
	α_P	47.3			40-46[123]
<i>zb</i> -InN	E_g	0.414	0.540	0.264	0.61[164]
	α_V	-4.48			
	α_P	34.2			3[123]
<i>wz</i> -AlN	E_g	6.310	6.553	6.144	6.28[165]
	α_V	-10.07			
	α_P	49.8			49[123]
<i>wz</i> -GaN	E_g	3.659	3.847	3.366	3.51[165]
	α_V	-8.52			
	α_P	46.5			37-47[123]
<i>wz</i> -InN	E_g	0.638	0.765	0.494	0.7[165],[15]
	α_V	-4.56			
	α_P	34.7			22-30[123]

Table 3.3: Energies E_g (in eV) of the fundamental band gaps at Γ obtained within HSE+ G_0W_0 . For the AM05 equilibrium geometry, the hydrostatic pressure coefficients α_P (in meV/GPa) and the volume deformation potentials α_V (in eV) of the fundamental band gap are given. In the case of *zb*-AlN the values in parenthesis refer to the indirect gap between Γ and X . The gaps resulting for the LDA and GGA geometries in Table 3.1 are also listed.

notation[135]) to the textbook version (Γ_5 Ref.[132]).

In addition, also the indirect fundamental gap of *zb*-AlN between X_{1c} -like and Γ_{15v} -like states is given in Table 3.3. These results clearly demonstrate that the approach applied in this work, i.e., calculating QP energies within the *GW* approximation based on an initial electronic structure from HSE, gives excellent fundamental gaps for the nitrides. While this is true for the atomic geometries obtained using the AM05 XC functional, the ones calculated based on the LDA (PBE-GGA) lead to an overestimation (underestimation) of the direct gaps in comparison to measured values. Thereby, it is found that the relative variation of the gap with the cell volume is most drastic for InN, while the influence on the indirect gap of *zb*-AlN is much weaker. This is a consequence of the opposite shifts of the Γ_{1c} and X_{1c} levels in *zb*-AlN when the volume changes.

Using the changes of the unit-cell volume due to the different XC functionals (cf. Table 3.1) and the fundamental band gaps, the hydrostatic band-gap deformation potentials $\alpha_V = \delta E_g / \delta \ln V$ are derived (cf. Table 3.3). They are slightly larger than values from an equally sophisticated QP approach.[118] The hydrostatic pressure coefficients $\alpha_P = -\alpha_V / B_0$ follow with the bulk moduli in Table 3.1. The results for α_V and α_P are in excellent agreement with measured values (see e.g. collection in Rinke et al.[118]).

In Table 3.4 the fundamental band gaps of the *zb* mononitrides are given as calculated based on the different equilibrium geometries (cf. Table 3.1) and using different levels of approximation for the XC self-energy. These numbers confirm that the KS eigenvalues obtained using a local/semi-local XC functional are smaller compared to the more sophisticated approximations. InN even turns out to be a zero-gap semiconductor in these cases since the ordering of the Γ_{1c} and the Γ_{15v} levels is inverted.[166] Including the screened-exchange contribution[69] by using the spatially non-local HSE functional shifts the electron and hole

	XC self-energy	AM05	LDA	PBE-GGA
<i>zb</i> -AlN	(semi-)local	3.198	2.977	3.312
	HSE	4.333	4.354	4.316
	HSE+ G_0W_0	5.198	5.265	5.164
<i>zb</i> -GaN	(semi-)local	1.843	1.925	1.572
	HSE	2.844	2.972	2.590
	HSE+ G_0W_0	3.427	3.609	3.158
<i>zb</i> -InN	(semi-)local	≈ 0.0	≈ 0.0	≈ 0.0
	HSE	0.325	0.416	0.206
	HSE+ G_0W_0	0.414	0.540	0.264

Table 3.4: Fundamental band gaps E_g (in eV) of *zb*-AlN, *zb*-GaN, and *zb*-InN calculated for the LDA, PBE-GGA, and the AM05 equilibrium geometries. Three different approximations for the XC self-energy are compared: (i) “(semi-)local” means that the same XC functional as for the calculation of the atomic geometry has been used. In addition, the gaps calculated using (ii) the HSE functional, and (iii) the HSE+ G_0W_0 approach are included.

eigenvalues in opposite directions.[26] Consequently, the gaps are by about 1 eV (AlN, GaN) or 0.3 eV (InN) larger than the KS gaps (cf. Table 3.4). In a next step, the correct screening (including its dynamics) as well as the Coulomb hole contribution[69] are taken into account by calculating QP energies within the G_0W_0 approximation. This leads to an additional increase of the gaps by about 0.9 eV (AlN), 0.6 eV (GaN), and 0.1 eV (InN), which corresponds to roughly 20 % of the true fundamental gap. Therefore, we find that eigenvalues obtained in an HSE calculation significantly improve over the DFT-LDA/DFT-GGA ones. However, only the full XC self-energy (as approximately calculated within the G_0W_0 approach) leads to QP gaps that are in good agreement with measured values.

3.2.4 Valence band splittings and spin-orbit interaction

The SOC is taken into account via a non-collinear description[132] within the calculation of the HSE electronic structure.[110, 120, 167] Currently, we have not fully developed a full HSE+ GW approach including non-collinear spins, moreover, the replacement of wave functions by spinors is not enough because of the coupling of orbital and spin motion. Hence, since the spin is not conserved,[81] a simple generalization of the available codes is difficult. However, since all orbital contributions to the mixed states are mostly p -like the same influence of the QP corrections can be expected for the spin-orbit-split band energies at a given Bloch wave vector. Consequently, the SOC should be almost uninfluenced by the QP effects. This especially holds for the small shifts starting from HSE close to the QP ones. The accuracy of this efficient approximation has been demonstrated for group-II monoxides.[110, 120, 167]

Without SOC (cf. Fig. 3.4) the VB maximum of the *zb* nitrides is a threefold degenerate state with $\Gamma_{15\nu}$ symmetry which splits into a $\Gamma_{8\nu}$ (fourfold degenerate) and a $\Gamma_{6\nu}$ (twofold degenerate) level in the presence of the spin-orbit interaction .[132] The corresponding $\Delta_{so} = \varepsilon(\Gamma_{8\nu}) - \varepsilon(\Gamma_{6\nu})$ are compiled in Table 3.5. These numbers show that the choice of the XC functional indirectly influences the splittings via the atomic geometry. However, there is no clear trend with the (overestimated or underestimated) lattice constants, since also the mixing of the p and d like levels changes and, hence, affects the SOC splitting (see below). Moreover, the values for Δ_{so} do not vary strongly for the different cubic group-III nitrides. The results in Table 3.5 agree well with values from previous DFT-LDA calculations[105] from which 20.0,

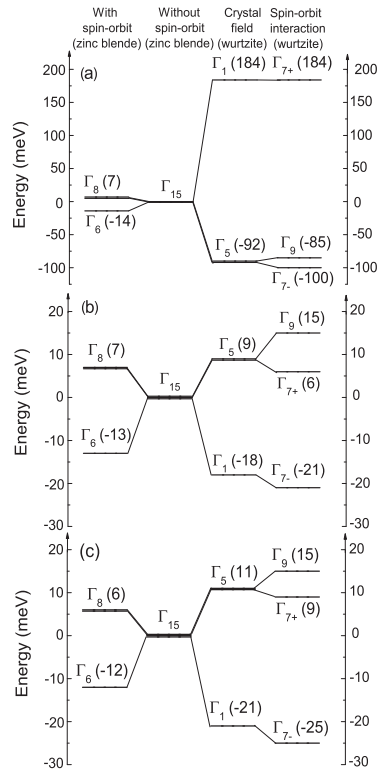


Figure 3.3: Characteristic splittings and shifts due to the crystal-field splitting and the spin-orbit interaction for (a) AlN, (b) GaN, and (c) InN. The absolute energy values (in meV) are given in parenthesis. The threefold degenerate Γ_{15} level of the zb polymorphs is used as energy zero.

18.5, and 12.6 meV was derived for AlN, GaN, and InN, respectively. Also the values $\Delta_{so} = 19$, 17, and 5 meV which have been recommended by Vurgaftman and Meyer [168] are very close.

In the case of GaN and InN the Δ_{so} are so small compared to AlN since the atomic spin-orbit splittings [169] for the Ga $4p$ (98 meV) and Ga $3d$ (-537 meV) electrons or the In $5p$ (264 meV) and In $4d$ (-958 meV) states, respectively, partially compensate each other because of the different signs [105]. This compensation arises due to the pd hybridization of atomic-like p and d states and leads to the values given in Table 3.5. Interestingly, for GaN and InN the spin-orbit splittings between $L_{4,5}$ and L_6 states, $\Delta_{so}(L)$, are larger than the respective splittings at the Γ point. In contrast to AlN, the rule [105] $\Delta_{so}(L)/\Delta_{so}(\Gamma) = 2/3$ is violated for GaN and InN. A similar effect has been observed for other tetrahedrally coordinated III-V compounds with relatively large differences of the covalent radii, for instance InP [170].

For wz crystals, in Fig. 3.4, the VB structure is more complex due to the hexagonal crystal field which leads to a crystal-field splitting. Hence, without SOC one finds the twofold degenerate Γ_{5v} and the non-degenerate Γ_{1v} states at the VB maximum. Thereby, we use the Bouckaert, Smoluchowski and Wigner notation [132, 134] Γ_{15v} which leads to Γ_{5v} and Γ_{1v} instead of Γ_{6v} and Γ_{1v} as in the Rashba denotation [135] applied in Fig. 3.1. The Γ_{5v} state splits into Γ_{9v} and Γ_{7v} levels and Γ_{1v} becomes a level with Γ_{7v} symmetry in the presence of SOC.

The values for the crystal-field splittings Δ_{cf} in Table 3.5 indicate a small influence of the GW corrections on the crystal-field splittings: the QP shifts towards lower band energies are larger for the Γ_{5v} states than for the Γ_{1v} states. Consequently, the QP corrections reduce the crystal-field splitting for wz -GaN and wz -InN by about 3–7 meV. In the case of wz -AlN an enlargement of the absolute value by about 17–20 meV is computed due to the negative sign

of Δ_{cf} . The absolute splittings in Table 3.5 are somewhat larger than the values recommended by Vurgaftman and Meyer.[18] However, the sign and, hence, the ordering of the $\Gamma_{5\nu}$ and $\Gamma_{1\nu}$ states are the same. Moreover, the values calculated in this work are in good agreement with other *ab-initio* calculations, e.g. collection in Bechstedt et al.[115] and references therein. The QP calculations without SOC in Rinke et al.[118] tend to overestimate the absolute values for Δ_{cf}^0 .

Within $\mathbf{k} \cdot \mathbf{p}$ theory the energy differences of the uppermost valence levels in a *wz* crystal, $\Delta E_1 = \varepsilon(\Gamma_{9\nu}) - \varepsilon(\Gamma_{7+\nu})$ and $\Delta E_2 = \varepsilon(\Gamma_{9\nu}) - \varepsilon(\Gamma_{7-\nu})$, can be described by[171]

$$\begin{aligned} \Delta E_{1/2} &= \varepsilon(\Gamma_{9\nu}) - \varepsilon(\Gamma_{7+/-\nu}) \\ &= \frac{1}{2}(\Delta_{\text{cf}} + \Delta_{\text{so}\parallel}) \mp \frac{1}{2} \sqrt{\left(\Delta_{\text{cf}} - \frac{1}{3}\Delta_{\text{so}\parallel}\right)^2 + \frac{8}{9}\Delta_{\text{so}\perp}^2}. \end{aligned} \quad (3.1)$$

In Eq. (3.1), $3i\Delta_{\text{so}\parallel} = \langle y | H_{sz} | x \rangle$ and $3i\Delta_{\text{so}\perp} = \langle z | H_{sx} | y \rangle = -\langle z | H_{sy} | x \rangle$ are the spin-orbit splitting parameters; the spin-orbit interaction H_{so} is divided according to $H_{\text{so}} = H_{sx}\sigma_x + H_{sy}\sigma_y + H_{sz}\sigma_z$ by means of the Pauli spin matrices σ (cf. section 2.1.2.3). Therein, $|x\rangle$, $|y\rangle$, and $|z\rangle$ describe the *p* like basis functions at Γ . In addition, Δ_{cf} represents the differences in the VB eigenvalues of the $|x\rangle$ ($|y\rangle$) and the $|z\rangle$ states.

However, Eq. (3.1) indicates a complication for both theory as well as experiment. In band-structure calculations and also in all spectroscopies only energy differences such as ΔE_1 and ΔE_2 are determined. Hence, only two numbers are available to determine the three band-structure parameters Δ_{cf} , $\Delta_{\text{so}\parallel}$, and $\Delta_{\text{so}\perp}$ from Eq. (3.1). If no additional assumption is made, the lack of one parameter for the determination of Δ_{cf} , $\Delta_{\text{so}\parallel}$, and $\Delta_{\text{so}\perp}$ leads to a parameter field $\Delta_{\text{so}\parallel} = \Delta_{\text{so}\parallel}(\Delta_{\text{cf}})$ and $\Delta_{\text{so}\perp} = \Delta_{\text{so}\perp}(\Delta_{\text{cf}})$ which is visualized in Fig. 3.4. One possible additional assumption to fix all parameters is the quasicubic approximation $\Delta_{\text{so}\parallel} = \Delta_{\text{so}\perp} = \Delta_{\text{so}}^{\text{qc}}$ and $\Delta_{\text{cf}} = \Delta_{\text{cf}}^{\text{qc}}$. Interestingly, when $\Delta_{\text{cf}} > 0$ (as found for GaN and InN) the resulting $\Delta_{\text{cf}}^{\text{qc}}$ are not very different from the values computed in the absence of SOC (cf. Table 3.5).

For $\Delta_{\text{cf}} < 0$ (AlN) a further increase of the absolute values is observed. In any case the quasicubic spin-orbit splitting constant $\Delta_{\text{so}}^{\text{qc}}$ is by nearly a factor of 2 (1.5) smaller than its *zb* value for InN (GaN), while there is no such deviation for AlN, which has no *d* electrons. This has recently been discussed for the first time,[109] and, according to the results of the present work, the recommendation[168] to choose the same spin-orbit splittings for *wz* and *zb* fails for compounds with shallow *d* electrons. Another additional assumption can be derived by identifying $\Delta_{\text{cf}} = \Delta_{\text{cf}}^0$ which leads to $\Delta_{\text{so}\parallel} \neq \Delta_{\text{so}\perp}$. Moreover, the ΔE_1 and ΔE_2 values in Table 3.5 indicate that Δ_{cf} , as computed using the eigenvalues without SOC, is almost in agreement with the average distance $\frac{1}{2}[\varepsilon(\Gamma_{9\nu}) + \varepsilon(\Gamma_{7+\nu}) - \varepsilon(\Gamma_{7-\nu})] = \frac{1}{2}[\Delta E_1 + \Delta E_2]$ between the valence levels including SOC. Therefore, the choice $\Delta_{\text{cf}} = \Delta_{\text{cf}}^0$ seems to be reasonable. For a more detailed comparison of theoretical and experimental values, the reader is referred to Carvalho et al. [109].

		AM05	LDA	PBE-GGA	Expt.
<i>zb</i> -AlN	$\Delta_{\text{so}}(\Gamma)$	21.8	21.9	21.8	19[121]
	$\Delta_{\text{so}}(L)$	16.9	17.0	16.8	
<i>zb</i> -GaN	$\Delta_{\text{so}}(\Gamma)$	20.2	19.4	21.6	17[121]
	$\Delta_{\text{so}}(L)$	31.3	31.2	31.6	
<i>zb</i> -InN	$\Delta_{\text{so}}(\Gamma)$	17.4	14.4	20.7	5[121]
	$\Delta_{\text{so}}(L)$	53.7	53.0	54.3	
<i>wz</i> -AlN	Δ_{cf}^0	-257.2	-242.7	-217.2	-169[123]
		(-275.7)	(-260.0)	(-234.3)	
	ΔE_1	-250.4	-235.9	-210.5	
		(-268.9)	(-253.2)	(-227.6)	
	ΔE_2	14.9 (14.9)	14.9 (14.9)	14.9 (14.9)	
	$\Delta_{\text{cf}}^{\text{qc}}$	-257.3	-242.7	-217.3	-230[123]
		(-275.8)	(-260.1)	(-234.4)	
	$\Delta_{\text{so}}^{\text{qc}}$	21.8 (21.8)	21.7 (21.8)	21.7 (21.7)	19[123]
	$\Delta_{\text{so}\parallel}$	21.7 (21.7)	21.7 (21.7)	21.6 (21.6)	
$\Delta_{\text{so}\perp}$	22.7 (23.5)	22.1 (22.8)	22.5 (23.3)		
<i>wz</i> -GaN	Δ_{cf}^0	32.2 (26.4)	40.9 (34.5)	32.0 (27.3)	10[123]
	ΔE_1	8.4 (8.4)	8.7 (8.7)	9.0 (9.0)	
	ΔE_2	41.8 (36.0)	49.3 (42.9)	42.6 (37.9)	
	$\Delta_{\text{cf}}^{\text{qc}}$	35.3 (28.5)	43.1 (36.1)	35.3 (29.6)	39[123]
	$\Delta_{\text{so}}^{\text{qc}}$	14.9 (15.9)	14.9 (15.5)	16.3 (17.3)	17[123], 8[123]
	$\Delta_{\text{so}\parallel}$	18.0 (18.0)	17.1 (17.1)	19.6 (19.6)	
	$\Delta_{\text{so}\perp}$	22.0 (19.7)	21.5 (19.6)	23.2 (21.3)	
	$\Delta_{\text{so}\perp}$				
<i>wz</i> -InN	Δ_{cf}^0	34.6 (31.7)	41.3 (38.5)	25.1 (22.1)	40[123]
	ΔE_1	6.3 (6.3)	5.4 (5.4)	6.3 (6.3)	
	ΔE_2	42.8 (39.9)	47.4 (44.7)	36.5 (33.5)	
	$\Delta_{\text{cf}}^{\text{qc}}$	38.6 (35.6)	44.1 (41.3)	32.0 (28.8)	39[123]
	$\Delta_{\text{so}}^{\text{qc}}$	10.5 (10.6)	8.7 (8.8)	10.8 (11.0)	5[123]
	$\Delta_{\text{so}\parallel}$	14.5 (14.5)	11.5 (11.6)	17.7 (17.7)	
	$\Delta_{\text{so}\perp}$	22.4 (21.4)	20.1 (19.7)	24.7 (23.2)	
	$\Delta_{\text{so}\perp}$				

Table 3.5: Different energy splittings (from HSE calculations) of the uppermost VB states of the nitrides in three different equilibrium geometries are given in meV: The spin-orbit splitting constants at the BZ center Γ , $\Delta_{\text{so}} = \varepsilon(\Gamma_{8\nu}) - \varepsilon(\Gamma_{6\nu})$, and at the L point, $\Delta_{\text{so}}(L) = \varepsilon(L_{4,5}) - \varepsilon(L_6)$, for *zb* polymorphs as well as $\Delta E_1 = \varepsilon(\Gamma_{9\nu}) - \varepsilon(\Gamma_{7+\nu})$ and $\Delta E_2 = \varepsilon(\Gamma_{9\nu}) - \varepsilon(\Gamma_{7-\nu})$ for *wz* polymorphs are calculated from the HSE eigenvalues including SOC. The crystal-field splittings $\Delta_{\text{cf}}^0 = \varepsilon(\Gamma_5) - \varepsilon(\Gamma_1)$ (in the absence of SOC) are also given. The values $\Delta_{\text{cf}}^{\text{qc}}$ are derived within the quasicubic approximation. The spin-orbit interaction constants $\Delta_{\text{so}\parallel}$ as well as $\Delta_{\text{so}\perp}$ are derived using Δ_{cf}^0 for the crystal-field splitting (see text). The respective HSE+ G_0W_0 results are provided in parenthesis.

Recently, by means of quasiparticle self-consistent GW calculations, Punya and Lambrecht [172] computed a negative Δ_{so} for InN. They attributed this negative spin-orbit interaction to the symmetry inversion of the Γ_{7+} and Γ_9 valence band states owing the contribution of the In-4*d* orbital to the effective spin-orbit splitting.

3.2.5 Band dispersions

In Fig. 3.5 the large impact of the spin-orbit and crystal-field splittings on the dispersion of the uppermost valence bands around Γ is shown for the $\Gamma - X$ and the $\Gamma - L$ directions in the fcc BZ as well as the $\Gamma - A$ and the $\Gamma - M$ directions in the hexagonal BZ. Fig. 3.5(a) illustrates the splittings of the six uppermost VBs of the *zb* polymorphs: while the degeneracy of the heavy-hole (hh) bands, which belong to the Λ_4 and Λ_5 irreducible representations [173], is lifted along the $\Gamma - L$ direction, the light hole (lh) and the spin-orbit split-off (so) bands remain twofold degenerate.

The degeneracy of the L_4 and L_5 representations occurs due to the time-reversal symmetry. These effects are well known for other *zb* crystals [170, 174, 175] as well as for the nitrides. [105] The splitting of the hh bands near Γ along the [111] direction can be described by the relation [170] $\Delta E_{\text{hh}} = -2\sqrt{2}C_k \cdot k$. Using our *ab-initio* results we derive values of $C_k = -0.005, -0.063$ and -0.178 eVÅ for AlN, GaN and InN which are in qualitative agreement with the trends found for group-V compounds containing Al, Ga, and In. [170] The strong increase

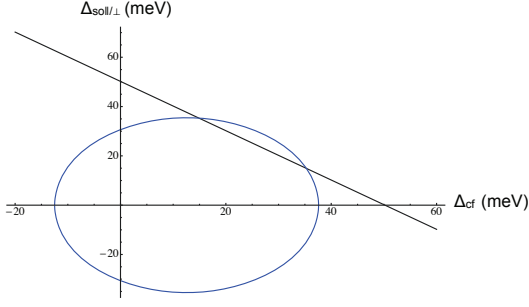


Figure 3.4: Geometric solution of Eq. (3.1) to relate the $\Delta E_{1/2}$ values (cf. Table 3.5) and Δ_{cf} , $\Delta_{so||}$, and $\Delta_{so\perp}$ for wz -GaN. The black line represents $\Delta_{so||}$ while the blue ellipsoid gives $\Delta_{so\perp}$. The two crossings indicate the two possible solutions within the quasicubic approximation.

of the C_k going from AlN to GaN or InN can be traced back to the presence of the shallow d states that contribute to the top of the VBs in GaN and InN. [105, 176]

Figure 3.5(b) illustrates the SOC-induced splitting effects for the VBs of the wz nitrides along the $\Gamma - M$ direction in the BZ. In this case all the irreducible representations compatible with spin are singly degenerate (except for the BZ center and the BZ boundary). In contrast to that, no spin splitting of the three VBs appears along the hexagonal $\Gamma - A$ direction since the small point group of these \mathbf{k} points is C_{6v} . Hence, the irreducible representations that are compatible with spin are twofold degenerate like Γ_9 , Γ_{7+} and Γ_{7-} in the BZ center. [177] Indeed, for GaN and InN a clear splitting of the lh bands is visible in Fig. 3.5(b), whereas the splittings for the other bands are small.

However, as can be seen for wz -GaN and wz -InN in Fig. 3.5(b), the interpretation of the VBs can be more complex due to state mixing and band crossings near the Γ point. For these materials the definition of spin splittings that are linear in the \mathbf{k} vector is impossible. For that reason the spin-orbit splittings of the hh, lh, and ch bands along the $\Gamma - M$ direction are compared to the corresponding splitting of the lowest CB in Fig. 3.6. This shows that the influence of the SOC on the hh band and the lowest CB remains relatively small. Contrary, the impact on the lh and the ch bands is much larger. As observed for the zb polymorphs, there is a clear chemical trend of increasing SOC splittings along the row AlN, GaN, and InN. For InN the \mathbf{k} -vector-induced splittings even approach the order of magnitude of Δ_{so} (cf. Table 3.5). The non-monotonous behavior of the wave-vector-induced splittings of the lh and ch bands of wz -GaN and wz -InN is a consequence of the corresponding band crossings along $\Gamma - M$ in Fig. 3.5(b).

3.2.6 Effective masses

The band dispersions and curvatures away from Γ in Fig. 3.5 depend not only on the splittings of the valence states but also on the coupling between the lowest CB and the uppermost VBs. Within $\mathbf{k} \cdot \mathbf{p}$ theory [132, 171] this coupling is governed by the interaction of the s -like CB state $|s\rangle$ and the p -like valence wave functions $|x\rangle$, $|y\rangle$, $|z\rangle$ at Γ , mediated by the momentum operator \mathbf{p} . The respective matrix elements $P_{\perp} = \frac{\hbar}{m_0} \langle s | \mathbf{p}_x | x \rangle = \frac{\hbar}{m_0} \langle s | \mathbf{p}_y | y \rangle$ or $P_{\parallel} = \frac{\hbar}{m_0} \langle s | \mathbf{p}_z | z \rangle$ give rise to relatively large values. In units of energy, the Kane parameters $E_{p\perp/\parallel} = \frac{2m_0}{\hbar^2} P_{\perp/\parallel}^2$ calculated using the HSE wave functions are $E_p = 15.86 / 13.26 / 9.50$ eV for

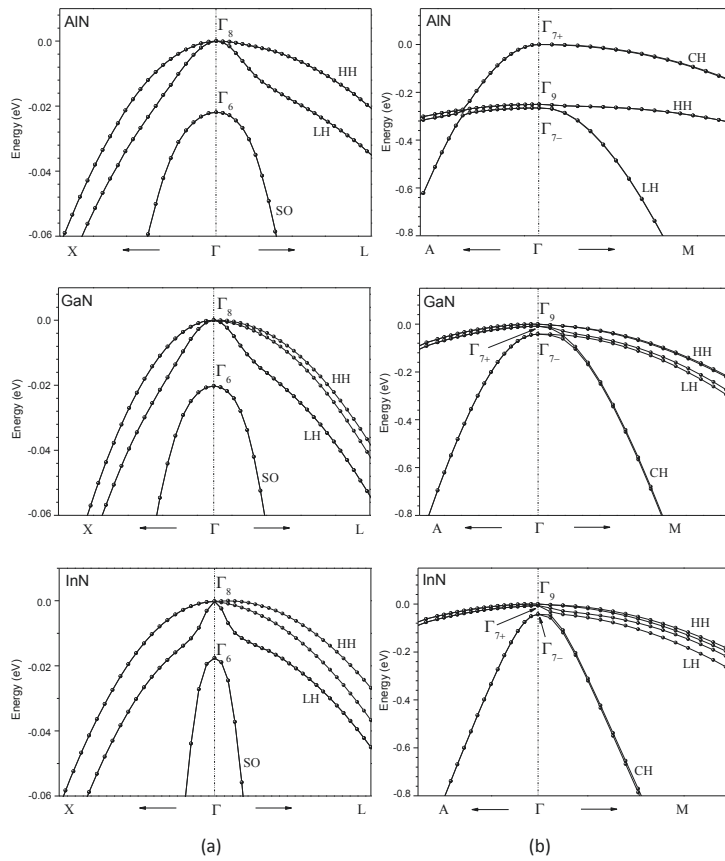


Figure 3.5: The HSE+SOC results for the uppermost VBs of AlN, GaN, and InN in (a) the zb and (b) the wz structure are shown along two high-symmetry directions in the BZ. Up to $1/16$ of the paths $\Gamma-X$, $\Gamma-L$, and $\Gamma-M$ in the BZ is shown, as well as $1/12$ of the $\Gamma-A$ path. The heavy-hole (hh), light-hole (lh), spin-orbit split-off (so), and crystal-field split-off (ch) bands are labeled and the top of the VBs is used as energy zero.

zb -AlN / zb -GaN / zb -InN or $E_{p\perp} = 15.78 / 12.83 / 9.39$ eV and $E_{p\parallel} = 15.92 / 14.79 / 10.52$ eV in the wz case. These values are close to those derived from experimental data for InN[178, 179] but seem to underestimate the values suggested for GaN.[181, 262] The agreement with theoretical values[118] calculated from the OEPx wave functions is good. However, the agreement is worse when comparing to results for GaN that take the GW corrections into account.[119]

The effective electron and hole masses are extracted from the HSE band-structure calculations (including spin-orbit interaction), assuming that the influence of the QP corrections on the band dispersion is small. Thereby, the complex curvature of the VBs shown in Fig. 3.5 renders the determination of the effective masses difficult. To avoid these complications, the lifting of degeneracies of the lh and the hh bands occurring away from the Γ point due to SOC are neglected by using averages over the \mathbf{k} -vector-induced spin-orbit-split band pairs.

In addition, it is essential to employ only the close proximity of Γ for the determination of the effective masses. The use of a larger \mathbf{k} -point region would give rise to larger effective masses of the lh band otherwise due to the significant non-parabolicity of the corresponding bands (cf. Fig. 3.5(a)). Moreover, the strong warping of the hh and the lh bands observed for the zb polymorphs is taken into account. In the wz case only wave vectors that are closer to the Γ point than the band-crossing points are taken into consideration. Figure 3.5(b) shows that especially the lh masses along the $\Gamma-M$ direction may sensitively depend on the wave-vector range chosen for their determination. This is not merely a shortcoming of the theoretical description but also holds for their experimental determination by varying the hole

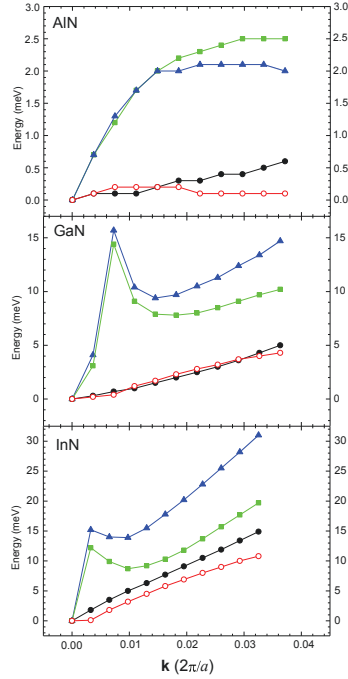


Figure 3.6: The spin-orbit-induced splittings for the wz nitrides in the proximity of Γ are shown along the $\Gamma-M$ direction. The hh (red open circles), the lh (blue triangles), and the ch (green squares) bands are given. For comparison the splittings for the lowest CB (black circles) are included.

concentrations. For the electron masses the situation is less complex as illustrated by the band structures in Fig. 3.1. The effective masses of the uppermost three VBs and the lowest CB are given for the zb polytypes in Table 3.6. While the HSE+SOC results describe the electron masses for zb -GaN quite well, they slightly overestimate them for zb -InN in comparison to measured values. Nevertheless, the numbers given in Table 3.6 confirm the extremely small electron mass for InN found in experiments. Overall, the results in the present work are closer to experimentally determined masses than found in previous calculations.[182, 183] The values of $m_{e\perp}(X) = 0.30 m_0$ and $m_{e\parallel}(X) = 0.53 m_0$ calculated for the CB minimum of zb -AlN in this work agree well with $m_{e\perp}(X) = 0.33 m_0$ and $m_{e\parallel}(X) = 0.52 m_0$ as derived within the LDA using the experimental lattice parameters.[107] The same holds for the effective masses of AlN and GaN at the CB minimum at the Γ point.[107] Especially for AlN and GaN the hole masses agree very well with the fully relativistic LDA calculations of Ramos *et al.*[184], as well as with other first-principles calculations based on local or semilocal XC functionals[107], empirical-pseudopotentials[182] or the OEPx+ G_0W_0 approach.[118] In general and also in our studies, no clear trend of the hole masses with the different XC functionals is found.

The electron masses at the Γ point decrease along the row AlN, GaN, and InN. Qualitatively they nearly agree with the values of 0.29, 0.20, and 0.04 obtained using the relation $m_e(\Gamma)/m_0 = 1/[1 + E_p/E_g]$. The hole masses of the spin-orbit split-off VBs in Table 3.6 are isotropic and also decrease from AlN over GaN to InN. The values in Table 3.6 show that the masses of the lh band are by a factor of $m_{hh}/m_{lh} = 3-27$ lighter than the hh ones. The masses of the lh bands approach values on the order of the electron effective mass. The fact that the hh and the lh masses (Table 3.6) are different in the three directions confirms the well-known warped isoenergy surfaces of the Kane model.[132]

	$m_{hh}^{[100]}$	$m_{lh}^{[100]}$	$m_{hh}^{[110]}$	$m_{lh}^{[110]}$	$m_{hh}^{[111]}$	$m_{lh}^{[111]}$	m_{so}	$m_e(\Gamma)$
<i>zb</i> -AlN								
This work	1.32	0.44	2.32	0.39	3.98	0.38	0.55	0.30
[184]	1.44	0.42	3.03	0.37	4.24	0.36	0.63	0.28
[182]	1.02	0.37	1.89	0.32	2.64	0.30	0.54	0.23
[182]	1.33	0.47	2.63	0.40	3.91	0.38		0.32
[107]								0.33
<i>zb</i> -GaN								
This work	0.83	0.28	1.59	0.25	1.95	0.23	0.34	0.19
[184]	0.86	0.21	1.65	0.19	2.09	0.19	0.30	0.14
[182]	0.84	0.22	1.52	0.20	2.07	0.19	0.35	0.14
[182]	0.81	0.27	1.38	0.23	1.81	0.22		0.19
[107]								0.19
Expt.[185]								0.15
<i>zb</i> -InN								
This work	0.91	0.079	1.55	0.065	1.89	0.070	0.11	0.052
[182]	0.84	0.080	1.37	0.078	1.74	0.077		0.054
[183]	1.26	0.100	2.22	0.097	2.74	0.096	0.19	0.066
Expt.[186]								0.041

Table 3.6: Effective heavy-hole (hh), light-hole (lh), spin-orbit split-off hole (so), and electron (e) masses (in units of the free-electron mass m_0) as derived from the HSE band structure (including SOC) of *zb*-AlN, *zb*-GaN and *zb*-InN. While hh and lh masses along the [100], [110], and [111] directions are given, only the isotropic mass for the so case is included. The values for the hh and lh masses represent averages along $\Gamma-L$ and $\Gamma-K$. For AlN, longitudinal and transverse electron masses are included also for the X point. The results are compared with values from other calculations and experiment.

The six different hh and lh masses given in Table 3.6 contain more information than is included in the Kane model of the three uppermost VBs. In the Kane model these bands are characterized by three Luttinger parameters γ_1 , γ_2 , and γ_3 . [107, 262] Using the HSE+SOC values, we determine the Luttinger parameters along the $\Gamma-X$ and the $\Gamma-L$ directions using the assumptions $\gamma_1 = \frac{m_0}{4}(1/m_{hh}^{[111]} + 1/m_{lh}^{[111]} + 1/m_{hh}^{[001]} + 1/m_{lh}^{[001]})$, $\gamma_2 = \frac{m_0}{4}(1/m_{lh}^{[001]} - 1/m_{hh}^{[001]})$, and $\gamma_3 = \frac{m_0}{4}(1/m_{lh}^{[111]} - 1/m_{hh}^{[111]})$. Using the masses given in Table 3.6 we obtain $\gamma_1 = 1.478 / 2.409 / 7.143$, $\gamma_2 = 0.379 / 0.592 / 2.890$, and $\gamma_3 = 0.595 / 0.959 / 3.439$ for AlN / GaN / InN. We find a dramatic increase of the Luttinger parameters from AlN via GaN to InN. The present results are close to the results of an OEPx+ G_0W_0 calculation (neglecting SOC). [118] However, for InN we obtain somewhat larger Luttinger parameters.

In the case of the *wz* polymorphs the band anisotropy is influenced by the lower crystal symmetry. The uppermost VBs are isotropic in the plane perpendicular to the c -axis due to the lift of the degeneracy at Γ . Therefore, the curvatures of the bands along the $\Gamma-M$ and the $\Gamma-K$ directions are nearly the same, whereas they differ from the dispersions along the $\Gamma-A$ direction.

As can be seen from the masses for the *wz* polytypes given in Table 3.7, the overall agreement (especially for the hh VB as well as the CB) with other calculations [106, 107, 118] for AlN and GaN (see Table 3.7) is much better than in the *zb* case. This also holds for the comparison with masses derived from measurements for *wz*-GaN [189, 190]. It has to be pointed out again that due to the non-parabolicity especially of the lh band its mass in the plane perpendicular to the c -axis is sensitive to the \mathbf{k} region chosen for its calculation. Consequently, if larger \mathbf{k} regions play a role in the measurement, an increase of the lh mass is expected (cf. Fig. 3.5(b)).

As shown for GaN and InN in Fig. 3.6 the averages of the lh and ch in-plane masses are influenced by the spin-orbit splitting of the corresponding VBs. For example the two lh masses are 0.44 and 0.24 m_0 for GaN or 0.15 and 0.06 m_0 for InN instead of 0.31 m_0 or 0.09 m_0 in Ta-

	m_{hh}^A	m_{lh}^A	m_{ch}^A	m_e^A	$m_{hh}^{M,K}$	$m_{lh}^{M,K}$	$m_{ch}^{M,K}$	$m_e^{M,K}$
<i>wz</i> -AlN								
This work	3.31	3.06	0.26	0.32	6.95	0.35	3.47	0.34
[182]	2.37	2.37	0.21	0.23	3.06	0.29	1.20	0.24
[106]	3.68	3.68	0.25	0.33	6.33	0.25	3.68	0.25
[107]	3.53	3.53	0.26	0.35	11.14	0.33	4.05	0.35
[187]				0.29				0.34
Expt.[118]				0.29-0.45				0.29-0.45
<i>wz</i> -GaN								
This work	2.00	1.22	0.20	0.21	0.57	0.31	0.92	0.21
[107]	2.00	1.19	0.17	0.35	0.34	0.35	1.27	0.35
[188]	1.76	1.76	0.14	0.19	1.69	0.14	1.76	0.17
[118]	1.88	0.92	0.19	0.19	0.33	0.36	1.27	0.21
Expt.	2.20[189]	1.10[190]	0.30[118]	0.20 [118]	0.42[118]	0.51[118]	0.68[118]	0.20[118]
<i>wz</i> -InN								
This work	1.98	1.02	0.08	0.06	0.44	0.09	0.18	0.06
[182]	2.44	2.44	0.14	0.14	2.66	0.15	3.42	0.14
[188]	1.56	1.56	0.10	0.11	1.68	0.11	1.39	0.10
[191]	1.39	1.39	0.10	0.12	1.41	0.12	1.69	0.11
Expt. [118]				0.07				0.07
[192]				0.055				0.055

Table 3.7: Effective heavy-hole (hh), light-hole (lh), crystal-field split-off hole (ch), and electron (e) masses (in units of the free-electron mass m_0) as derived from the HSE band structure including SOC of *wz*-AlN, *wz*-GaN and *wz*-InN. The masses are evaluated along the $\Gamma-A$, $\Gamma-M$, and $\Gamma-K$ direction in the BZ. The results are compared with values from other calculations and experiments.

ble 3.7. Furthermore, the in-plane hole masses calculated in this work for *wz*-InN are much smaller than previous predictions.[182, 188, 191] This is traced back to the more accurate band-structure calculations with respect to the gap value and the inclusion of SOC.

It is observed that the effective masses decrease along the row *wz*-AlN, *wz*-GaN, and *wz*-InN (cf. Table 3.7). For the electron masses this tendency can be explained again by the coupling of *s*- and *p*-states, $E_{p\perp/\parallel}$, and the gaps, E_g or $E_g + \Delta_{cr}$. Using the estimates $m_{e\parallel}(\Gamma)/m_0 = 1/[1 + E_{p\parallel}/E_g + \Delta_{cr}]$ and $m_{e\perp}(\Gamma)/m_0 = 1/[1 + E_{p\perp}/E_g]$ [132] one finds $m_{e\parallel}(\Gamma)/m_0 = 0.28, 0.20,$ and 0.06 and $m_{e\perp}(\Gamma)/m_0 = 0.29, 0.22,$ and 0.06 based on the computed energy values. Indeed, these estimated values are not too far from the results of the full calculations in Table 3.7 and, hence, explain the chemical trend and the symmetry-induced mass splitting.

4

InAlN and InGaN alloys: Energetics, structures, and cation distribution

*"Aceite seus limites sem jamais
desacreditar na sua capacidade de
superação"*

Caleidoscópia

The ternary, isostructural, wurtzite-derived group-III mononitride alloys $\text{In}_x\text{Ga}_{1-x}\text{N}$ and $\text{In}_x\text{Al}_{1-x}\text{N}$ are studied within a cluster expansion approach. Using density functional theory together with the AM05 exchange-correlation functional, the total energies and the optimized atomic geometries of all 22 clusters classes of the cluster expansion (cf. Appendix A.2) for each material system are calculated. The combination of various local configurations with an alloy statistics and the calculation of QP energies is a computational challenge which is however possible nowadays.[92]

So far, the limitation of most of the previous electronic-structure calculations for alloys is the use of just one atomic configuration to model an alloy with a given average composition x . Investigating only a certain fixed atomic geometry or an ordered structure cannot correctly describe the details of the cation distribution (clustering, ordering, composition fluctuation, etc.) in an alloy on a nm-scale. Hence, the corresponding results for alloy properties, such as the energy gap for a defined composition x , have a rather limited validity. Instead, the probability of the occurrence of such local structures has to be taken into account in a rigorous theoretical study; it is imperative to account for different configurations within a statistical scheme [90], i.e. a certain alloy statistics has to be used.

In this chapter, the alloy system is modeled by taking all possible combinations of In and Ga/Al atoms on the cation sublattice into account that arise when 16-atom cells with local *wz* geometry are assumed. For each of these clusters the equilibrium atomic geometry is calculated and, subsequently, the respective alloy properties are computed as configurational averages.

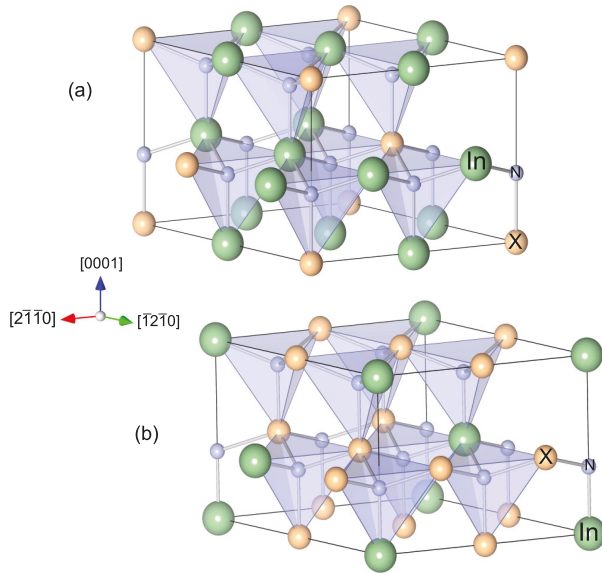


Figure 4.1: Ball-and-stick models for two cluster classes (a) $\text{In}_6\text{X}_2\text{N}_8$ ($j = 4$) and (b) $\text{In}_2\text{X}_6\text{N}_8$ ($j = 17$). The unit cell is indicated by black solid lines. The tetrahedra $\text{N-In}_i\text{X}_{4-i}$ (blue areas) that belong to the N atoms (small blue circles) in the unit cell are illustrated. The Cartesian axes **a**, **b**, and **c** correspond to the directions $[11\bar{2}0]$, $[\bar{1}2\bar{1}0]$, and $[0001]$, respectively. Large green (medium yellow) circles represent In (Ga,Al) cations.

4.1 Cluster approach and alloy statistics

The cluster expansion method combined with alloy statistics [87, 88] is one of the central approaches to describe isostructural ternary alloys. For cluster expansion and statistical methods, in this work, cf. section 2.3 as well as Appendices A.1 and A.2.

The clusters for the nitride alloys in wz structure are modeled by 16-atom supercells (i.e. $n = 8$) as depicted in Fig. 2.2. Due to the point-group symmetry of wz , the total number of $2^n = 256$ clusters is grouped into $J + 1 = 22$ classes.[84, 90] A complete treatment of all classes of larger clusters, e. g. of 32-atom clusters with $n = 16$ would increase the CPU time too much because of the $2^n = 65\,536$ clusters needed to study. The 16-atom cell can be constructed in such a way that N atoms occupy the top and bottom surfaces of the cell (cf. Fig. 2.2). Since the N sublattice (although somewhat deformed after atomic relaxation) is present in all cluster materials, the clusters with such surfaces may roughly be considered to be statistically independent, at least in c -axis direction.

All classes j represent more or less ordered systems along the three crystallographic directions $[11\bar{2}0]$, $[\bar{1}2\bar{1}0]$, and $[0001]$, giving rise to a - and c -planes in the unrelaxed starting geometries. Superlattices of ordered bilayers in $[0001]$ direction are of special interest; the most pronounced one is the class $j = 8$ with $\text{In}_4\text{X}_4\text{N}_8$ clusters (cf. Appendices A.1). The cluster material consists of In-N and X-N bilayers with the axis parallel to $[0001]$. In the class $j = 12$, with $n_j = 4$ each cation layer consists of alternating rows of In and X atoms in each c -plane in $[11\bar{2}0]$ direction (cf. Appendices A.1).

4.2 Structural and thermodynamic properties

While the tendencies for ordering and/or clustering in an alloy can intuitively be understood, it is, however, difficult to describe them quantitatively. It is also necessary to dis-

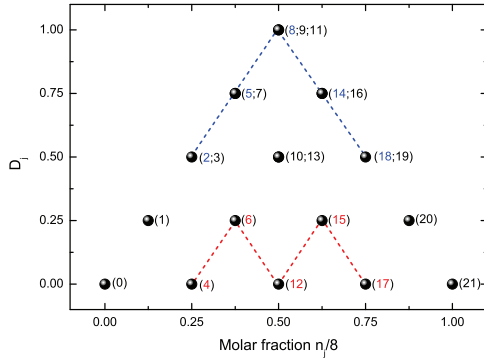


Figure 4.2: Degree of clustering D_j for all classes j (numbers given in parenthesis) of wz - $\text{In}_j\text{X}_{8-n_j}\text{N}_8$ versus the molar fraction $n_j/8$. The blue (red) dotted lines connect cluster classes j with lowest (highest) total energy per cation-anion pair.

tinguish between short-range and long-range ordering. By means of the Warren-Cowley parameter[193], the degree of short-range ordering in an alloy can be quantified and one can differentiate the atom distribution in a perfect random alloy from the clustered situation. The definition of this parameter can be easily applied to ternary systems based on zinc-blende crystals with 12 structurally equivalent second-nearest neighbor positions, as recently demonstrated for the ternary cubic nitrides.[194, 195] Since the geometry is different for wurtzitic systems with six second-nearest neighbors and two other cations in a slightly different distance, we introduce a novel approach to characterize ordering in non-cubic but tetrahedrally coordinated alloys.

First, for each of the eight N anions in a given cluster j , we count how many of the four *nearest neighbors* on the tetrahedral positions are In cations; this leads to five possible types of tetrahedra $\text{N-In}_i\text{X}_{4-i}$ with $i = \{0, 1, 2, 3, 4\}$ (see the two examples given in Fig. 4.1). By α_{ji} we denote the numbers of tetrahedra of type i that occur in the cluster class j for which it holds $\alpha_{ji} = \{0, 1, 2, 3, 4, 6, 8\}$. It can be verified that the α_{ji} fulfill the relations

$$\sum_{i=0}^4 \alpha_{ji} = 8 \quad (4.1)$$

and

$$\frac{1}{4} \sum_{i=0}^4 \alpha_{ji} \cdot i = n_j. \quad (4.2)$$

The first relation, Eq. (4.1), arises from the fact that there is a total of eight tetrahedra for each cluster cell. Equation (4.2) expresses that the total number of In atoms in cluster j equals n_j ; the prefactor of 1/4 ensures the correct counting of the In atoms. Note that the small perturbations of the ideal wz structure due to the relaxations of the atomic positions do *not* affect the assignment of the atoms to tetrahedra. Second, based on the α_{ji} as introduced above, we define a parameter D_j which describes the tendency of clustering on an atomic length scale for the cations of the class j . D_j is defined as the averaged mean-square deviation of the number of In atoms in a given tetrahedron, i , from the number of In atoms per tetrahedron, $n_j/2$, that corresponds to a uniform distribution of In over the cation positions in the

class j	n_j	g_j	D_j	ε_j (eV/pair)	c_j (Å)	a_j (Å)	V_j (Å ³ /pair)	$B_{0,j}$ (GPa)	$E_{g,j}$ (eV)	$E_{BP,j}$ (eV)
0	0	1	0.0	-12.503 -14.877	5.17 4.97	3.18 3.12	22.66 20.94	184.2 200.6	3.571 6.328	2.358 3.409
1	1	8	0.25	-12.258 -14.314	5.24 5.08	3.23 3.17	23.63 22.07	179.0 189.4	3.322 5.151	2.308 3.079
2	2	12	0.50	-12.019 -13.760	5.31 5.19	3.26 3.20	24.62 23.28	169.0 180.6	2.580 3.999	2.122 2.550
3	2	12	0.50	-12.033 -13.787	5.29 5.15	3.27 3.23	24.58 23.21	169.7 180.2	2.692 4.280	2.212 2.833
4	2	4	0.0	-12.052 -13.815	5.31 5.19	3.27 3.21	24.58 23.20	170.9 181.6	2.684 4.441	2.192 2.916
5	3	8	0.75	-11.783 -13.210	5.39 5.31	3.32 3.27	25.68 24.52	161.7 171.8	2.123 3.322	1.994 2.381
6	3	24	0.25	-11.831 -13.291	5.37 5.27	3.31 3.26	25.58 24.37	162.7 174.1	2.243 3.525	2.065 2.523
7	3	24	0.75	-11.812 -13.262	5.35 5.23	3.31 3.26	25.59 24.36	161.4 172.6	2.194 3.331	2.025 2.393
8	4	2	1.0	-11.550 -12.661	5.49 5.44	3.36 3.31	26.43 25.87	151.4 156.5	1.644 2.571	1.814 2.049
9	4	8	1.0	-11.592 -12.732	5.43 5.34	3.37 3.33	26.67 25.66	154.9 158.9	1.799 2.751	1.924 2.260
10	4	24	0.50	-11.612 -12.764	5.44 5.37	3.36 3.32	26.66 25.65	155.6 162.2	1.803 2.813	1.919 2.274
11	4	6	1.0	-11.609 -12.761	5.40 5.36	3.35 3.31	26.59 25.52	154.3 157.8	1.759 2.588	1.866 2.097
12	4	6	0.0	-11.647 -12.823	5.44 5.37	3.34 3.30	26.59 25.56	157.1 163.0	1.857 2.986	1.946 2.399
13	4	24	0.50	-11.627 -12.789	5.42 5.33	3.36 3.32	26.60 25.56	156.1 160.2	1.840 2.831	1.937 2.285
14	5	24	0.75	-11.411 -12.283	5.48 5.41	3.40 3.37	27.65 26.85	150.4 152.9	1.431 2.147	1.791 2.021
15	5	24	0.25	-11.422 -12.314	5.50 5.45	3.40 3.37	27.66 26.87	151.0 154.6	1.481 2.343	1.836 2.182
16	5	8	0.75	-11.392 -12.233	5.53 5.49	3.41 3.37	27.78 27.05	147.9 152.4	1.381 2.123	1.777 1.993
17	6	4	0.0	-11.269 -11.878	5.57 5.55	3.45 3.42	28.74 28.16	143.0 151.3	1.150 1.841	1.746 2.060
18	6	12	0.50	-11.249 -11.827	5.55 5.50	3.46 3.43	28.72 28.13	141.0 149.1	1.168 1.682	1.727 1.918
19	6	12	0.50	-11.234 -11.801	5.58 5.54	3.45 3.42	28.81 28.26	138.2 147.1	1.119 1.600	1.688 1.835
20	7	8	0.25	-11.075 -11.360	5.65 5.61	3.50 3.49	29.96 29.58	129.9 137.0	0.737 1.119	1.587 1.735
21	8	1	0.0	-10.916	5.73	3.55	31.18	126.8	0.638	1.580

Table 4.1: Properties of the 22 cluster classes for $\text{In}_{n_j}\text{Ga}_{8-n_j}\text{N}_8$ (first line for each j) and $\text{In}_{n_j}\text{Al}_{8-n_j}\text{N}_8$ (second line for each j). Each class j is characterized by the number n_j of In atoms and the degeneracy g_j of the class. The degree D_j of the isotropic clustering (see text), the total energy per cation-anion pair ε_j (in eV/pair), the effective lattice constants c_j and a_j (in Å), the volume per cation-anion pair V_j (in Å³/pair), and the bulk modulus $B_{0,j}$ (in GPa) are given for each j . In addition, the fundamental QP gap $E_{g,j}$ and the branch-point energy $E_{BP,j}$ with respect to the energy of the highest occupied state are listed.

supercell. Due to the normalization to the total number of tetrahedra, Eq. 4.1, the quantity

$$\begin{aligned}
 D_j &= \frac{\sum_{i=0}^4 \alpha_{ji} \left(i - \frac{1}{2}n_j\right)^2}{\sum_{i=0}^4 \alpha_{ji}} \\
 &= \frac{1}{8} \sum_{i=0}^4 \alpha_{ji} \left(i - \frac{1}{2}n_j\right)^2
 \end{aligned} \tag{4.3}$$

varies in the interval $0 \leq D_j \leq 1$.

Table 4.1 contains the D_j values for the 22 cluster classes. The value $D_j = 0$ occurs for the binary end components and indicates a tendency for no clustering and uniform distribution. However, it is also found for the cluster classes $j = 4, 12, 17$ which contain only N-In₁X₃, N-In₂X₂, and N-In₃X₁ tetrahedra, respectively, i.e. only tetrahedra with $n_j/2$ In atoms are

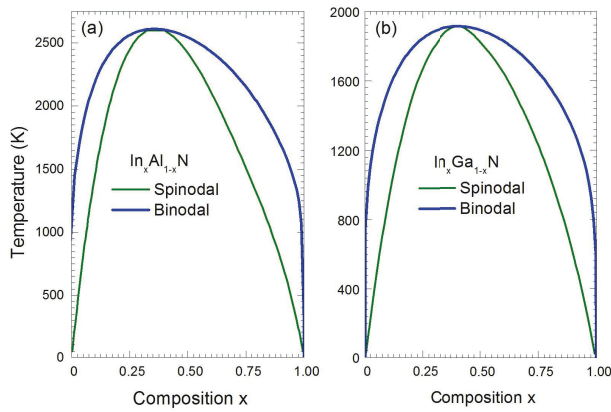


Figure 4.3: Spinodal and binodal phase diagrams for $\text{In}_x\text{Al}_{1-x}\text{N}$ (a) and $\text{In}_x\text{Ga}_{1-x}\text{N}$ (b) alloys in wurtzite structure computed from ΔF , Eq. 2.93 as a function of the temperature.

present in these cases. The maximum of $D_j = 1$ appears for the classes $j = 8, 9, 11$ with 4 In atoms. The classes $j = 8$ and 11 contain only tetrahedra of the type $\text{N-In}_1\text{X}_3$ and $\text{N-In}_3\text{X}_1$ and, hence, deviate from the uniform distribution of $n_j/2 = 2$. For $j = 9$, six $\text{N-In}_2\text{X}_2$ tetrahedra appear, which correspond to a uniform In distribution, however, the remaining two (N-In_4 and N-X_4) indicate strong clustering. Figure 4.2 clearly shows that the degree of clustering tends to maximum values for $n_j = 4$ and decreases towards $n_j = 0$ and $n_j = 8$. However, for a given n_j different D_j may occur (see Fig. 4.2).

The energetics of the clusters j with a given number of In atoms n_j seems to be clearly correlated to the tendency for clustering as described by D_j (cf. Eq. (4.3)). The energetically most favored class $j = 12$ is characterized by $D_j = 0$ (no tendency for clustering), while the less favored one $j = 8$ leads to $D_j = 1$ (large tendency for clustering). More specifically, the maximum values of the excess energies of 20.0 meV/pair ($\text{In}_4\text{Ga}_4\text{N}_8$) or 29.4 meV/pair ($\text{In}_4\text{Al}_4\text{N}_8$) occur for the cluster class $j = 8$. This relation between energetics and tendency for clustering is also found for the classes $j = 4$

($n_j = 2$) and $j = 17$ ($n_j = 6$). They are exclusively composed of $\text{N-In}_1\text{X}_3$ or $\text{N-In}_3\text{X}_1$ tetrahedra due to the alternating rows of X-X (or In-In) and X-In atom pairs in $[11\bar{2}0]$ direction in both m - and c -planes. At the same time, they are the energetically most favorable ones of all classes j for the given $n_j = 2$ or 6 and are characterized by $D_j = 0$ (cf. Table 4.1).

The total energies ε_j per cation-anion pair of the $\text{In}_{n_j}\text{Ga}_{8-n_j}\text{N}_8$ and $\text{In}_{n_j}\text{Al}_{8-n_j}\text{N}_8$ clusters in Table 4.1 show a monotonous decrease with the number n_j of the In cations. Figure 4.4 shows the excess energies (cf. Eq. (2.95)) and the mixing enthalpies (as the configurational averages of the excess energies). From this figure it becomes clear that the excess energies of InAlN are generally larger than those of InGaN with similar trends for the composition dependence for both alloys. In addition, as common for isovalent and isostructural alloys, all excess energies and, hence, also the mixing enthalpies, are positive. This indicates that such alloys can be thermodynamically miscible only at temperatures T high enough for the entropy term $-T\Delta S$ (with ΔS being the mixing entropy) to be sufficiently negative. [85, 196, 197]

Within the GQCA (cf. section 2.3.2) in Fig. 4.3 we computed critical temperatures for the

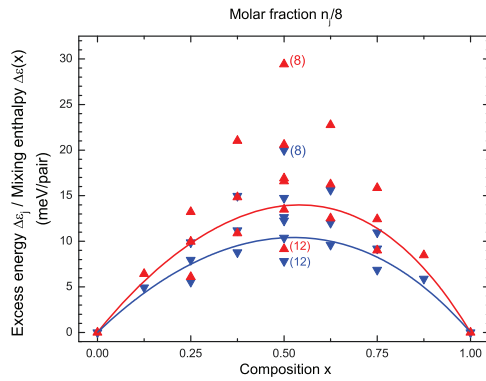


Figure 4.4: Excess energies $\Delta\varepsilon_j$ (triangles) and mixing enthalpies $\Delta\varepsilon(x)$ obtained using the SRS statistics (solid lines) versus fraction $n_j/8$ or composition x for InGaN (blue) and InAlN (red). The classes $j = 8$ ($j = 12$) are indicated.

miscibility of $T_c = 1914$ K at $x_c = 0.40$ for $\text{In}_x\text{Ga}_{1-x}\text{N}$ and $T_c = 2610$ K at $x_c = 0.36$ for $\text{In}_x\text{Al}_{1-x}\text{N}$. They are in good agreement with other more recent theoretical studies [90, 198]. The different covalent radii can lead to different strains in the layers causing deviations from the homogeneity of the sublattice. According to Zunger and Mahajan[87], this can also give rise to variations in the structural properties affecting the phase separation and/or the atomic ordering.

4.3 Bowing parameters

$$P(x) = xP(\text{InN}) + (1-x)P(\text{XN}) - x(1-x)P_b(x). \quad (4.4)$$

The most simple case, $P_b(x) \equiv 0$, is represented by the MDM in this work for which the variation with the composition is linear. If P corresponds to lattice constants, this situation is known as Vegard's rule [199].

For $P_b(x) \neq 0$ the property $P(x)$ in Eq. (4.4) shows a bowing as it is found, for instance, for the fundamental energy gaps. The parameter P_b itself may also depend on the average composition x . In this work the form [200]

$$P_b(x) = P_{b,0}/(1 + P_{b,1}x^2) \quad (4.5)$$

for the composition dependence is assumed and values for $P_{b,0}$ as well as $P_{b,1}$ are derived. The dependence of an alloy property P on the average composition x can be related to the values of the property for the binary end components, $P(\text{InN})$ and $P(\text{XN})$, by introducing a bowing parameter $P_b(x)$ according to

4.4 Lattice parameters and bulk modulus

The optimization of the atomic coordinates in the $\text{In}_{n_j}\text{Ga}_{8-n_j}\text{N}_8$ and $\text{In}_{n_j}\text{Al}_{8-n_j}\text{N}_8$ cluster cells with an initial atomic geometry corresponding to four primitive wz unit cells (cf. Fig. 2.2) leads to the results compiled in Table 4.1. From these results we calculate values

of 12.9 % (11.0 %) and 14.2 % (10.3 %) for the mismatches of the a and c lattice parameters of binary InN and AlN (GaN). Our results are in good agreement with the experimental values [124, 201, 202] of 13.0 % (10.5 %) and 14.5 % (9.7 %), respectively, which shows that the internal local strain in the alloys due to the different In-N and Ga-N (Al-N) bond lengths is correctly described.

The configurational averages for the lattice parameters a and c , calculated using the SRS cluster statistics (cf. Eq. (2.100)) as well as the MDM (cf. Eq. (2.102)), are given in Fig. 4.5. As discussed above, the MDM results correspond to a linear interpolation between the binary end components (i.e., Vegard's rule [199] for a and c). The deviations of the SRS results from the straight MDM line are small. Consequently, Fig. 4.5 shows at first glance that Vegard's rule describes the situation fairly well. This has also been observed by other authors. [90, 203]

More in detail, Vegard's rule is better fulfilled for the a lattice constant than for c in $\text{In}_x\text{Ga}_{1-x}\text{N}$. The opposite is true for $\text{In}_x\text{Al}_{1-x}\text{N}$ where the c lattice constant varies nearly linearly with the composition x . These findings suggest to use $a(x)$ for $\text{In}_x\text{Ga}_{1-x}\text{N}$ but $c(x)$ for $\text{In}_x\text{Al}_{1-x}\text{N}$ when determining the average composition x via Vegard's rule. Locally much stronger deviations from the linear interpolation as derived from Vegard's rule may occur; this is suggested by the lattice parameters of the individual cluster materials in Fig. 4.5.

In addition as can be seen from Fig. 4.5, the bowing for alloys described within the SRS model is small. Note that the composition dependence of the lattice constant c for $\text{In}_x\text{Al}_{1-x}\text{N}$ shows a concave instead of a convex behavior. Assuming a composition-*independent* bowing (cf. Eq. (4.4)), we find $a_b = 0.021$ (0.064) Å and $c_b = 0.067$ (0.048) Å for $\text{In}_x\text{Ga}_{1-x}\text{N}$ ($\text{In}_x\text{Al}_{1-x}\text{N}$). Taking the composition dependence of the bowing into account (cf. Eq. (4.5)) leads to values of $a_{b,0} = 0.022$ (0.063) Å, $a_{b,1} = 0.100$ (−0.073) and $c_{b,0} = 0.050$ (−0.117) Å, $c_{b,1} = -0.856$ (5.837) for $\text{In}_x\text{Ga}_{1-x}\text{N}$ ($\text{In}_x\text{Al}_{1-x}\text{N}$). Even though the bowing is small for the composition dependence of the lattice constants, it may influence the determination of the average composition x using measured lattice parameters along with Vegard's rule. A maximum deviation of 0.02 Å from the linear interpolation leads to a maximum uncertainty of the composition of about 0.5 %.

The classes $j = 11, 12$ for $\text{In}_4\text{Ga}_4\text{N}_8$ and $j = 8, 12$ for $\text{In}_4\text{Al}_4\text{N}_8$ exhibit the strongest deviation from the linear interpolation: $c(x = 0.5) = 5.44 / 5.37$ Å and $a(x = 0.5) = 3.36 / 3.32$ Å, as computed from Table 4.1. These classes are characterized by superlattice-like structures; the $j = 8$ material, for instance, consists of alternating c -plane bilayers in [0001] direction and in the case of the class $j = 11$ the superlattice is formed by m -plane bilayers in [1 $\bar{1}$ 00] direction. Interestingly, both classes show the same high degree of clustering, $D_8 = D_{11} = 1$, with four tetrahedra of type N- In_3X_1 and four of type N- In_1X_3 . It is noticeable that, in average, these classes show merely tetrahedra of type N- In_2X_2 as class $j = 12$ whose clustering degree is $D_{12} = 0$. It is likely that, tetrahedra N- In_2X_2 exhibit the strongest deviations from the ideal situation due to the high lattice mismatches between InN-AlN and InN-GaN.

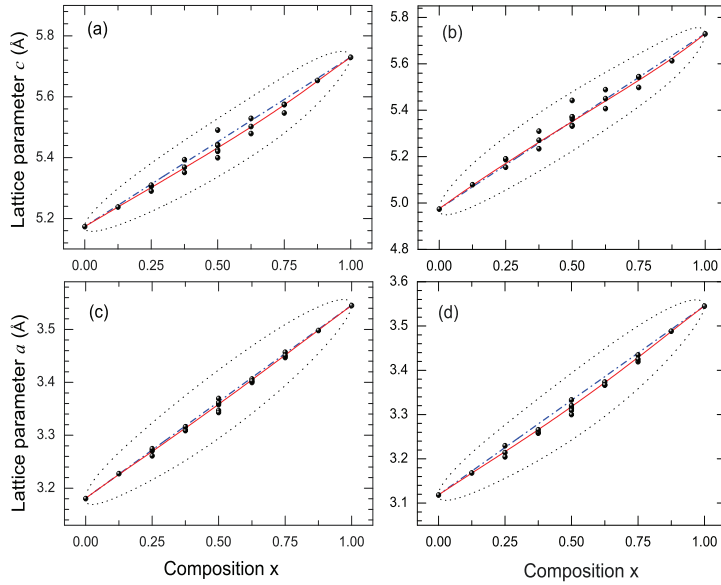


Figure 4.5: Lattice parameters c [(a) and (b)] and a [(c) and (d)] of $\text{In}_x\text{Ga}_{1-x}\text{N}$ [(a) and (c)] and $\text{In}_x\text{Al}_{1-x}\text{N}$ [(b) and (d)] alloys in wz geometry versus composition x for MDM (dot-dashed blue lines) and SRS statistics (red solid line). The black dotted lines indicate the mean-square deviation within SRS. The dots represent the results versus the fraction $n_j/8$ of the individual cluster materials.

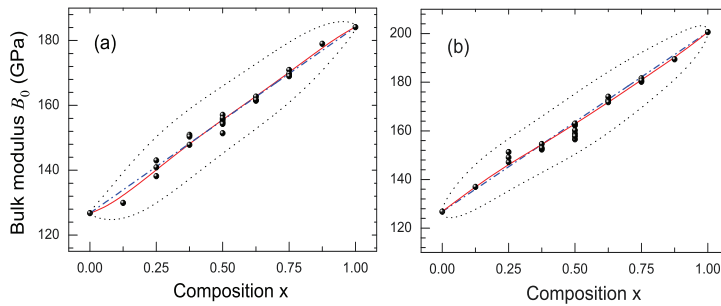


Figure 4.6: Bulk modulus B_0 of $\text{In}_x\text{Ga}_{1-x}\text{N}$ (a) and $\text{In}_x\text{Al}_{1-x}\text{N}$ (b) alloys in wz geometry versus composition x for MDM (dot-dashed blue lines) and SRS statistics (red solid line). The black dotted lines indicate the mean-square deviation within SRS. The dots represent the bulk moduli of individual cluster materials.

Figure 4.6 depicts the configurational averages for the bulk moduli of $\text{In}_x\text{Ga}_{1-x}\text{N}$ and $\text{In}_x\text{Al}_{1-x}\text{N}$ as obtained within the MDM and the SRS model. As for the lattice parameters, the SRS model leads to deviations of the elastic properties from the linear interpolation. The composition-*independent* bowing parameters amount to $B_b = 0.88 / 2.19$ GPa for $\text{In}_x\text{Ga}_{1-x}\text{N} / \text{In}_x\text{Al}_{1-x}\text{N}$. In addition, Fig. 4.6 shows that the strongest deviations of B_0 from the linear interpolation occur in the composition range $0 < x \leq 0.5$. They mainly follow the deviation of the lattice parameter a , as can be seen from a comparison with Fig. 4.5.

5

InAlN and InGaN alloys: Quasiparticle electronic structure

*"Três elementos são capazes de fazer
feliz uma pessoa: DEUS, um amigo e
um livro."*

Lacordaire

Recently it has been found experimentally that the incorporation of small amounts of In leads to an enhancement of the light emission intensity in light-emitting diodes as well as laser diodes with respect to devices made from pure GaN or AlN[204]. This may be related to In clustering as well as composition fluctuations[205]. However, also the short radiative lifetimes measured for alloys that contain In have been traced back to atomic condensates of In-N bonds[25]. This variety of results shows that a good grasp of the incorporation and distribution of In in the $\text{In}_x\text{Ga}_{1-x}\text{N}$ or $\text{In}_x\text{Al}_{1-x}\text{N}$ alloys is crucial for both the device operation as well as the physical understanding of the material.

Indeed, the local structural patterns of an alloy system determine its electronic properties [194, 203]. Since the (optical) gap of an alloy can be measured by photoluminescence or optical absorption experiments, the majority of theoretical studies focused on the band gaps and, in particular, their non-linear variation with the average composition x (see e.g. Refs. [89, 194, 203, 206–210]). However, most of these electronic-structure studies rely on the density functional theory [211, 212] together with the local density approximation or the generalized-gradient approximation to describe exchange and correlation. In these approximations the fundamental energy gap of a semiconductor is significantly underestimated [203, 206–208] due to the missing quasiparticle effects [26]. Understanding the electronic structure and the optical properties of the alloys requires a more sophisticated approach,[92] for instance, most modern QP calculations.

In this chapter, we pursue an approach which relies on the picture of Fermi-level pinning; in this case the natural level of reference for the QP energies for different cation arrangements and In/Ga or In/Al ratios is the branch-point energy [103, 145, 158, 213–215]. At the BPE the electronic states change their character from predominantly acceptor-like (usu-

ally valence states) to donor-like (usually conduction states). Therefore, it is assumed that the global Fermi level of the electrons is pinned near at the BPE. Here, the BPEs are computed for each cluster material using a modified Tersoff approach [103] taking the lowest eight conduction bands and the highest sixteen valence bands into account. The computed BPEs (cf. Table 4.1) indicate that the branch point is located in the conduction bands for In-rich clusters up to about $n_j = 5$ ($n_j = 4$) for $\text{In}_{n_j}\text{Ga}_{8-n_j}\text{N}_8$ ($\text{In}_{n_j}\text{Al}_{8-n_j}\text{N}_8$).

5.1 Energy zero and alignment

For each of the 22 cluster classes of the $\text{In}_x\text{Ga}_{1-x}\text{N}$ and $\text{In}_x\text{Al}_{1-x}\text{N}$ alloys, the QP band structure is calculated using the HSE06+ G_0W_0 method. However, the definition of an average band structure for a given composition x and its calculation by means of the Connolly-Williams formula,[91] Eq. (2.91), is difficult [216] because the energy zeros of the cluster classes are different and the size of the BZ varies from class to class. However, for energies at the Γ point such an average is possible since the symmetries of the corresponding energy states can be related to each other. This holds e. g. for the energies of the lowest conduction-band state E_{c_j} and highest valence-band state E_{v_j} .

The configurational average Eq. (2.91) is however possible for the density of states (DOS) after alignment of the individual energy scales. When comparing single-QP energies of different cluster materials j one has to consider a common absolute energy scale, i.e. an internal reference level to which the individual QP energy scales of the individual cluster classes can be aligned. The space-averaged electrostatic potential (or sometimes the total KS potential) can provide such a level of reference. Alternatively, deep (atomic) levels such as the semicore d states can be used for the alignment. Here we use the BPE as internal reference level.

5.2 Density of states

The calculated QP electronic structures lead to significantly different DOSs of the individual cluster materials. Some features of the individual clusters remain conserved in an alloy. The strongly dispersive conduction band found for the nitrides (see Fig. 3.1), in particular for InN, leads to a slowly increasing tail of the density of the conduction-band states. Since all clusters contribute within the SRS model, the configurational averages of these tails render a definition of the band edges $E_v(x)$ and $E_c(x)$ in the lowest conduction-band and highest valence-band, respectively, very difficult (see Fig. 5.1). The background is that an alloy with chemical and structural disorder is not anymore a translationally invariant system. So in general, the definition of a bandstructure is impossible.[216] Therefore, we added the lines corresponding to $E_v(x)$ and $E_c(x)$ to Fig. 5.1 to indicate where the Lorentzian-broadened DOS of the occupied and empty states becomes smaller than $0.01 \text{ (eV}\cdot\text{pair)}^{-1}$. These lines provide

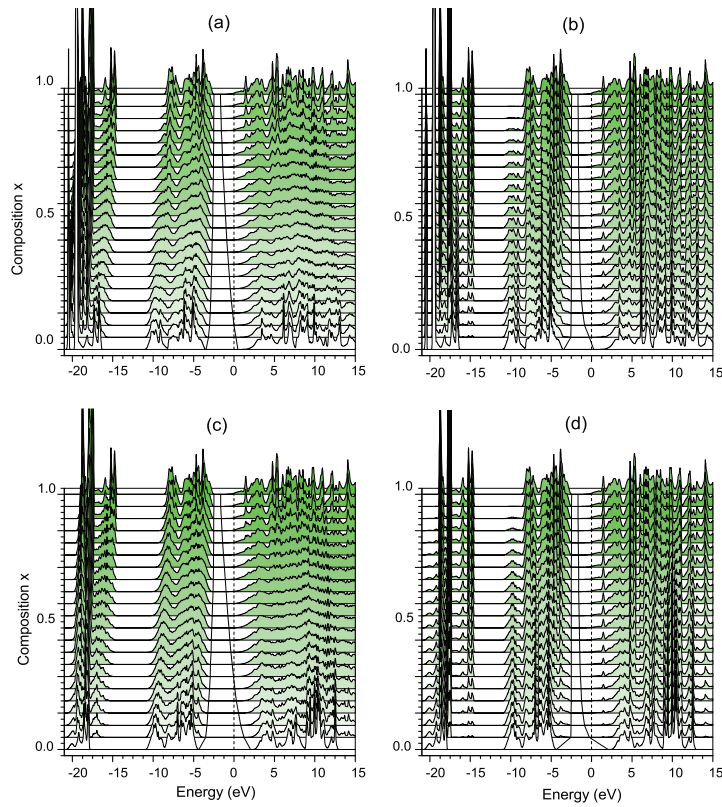


Figure 5.1: DOS in $(\text{eV}\cdot\text{pair})^{-1}$ (green areas) of the $\text{In}_x\text{Ga}_{1-x}\text{N}$ (a and b) and $\text{In}_x\text{Al}_{1-x}\text{N}$ (c and d) alloys versus energy (in eV), as a function of the composition x . The BPE has been used as energy zero (black dashed line). The curves are calculated as configurational averages using the cluster fractions from the SRS model (a and c) or the MDM (b and d). The DOS of the binary end components is shown for the compositions $x = 0.0$ and $x = 1.0$. The Lorentzian broadening parameter amount to 0.1 eV. In addition, as guide to the eye (see text), the black solid lines indicate where the DOS in the gap region decreases to $0.01 (\text{eV}\cdot\text{pair})^{-1}$.

insight into the composition dependence of the conduction-band and valence-band edges in the mixed crystals. Interestingly, they indicate for $E_c(x)$ at intermediate compositions x , that clusters with a fundamental gap $E_{g,j}$ (cf. Table 4.1) close to the one of InN significantly contribute to the alloy. The DOS differences between the GaN - (a,b) and AlN - (c,d) containing alloys are not only visible in the gap regions but also for low energies due to the occurrence of Ga 3d states.

Figure 5.1 also depicts the influence of the cluster statistics on the composition dependence of $E_c(x)$ and $E_v(x)$: While the MDM leads to a linear transition between the binary end components, the SRS statistics yields a significant non-linearity. In the case of the SRS model the DOS of all the cluster materials contribute to the peaks which is visible especially in the conduction-band region, where the DOS for intermediate compositions x significantly differs from the one of the binary end components. In the case of the MDM the linear transition between the DOSs of the binary end components is visible and mainly affects the heights of the peaks. The lower part of the uppermost p -like valence band region also differs significantly between the two statistics for both alloys. This striking difference in the composition dependence should be useful for the characterization of the cluster statistics and distribution by means of spectroscopic methods such as the investigation of the occupied DOS by means of X-ray photoemission (see e.g. Ref. [217]).

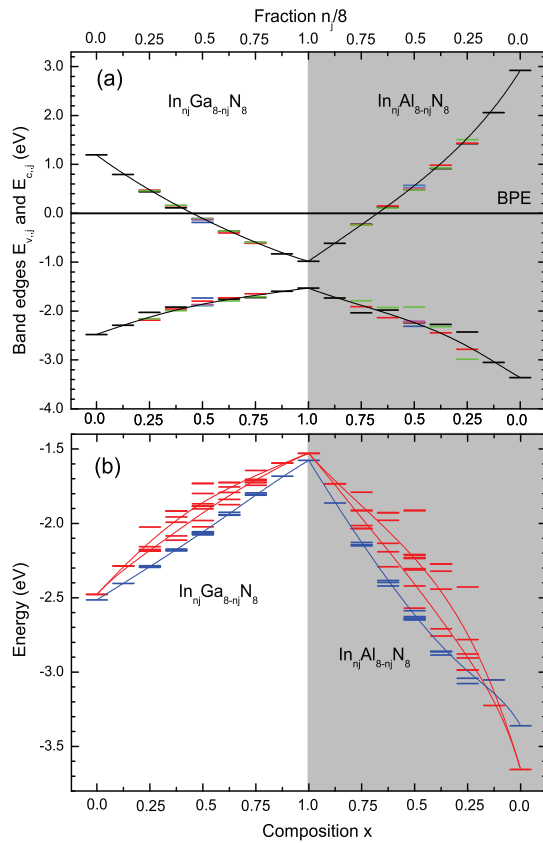


Figure 5.2: QP energy levels around the fundamental band gap for each cluster class j . In (a) the lowest conduction-band ($E_{c,j}$) and the highest valence-band ($E_{v,j}$) states are plotted. In (b) the two uppermost valence levels at the Γ point are shown as calculated for each cluster j in the HSE06+ G_0W_0 approximation. For the binary end components in wz structure these states are of Γ_5 (red) or Γ_1 (blue) type. The twofold degeneracy of the Γ_5 levels is lifted due to the deviations from the C_{6v}^4 symmetry at intermediate compositions. The configurational averages resulting within the SRS statistics are shown as guide to the eyes. The BPE has been used as energy zero.

5.3 Approximate band edges

In Fig. 5.2(a) the QP energies of the lowest conduction-band level, $E_{c,j}$, and of the highest valence-band level, $E_{v,j}$, are plotted for all cluster classes of the In_xGa_{1-x}N and In_xAl_{1-x}N alloys. In addition, the respective configurational averages, $E_c(x)$ and $E_v(x)$, as calculated within the SRS model, are shown. This figure indicates a non-linear variation of the band edges with the composition x of the alloys. It also shows that the gaps of the different cluster classes, that have the same number of In cations, vary significantly. More specifically, this variation can be on the same order of magnitude as the change that is observed when increasing or decreasing the number of In cations by one [see e.g. $x = 0.25$ or $x = 0.5$ in Fig. 5.2(a)].

In the light of the cluster ordering, for a given n_j we find that the energetically most unfavorable clusters with the highest tendency D_j for clustering give rise to the smallest energy distances $E_{g,j} = E_{c,j} - E_{v,j}$. This observation, which is in agreement with other theoretical studies,[203] becomes clear, for instance, for $j = 2$ or $j = 19$ in comparison to classes 3, 4 or 17, 18: In both cases the clusters are ordered ($D_j = 0.5$) with the same type of cations in c -planes with alternating bilayers. In addition, these cluster materials have the lowest conduction-band and highest valence-band states of all clusters for fixed $n_j = 2$ or $n_j = 6$, respectively. For $n_j = 4$ the situation is similar. The classes $j = 8, 9$, and 11 with $D_j = 1.0$ yield the smallest gaps.

The top of valence band states is studied in Fig. 5.2(b) in more detail. The three uppermost valence states are depicted versus the cluster fraction $n_j/8$ for each cluster class. Their average values using the SRS statistics versus the average composition x are also shown, despite the difficulties to identify the symmetry of the states due to the cation-site occupation and atomic relaxation. An additional problem appears in the $\text{In}_x\text{Al}_{1-x}\text{N}$ case. For the binary end components these states possess Γ_5 and Γ_1 symmetry (wz -InN and wz -GaN) or Γ_1 and Γ_5 symmetry (wz -AlN).[109] The reason for the different ordering of the valence-band symmetries is the sign of the crystal-field splitting: It is positive (35.6 meV for InN and 28.5 meV for GaN) for the two nitrides with d electrons, but negative (-275.8 meV) for AlN. As a consequence of this change of the band ordering, the valence levels in $\text{In}_x\text{Al}_{1-x}\text{N}$ cross at a certain fraction $n_j/8$ or composition x in order to guarantee the different signs of the crystal-field splitting as shown in Fig. 5.2(b). However, the situation is even more complicated, since for the cluster classes $0 < j < 21$ the symmetry of the atomic basis is significantly reduced. Therefore, the uppermost valence levels do not have the Γ_5 or Γ_1 symmetries. For these reasons it is difficult to describe the evolution of the Γ_5 and Γ_1 levels for varying compositions x and we pursue an approximation instead: In the case of $\text{In}_x\text{Ga}_{1-x}\text{N}$ we assume the same energetic ordering of the levels as found for GaN and InN. This procedure leads to the three lines plotted in the Fig. 5.2(b). Instead, in the case of $\text{In}_x\text{Al}_{1-x}\text{N}$ the ordering shown in Fig. 5.2(b) is only justified for $x \rightarrow 0$ and $x \rightarrow 1$. In addition, we have *assumed* the crossing of the Γ_5 and Γ_1 levels to occur between $x = 0.125$ and $x = 0.25$.

5.4 Fundamental gap and its bowing

In Fig. 5.3, the results for the fundamental band gaps $E_{g,j}$ (cf. Table 4.1) of all cluster materials are depicted together with the configurational averages $E_g(x)$ as a function of the composition x for both alloys. As discussed for the highest total energy (cf. Sec. 4.2), there is also a correlation of the fundamental band gap with the vertical ordering of the In and the Ga/Al atoms along the c -axis: The lowest gap appears for the highest degree of ordering $D_j = 1$ for $n_j = 4$. In the case of the ordered geometries, such as the $(\text{InN})_1(\text{XN})_1(0001)$ superlattices (see discussion above), the majority of In-N and X-N bonds are practically unstrained. These In-N bonds lead to a lowering of the gap in the cluster material towards the value of bulk InN.

As shown in Fig. 5.3, the gaps of the individual cluster materials clearly indicate a strongly nonlinear variation with the composition. Composition-*independent* bowing parameters (cf. Eq. (4.4)) obtained within the SRS statistics roughly amount to $E_{g,b} = 1.57$ eV ($\text{In}_x\text{Ga}_{1-x}\text{N}$) and $E_{g,b} = 3.03$ eV ($\text{In}_x\text{Al}_{1-x}\text{N}$). The physics underlying to the bowing parameter has been discussed in detail elsewhere.[218, 219] When a possible composition dependence of the bowing parameter is taken into account (cf. Eq. 4.5), we obtain $E_{g,b_0} = 1.42$ (2.24) eV and $E_{g,b_1} = -0.348$ (-0.875) for $\text{In}_x\text{Ga}_{1-x}\text{N}$ ($\text{In}_x\text{Al}_{1-x}\text{N}$). These numbers for the composition-

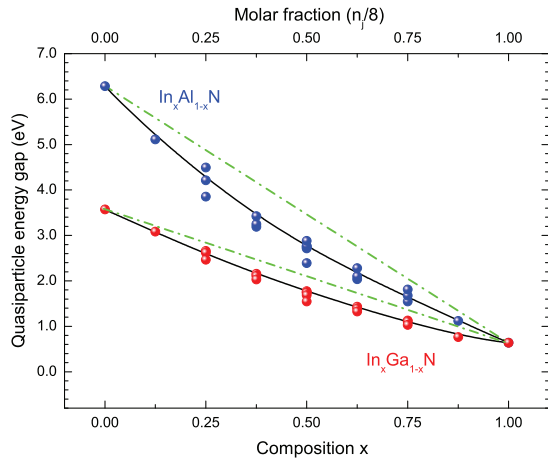


Figure 5.3: Quasiparticle energy gap of $\text{In}_x\text{Ga}_{1-x}\text{N}$ and $\text{In}_x\text{Al}_{1-x}\text{N}$ alloys in wz geometry versus composition x as computed using the MDM (dot-dashed green line) and the SRS model (black solid line). The dots represent the band gaps of the individual clusters.

dependent bowing parameters $E_{g,b}$ indicate a stronger bowing for InN-rich alloys in comparison to the XN-rich alloys.

Comparing the bowing parameters calculated in this work to results computed by other authors (see Refs. [89, 203, 207, 220] and references therein) shows the same order of magnitude. Vurgaftman *et al.*[18] recommend values of $E_{g,b} = 1.4$ eV ($\text{In}_x\text{Ga}_{1-x}\text{N}$) and $E_{g,b} = 2.5$ eV ($\text{In}_x\text{Al}_{1-x}\text{N}$) which are close to the ones predicted in this work. The calculated results slightly overestimate the experimental ones, which can be the consequence of the fact that the SRS model gives an upper limit for the bowing. The deviation of experimental parameters for $\text{In}_x\text{Al}_{1-x}\text{N}$ may also be traced back to the use of only AlN-rich samples.[200]

In addition, Fig. 5.3 shows that clustering can lead to a substantial increase of the bowing,[203] especially for $\text{In}_x\text{Al}_{1-x}\text{N}$: Several gap values $E_{g,j}$ appear below the configurational average obtained within the SRS model. Assuming that the cluster material which has the smallest gap for $n_j = 4$ ($E_{g,j} = 1.644$ eV for $\text{In}_4\text{Ga}_4\text{N}_8$ and $E_{g,j} = 2.571$ eV for $\text{In}_4\text{Al}_4\text{N}_8$) determines the alloy properties at $x = 0.5$, we obtain increased bowing parameters of 1.84 eV ($\text{In}_x\text{Ga}_{1-x}\text{N}$) and 3.65 eV ($\text{In}_x\text{Al}_{1-x}\text{N}$). However, these values are still smaller than those predicted by Gorczyca *et al.*[203] for the “clustering” scenario. In any case, the significant bowing of the gap found in experiment and in the calculations shows that a linear interpolation is not valid for both alloys.

In Fig. 5.4, the configurational averages for the band gaps are compared to optically measured results for $\text{In}_x\text{Ga}_{1-x}\text{N}$ and $\text{In}_x\text{Al}_{1-x}\text{N}$. For both alloys, most of the measured gap values appear within the area defined by the lines $E_g(x)$ and $E_g(x) - \Delta E_g(x)$, i.e. the configurational average reduced by the mean-square deviation. The few exceptions e.g. the absorption measurements of Wu *et al.*[178] or the values derived by Naoi *et al.*[221] for InN-rich $\text{In}_x\text{Ga}_{1-x}\text{N}$ alloys, however, approach (for $x \rightarrow 1$) a gap which is larger than the theoretical gap of $E_g = 0.64$ eV computed for InN within this work.

For a more detailed comparison, we divide the measured data into two groups: In Figs. 5.4(a) and (c) we compare to results derived from absorption measurements and in Figs. 5.4(b) and (d) energies obtained from photoluminescence are used. Therefore, we claim that extrapo-

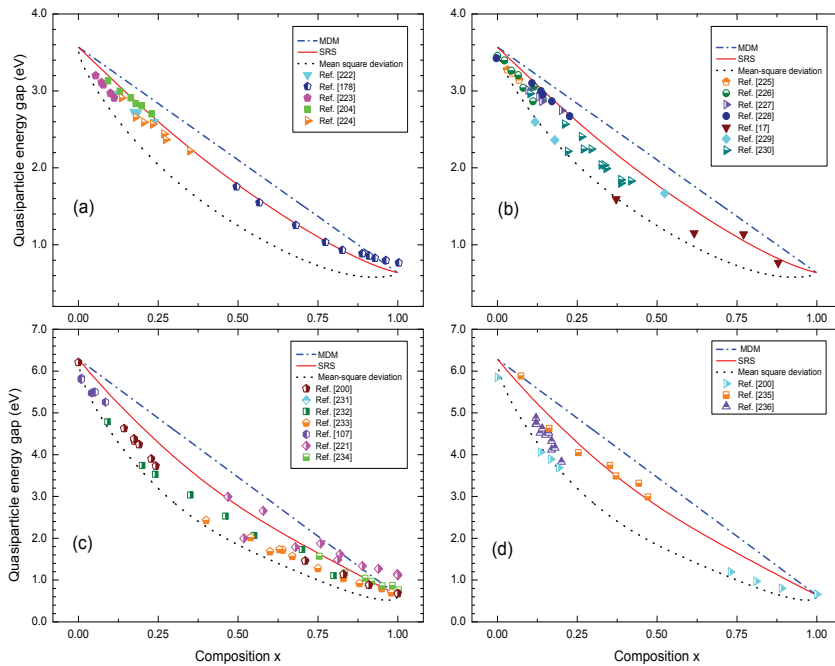


Figure 5.4: Quasiparticle energy gaps of $\text{In}_x\text{Ga}_{1-x}\text{N}$ (a, b) and $\text{In}_x\text{Al}_{1-x}\text{N}$ (c, d) alloys in wz geometry versus composition x computed using the MDM (dot-dashed blue line) and the SRS model (red solid line). The black dotted line describes the band gap reduced by the mean-square deviation, $E_g(x) - \Delta E_g(x)$. In the panels (a, c) we compare with absorption data (different symbols) while the experimental gaps (different symbols) in the panels (b, d) have been derived from luminescence measurements: (a) Refs. [178, 204, 222–224], (b) Refs. [17, 225–230], (c) Refs. [107, 200, 221, 231–234], and (d) Refs. [200, 235, 236].

lating the absorption edge in a random alloy to the limit of vanishing absorption defines an average gap of the system. The absorption onset can be affected by larger regions of the alloy, hence, it is better represented by the configurationally averaged band gaps. Contrary, in the case of the photoluminescence or cathode luminescence, the excited electron-hole pairs diffuse and relax until they reach domains with the smallest *local* gaps as long as the time constants for diffusion and relaxation are smaller than the lifetime of the excited electron-hole pairs. Consequently, the luminescence results should not be compared to $E_g(x)$, but to $E_g(x) - \Delta E_g(x)$ instead, i.e., to the configurational average reduced by the mean-square deviation.

The comparison of $E_g(x)$ to absorption data (cf. Fig. 5.4(a)) suggests that the SRS model seems to correctly describe the dependence of the measured absorption onsets on the average composition x for $\text{In}_x\text{Ga}_{1-x}\text{N}$. Especially the values of Nakamura *et al.*[204] are in good agreement. The results of McCluskey *et al.*[223] and O’Donnell *et al.*[224] indicate a deviation of $E_g(x)$ towards $E_g(x) - \Delta E_g(x)$ which may be a consequence of stronger composition fluctuations in the samples. This trend is found to be more pronounced for absorption studies of $\text{In}_x\text{Al}_{1-x}\text{N}$ (cf. Fig. 5.4(c)) which might be related to larger composition fluctuations due to the increased internal strain caused by the bigger bond-length difference between In-N and Al-N in comparison to Ga-N. Ordered structures play a less important role since their gap values are closer to the $E_g(x)$ curve than the measured values.

The physical picture derived from the luminescence measurements is less clear. For $\text{In}_x\text{Ga}_{1-x}\text{N}$ (cf. Fig. 5.4(b)) the experimental points are further away from the $E_g(x)$ curve than the ones in Fig. 5.4(a). However, only a few measurements, e.g. those of Davydov *et al.*[17] and Kim *et al.*[229], follow the $E_g(x) - \Delta E_g(x)$ line. Deviations found in other measurements may be a consequence of the actual alloy samples with local appearance of or-

dered structures and/or composition fluctuations. Measured values for $\text{In}_x\text{Al}_{1-x}\text{N}$ (cf. Fig. 5.4(d)) can be described by $E_g(x)$ (those of Onuma *et al.*[236]) as well as $E_g(x) - \Delta E_g(x)$ (those of Sakalauskas *et al.*[200]). The ones by Carlin *et al.*[235] are in between the two theoretical curves. The mean-square deviations computed within the SRS statistics seem to describe an upper limit for the difference in the absorption onset and the luminescence line. This difference is usually identified with the Stokes shift, but it is caused by the chemical (and partly structural) disorder in this work.[207]

Taking the mean-square deviation (cf. Eq. 2.92) for the fundamental band gaps into account can increase the bowing from 1.6 eV (see above) to 3.6 eV ($\text{In}_x\text{Ga}_{1-x}\text{N}$) or from 3.0 eV (see above) to 7.5 eV ($\text{In}_x\text{Al}_{1-x}\text{N}$) when going from $E_g(x)$ to $E_g(x) - \Delta E_g(x)$. These results indicate that the wide spread of bowing parameters found in the literature can be related to the different experimental methods and sample preparation techniques. Interestingly, our actual bowing-parameter values are almost embedded by values of 1.7... 2.8 eV / 2.5... 6.5 eV ($\text{In}_x\text{Ga}_{1-x}\text{N}$) or 2.1... 6.2 eV / 3.9... 14 eV ($\text{In}_x\text{Al}_{1-x}\text{N}$) computed by Gorczyca *et al.*[203] assuming a more uniform / a more clustered distribution of the In atoms.

6

InAlN and InGaN alloys: Excitonic effects and optical properties

"Acredite que você pode, assim você já está no meio do caminho."

Theodore Roosevelt

In the last decade enormous progress has been made in the *ab-initio* description of optical properties of bulk semiconductors [237, 238] and insulators [238, 239], but also of surfaces [240], nanostructures [241] and molecules [242]. This development is based on calculations which take the full quasiparticle (QP) electronic structure and the excitonic and local-field effects into account (see Refs. [81, 242] and references therein). The many-body effects drastically influence the lineshape, peak positions and peak intensities, especially of the optical absorption spectra. In the first step, going from the independent-particle approximation to the independent-QP approximation [102], the optically excited non-interacting electron-hole pairs are described by non-interacting quasidelectron-quasihole pairs. In general, the optical absorption spectra are significantly blue-shifted while the lineshape is less influenced [83]. The spectral picture based on critical points and van Hove singularities in the interband transitions between occupied QP valence bands and empty QP conduction bands [243] remains valid. In the second step the screened attractive and unscreened repulsive exchange interaction of quasidelectrons and quasiholes is taken into account. This usually leads to a drastic redistribution of oscillator or spectral strength from higher to lower photon energies combined with a certain redshift, which make the picture of van Hove singularities questionable [101]. In addition, the absorption edge may be significantly modified by the formation of bound excitonic states [64, 92, 244], a phenomenon which may also appear in resonance with higher optical transitions [101].

Such calculations have been also carried out for group-III nitrides crystallizing in wurtzite or zinc-blende structure [101, 133, 166, 244–248]. The resulting absorption coefficients and imaginary parts of the dielectric function are able to explain the experimental findings. The main peak structures, even in the range of higher interband transitions, are well described.

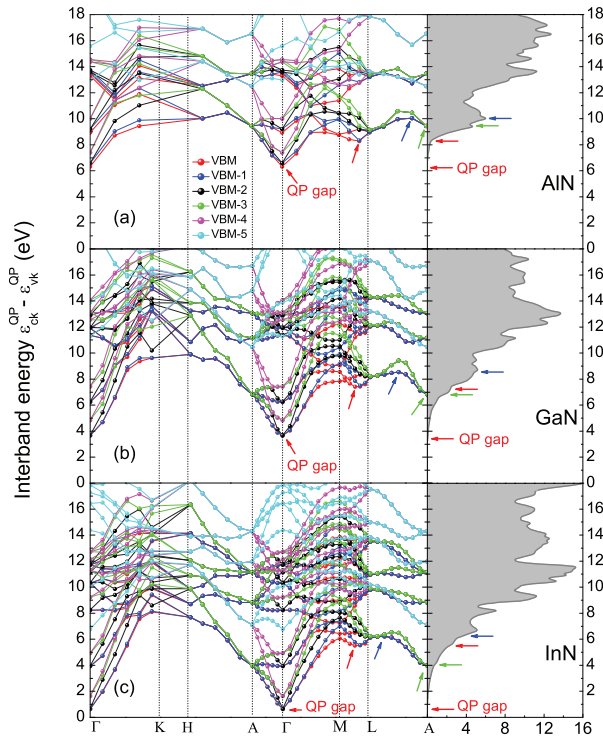


Figure 6.1: Joint QP band structure and joint density of states (in eV^{-1}) for wz -AlN (a), -GaN (b), and -InN (c) as obtained within a HSE + GW approach. The colors are related to the six highest valence bands and the arrows show lowest interband minima or maxima in the Joint QP band structure and its equivalent peak in the Joint density of states.

This holds not only for their positions but also for their intensities independent of the crystal structure. The latter result is especially remarkable since the dielectric functions of the nitrides [101, 133, 166, 244–248] are much smaller than those of other semiconductors, e.g. silicon [83], attributed to the fact that the interband transitions cover a wider spectral range up to about 18 eV. However, well-converged calculations of optical spectra including quasiparticle and excitonic effects together with optical transitions matrix elements based on all-electron(-like) wave functions also allow an accurate description of nonmetals with small oscillator strengths.

Meanwhile, there exist optical measurements, mainly due to spectroscopic ellipsometry, in a wide spectral range also for alloys of hexagonal group-III nitrides such as $\text{In}_x\text{Ga}_{1-x}\text{N}$ [249–251], $\text{In}_x\text{Al}_{1-x}\text{N}$ [200, 231], and $\text{Al}_x\text{Ga}_{1-x}\text{N}$ [252]. The variation of the lineshape with the composition x , but especially of the peak positions and intensities of absorption spectra, allow deep insight in the distribution of the group-III atoms over the cation sublattice, the strength of composition fluctuations, and the appearance of clustering phenomena (see Refs. [116, 203] and references therein). This is especially true when such measured spectra can be compared with theoretical ones including quasiparticle, excitonic, and LFEs [81, 83, 101] and a reasonable description of the alloying [84, 92, 116].

In this chapter, a combination of such calculations of electronic structures and optical spectra for alloys is used to study the frequency-dependent DF of wz - $\text{In}_x\text{Ga}_{1-x}\text{N}$ and - $\text{In}_x\text{Al}_{1-x}\text{N}$ for different light polarizations and cluster statistics. The success of the methods used is demonstrated for the end components InN, GaN, and AlN as well as for wz - $\text{In}_x\text{Ga}_{1-x}\text{N}$ and - $\text{In}_x\text{Al}_{1-x}\text{N}$ alloys. The influence of the alloy statistics and the composition

is studied by means of the absorption peaks, excitonic effects, and also dielectric properties of these materials.

6.1 Frequency-dependent dielectric function

In order to describe the optical properties of alloys in this work, their frequency-dependent macroscopic dielectric function (DF) $\varepsilon_{\perp,\parallel}(\omega)$ is studied as central quantity (cf. Sec. 2.2.5).

We performed such calculations including all the necessary interactions. For converged calculations too many electron-hole pairs $c\nu\mathbf{k}$ and optical transitions $|\nu\mathbf{k}\rangle \rightarrow |c\mathbf{k}\rangle$ have to be taken into the computation. However, the computational costs for the calculation of the starting HSE + GW electronic structure and the exciton Hamiltonian (cf. Eq. 2.87) become too high for all the 44 cluster calculations with 16-atom supercells, contrary to the restriction to one binary end component with two or four atoms in an unit cell, e.g. AlN [101].

In order to circumvent this problem, we follow the procedure of Schleife et al. [92]. The HSE + G_0W_0 QP eigenvalues and wave functions are mimicked by those of a LDA + U approach (cf. section 2.1.3.5) with an additional scissors shift Δ [64, 81, 92, 133].

6.2 LDA+ U + Δ as start approach

As described in section 2.4.9, the parameter U which describe an additional interaction on the Ga $3d$ or In $4d$ shell, is determined in such a way that the corresponding semicore binding energies approach the HSE + G_0W_0 values. The two U values, $U = 5.7$ eV (Ga $3d$) and $U = 3.7$ eV (In $4d$) are fixed in all clusters because of the strong localization of the d states. Here, the LDA + U scheme of Dudarev et al. [66] is used.

This procedure not only opens a gap from LDA values $< 0.0, 2.099, \text{ and } 4.385$ eV to LDA+ U values $0.386, 2.474, \text{ and } 4.385$ eV for wz -InN, -GaN, and -AlN. The resulting gaps values are still too small in comparison to the HSE+ G_0W_0 results. A scissors operator Δ , as described in section 2.4.9, is applied in order to achieve the QP gaps $0.638, 3.571$ and 6.328 eV mentioned before in Table 4.1. The resulting interband structures and JDOS computed in LDA+ U + Δ approach are very similar to those displayed in Fig. 6.1 computed from HSE06+ G_0W_0 calculations. In that case, it is illustrated the HSE+ G_0W_0 QP results obtained in [54] for AlN, GaN, and InN (c.f. Fig. 3.1). In Fig. 6.1 we show the joint band structure together with the joint density of states (JDOS) for interband transitions $\varepsilon_{c\mathbf{k}}^{\text{QP}} - \varepsilon_{\nu\mathbf{k}}^{\text{QP}}$ from the uppermost six VBs ($\nu = v$) into the CBs ($\nu = c$). The interband extrema related to van Hove singularities are clearly visible; besides the minima at Γ and A , such extrema also occur, for instance, between M and L . The lowest interband minima out of Γ give rise to an M_0 -type onset of the JDOS and the lowest interband maxima on the $L-A$ line are the reason for a pronounced peak-like structure in the JDOS. In [101] a more detailed discussion of critical points in AlN is presented.

According to the Appendix A.3, for each cluster class j such a scissors shift Δ_j used in the

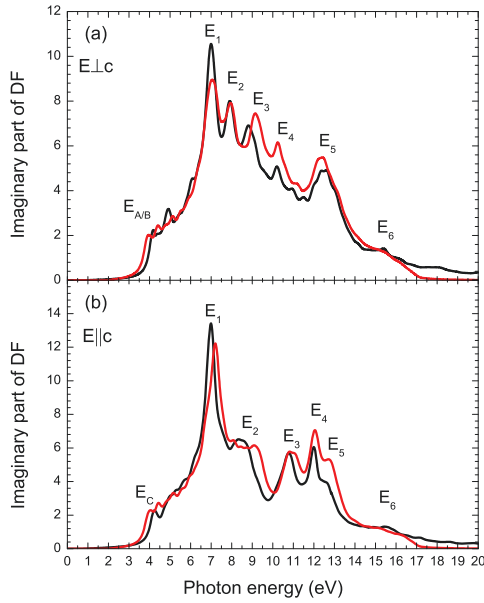


Figure 6.2: Imaginary part of (a) ordinary and (b) extraordinary dielectric function of wz -GaN calculated for 4-atom cells (red solid line) and 16-atom cells (black line).

LDA+ $U+\Delta$ approach has been computed. They vary non-linearly with n_j between 0.252 eV (InN) and 1.097 eV (GaN) or 1.943 eV (AlN).

6.3 Spectra of the binary-end components

The quality of the procedure described for the computation of the DFs of the individual cluster materials has to be checked by comparison with spectra computed for group-III nitrides in wurtzite geometry and experimental spectra.

Examples are illustrated in Figs. 6.2 and 6.3. In Fig. 6.2 we compare the result of our computational procedure for the DF of wz -GaN in a 16-atom cell with them of calculations using a 4-atom cell of the wurtzite geometry and hence more bands but a smaller BZ. In the case here the \mathbf{k} -point density near the lowest minimum of the joint band structure in Fig. 6.1 has been increased to a $9 \times 9 \times 9$ mesh for pair energies below 3.5 eV. The two spectra roughly agree. Only some peak positions and intensities are slightly modified. The same holds for higher photon-energy regions with only a small variation between the two DFs. The main reason for the discrepancies is the different sampling of the BZs and interband transitions. Together with the band folding the different BZs lead to a different sampling of the band pairs. Apart from slight changes in the JDOS also the interference of individual valence band - conduction band transitions weighted by the electron-hole pair amplitude $A_\Lambda(c\mathbf{v}\mathbf{k})$ in Eq. (2.90) is modified with sometimes significant consequences (see the discussion in Ref. [101])

In Fig. 6.3, the imaginary parts of the DF of wz -AlN, -GaN, and -InN, calculated for ordinary and extraordinary light polarization and using the 16-atom cells, are compared to spectra measured by spectroscopic ellipsometry [82, 253–257]. There is general agreement between theoretical and experimental spectra apart from small variations in the peak heights and positions. The biggest variations happen above the absorption onsets and in the region

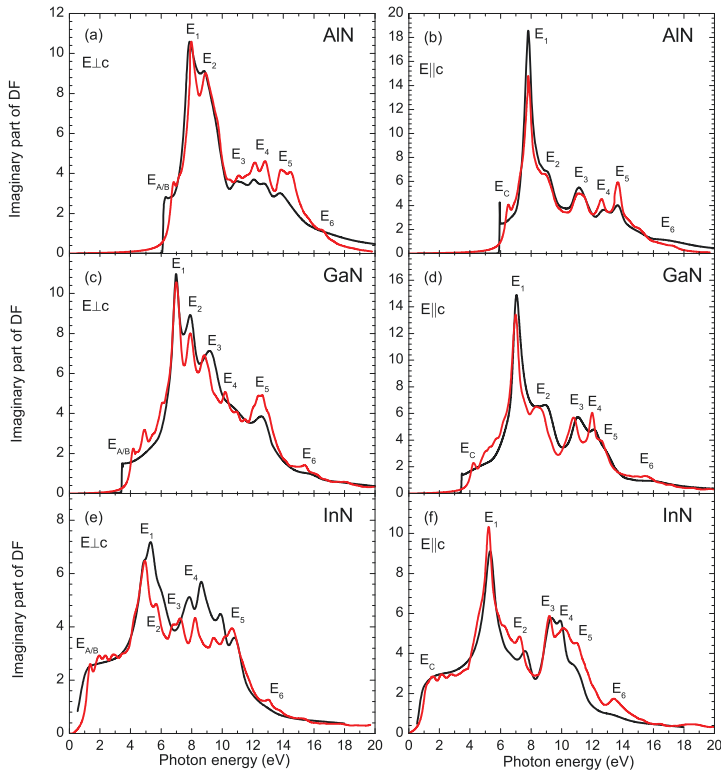


Figure 6.3: Imaginary part of the DF for ordinary (left panels) and extraordinary (right panels) light polarization of wz crystals of AlN (a,b), GaN (c,d), and InN (e,f). Red solid curves are calculated for the 16-atom supercells used in this work. The spectra are compared to experimental results (black solid lines) for InN [82, 253], GaN[254–256], and AlN[254, 255, 257].

of higher-energy interband transitions.

Nevertheless, Fig. 6.3 also indicates that the majority of measured peaks can be really identified within the theoretical investigations. This holds especially for the most pronounced absorption peak E_1 . The only exception for ordinary polarization and InN is related to the general underestimation (or overestimation in experiment) of the optical absorption in the 5-10 eV range of photon energies. In all other cases, the redistribution of spectral strength and the Coulomb enhancement due to the excitonic effects are obviously correctly described. The structures E_2, \dots, E_6 are mainly due a mixture of individual interband transitions near the BZ boundary of wurtzite as illustrated in Table 6.1. The theoretical spectra show wriggling structures just above the absorption onset. The reason is most easily explainable in the InN case where experimental spectra show an almost plateau-like region. The simulation of such a constant region in the imaginary part of the DF requires a further increase of the \mathbf{k} -point density in order to sum up over a sufficient number of broadened δ -functions. Small shifts of the peak positions E_2 and E_3 for GaN between theory and experiment may be interpreted as a consequence of the one and the same scissors shift for all interband transitions. In the case of InN the agreement is much better compared to previous computations [166]. Small changes to recent studies of AlN [101] mainly indicate the use of slightly modified atomic geometries. Figures 6.2 and 6.3, show different spectra in comparison to the joint DOS in Fig. 6.1 and, hence, indicate the importance of excitonic/LFEs on one hand and of optical dipole matrix elements on the other hand. The influence of the optical oscillator strength is obvious. Apart from the mixing of individual quasiparticle transitions in Eq. (2.90) they also lead

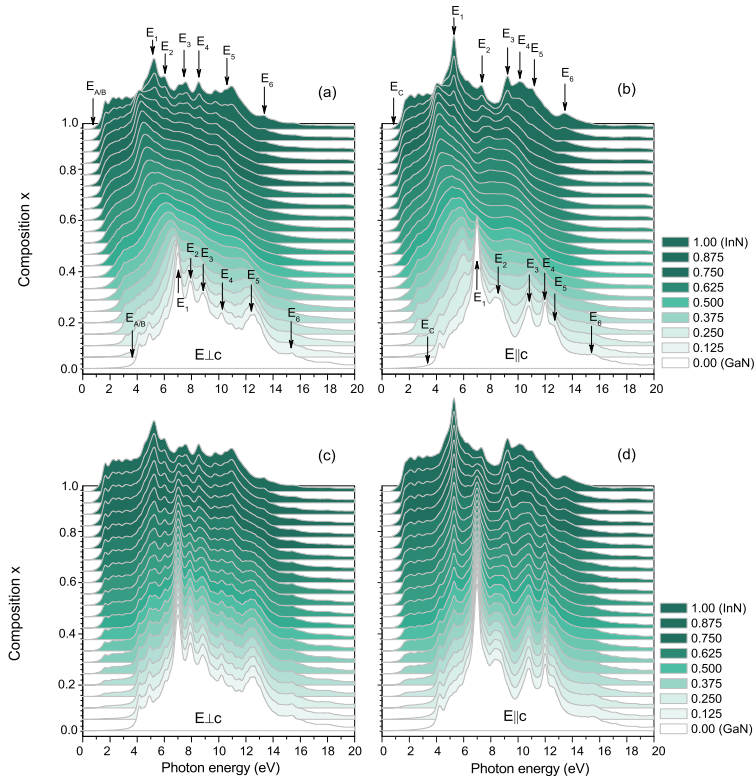


Figure 6.4: Imaginary part of the ordinary (a, c) and extraordinary (b, d) dielectric function $\varepsilon_{\perp/\parallel}(\omega)$ of wz - $\text{In}_x\text{Ga}_{1-x}\text{N}$ for varying averaged In compositions x . Results for two different alloy statistics, SRS (a, b) and MDM (c, d) model, are plotted.

to the decrease of the optical absorption for higher photon energies in order to guarantee the ω^{-2} tails of the imaginary parts [258].

6.4 Overall absorption spectra

For both light polarizations, i.e., ordinary and extraordinary, both alloy statistics SRS and MDM, and both alloys $\text{In}_x\text{Ga}_{1-x}\text{N}$ and $\text{In}_x\text{Al}_{1-x}\text{N}$ the configurationally averaged dielectric functions $\varepsilon_{\perp/\parallel}(\omega)$ have been computed according to Eq. (2.91) and expression (2.90). Their imaginary parts describing mainly the optical absorption are plotted in Figs. 6.4 and 6.5 for molar fractions $0 \leq x \leq 1$ over a wide range of photon energies. One observes a development of pronounced peak structures versus photon energy with the In composition x in the actual alloy. Thereby, the behavior of the lineshape development with x and the spectra resulting for a given x depend significantly on the alloy statistics.

The MDM spectra in Figs. 6.4(c), 6.4(d), 6.5(c), and 6.5(d) can be easily traced back to the spectra of the respective binary end components $x = 0$ and $x = 1$. The peak positions remain fixed at the values already found for the binary systems in Figs. 6.2 and 6.3. However, their intensities are clearly weighted by the probabilities $(1 - x)$ for GaN or AlN and x for InN. As a consequence, the absorption onsets exhibit a linear behavior in x . These findings clearly contradict the observations by means of room-temperature spectroscopic ellipsometry [200, 231, 250, 251, 255] that the variation of the optical gaps, the positions of absorption edge and the interband critical points show a nonlinear behavior with x . Though the weighted

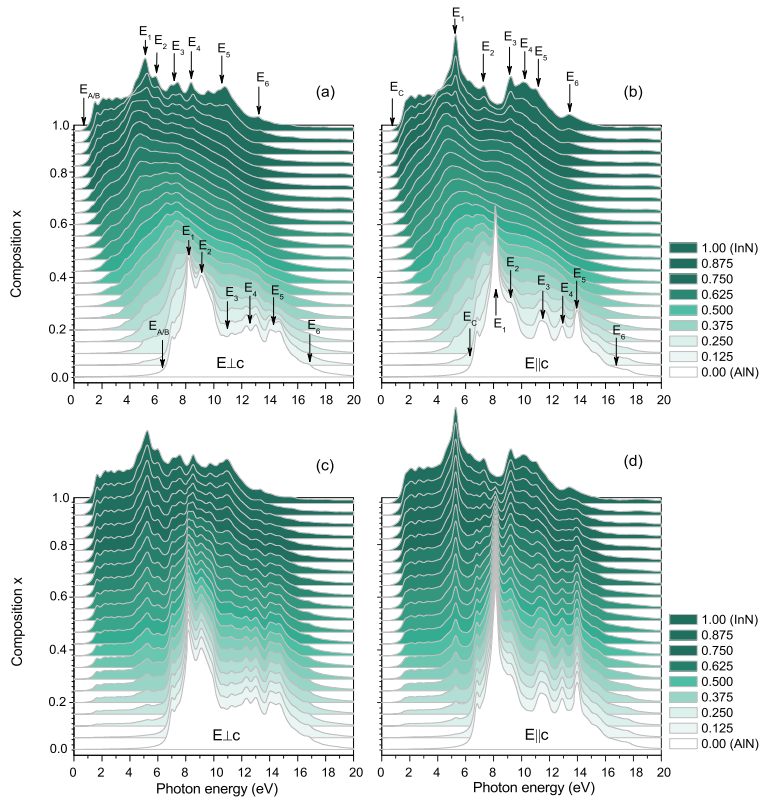


Figure 6.5: Imaginary part of the ordinary (a, c) and extraordinary (b, d) dielectric function $\varepsilon_{\perp/\parallel}(\omega)$ of wz - $\text{In}_x\text{Al}_{1-x}\text{N}$ for varying averaged In compositions x . Results for two different alloy statistics, SRS (a, b) and MDM (c, d) model, are plotted.

combination of the two spectra for $x = 0$ and $x = 1$ gives rise to a seemingly nonlinear variation of the absorption edge in Figs. 6.4(c), 6.4(d), 6.5(c) and 6.5(d) the clear conclusion is that the spectra measured for real alloy samples cannot be explained by a mixing model, independent of the possible characteristic microscopic, mesoscopic or even macroscopic length scale for regions with $x = 0$ and $x = 1$. Therefore, we focus our investigation of the alloy spectra on results obtained within the SRS statistics. This is also supported by the detailed studies of the fundamental gaps of nitride alloys elsewhere [116].

The random distribution of the clusters with weights corresponding to those of a regular solution (cf. section 2.3.3.1) gives rise to peak variations with x which are nonlinear in position and height in Figs. 6.4(a), 6.4(b), 6.5(a), and 6.5(b). Several peaks can be even followed over a wide range of compositions. One has the impression of a continuous variation of the lineshapes. However, this observation but also similar ones for the measured spectra cannot be interpreted in the sense that only one and the same optical transition contributes to such an individual peak structure. Apart from the intermixing of interband transitions by excitonic effects, which already occurs for the binary components [101], the alloying makes such an analysis practically impossible. Still within the cluster approach for each cluster material a band structure and a BZ can be depicted. However, due to the atomic relaxation within each 16-atom cell (which represents structural disorder) and the configurational average (which accounts for chemical disorder) such a symmetry analysis is practically impossible because of the random cation distribution and the related non-uniform modifications of the atomic positions. We cannot be sure that electronic states of nearly the same symmetry con-

tribute to a certain peak with varying position and weight. We come back to this point in the next section.

Starting from InN ($x = 1$) the increasing influence of the second nitride, GaN (Figs. 6.4(a) and 6.4(b)) or AlN (Figs. 6.5(a) and 6.5(b)), is obvious toward $x \rightarrow 0$. This behavior is not only visible in the range of the absorption edge, which can still clearly be identified for an alloy, but also for the frequency range of the higher interband transitions. Thereby, the composition dependence is much more pronounced in $\text{In}_x\text{Al}_{1-x}\text{N}$ compared to $\text{In}_x\text{Ga}_{1-x}\text{N}$ due to the larger fundamental band gap of AlN and the bigger range of absorption with minor frequency variation between the edge and the first main peak in GaN. The variation of the main peak near 7.0 eV (GaN) or 7.5 eV (AlN) is weak. The details of the higher interband transitions will be discussed below.

The differences of the SRS spectra for the different polarization directions are more striking near the end compounds $x = 0$ and $x = 1$. However, as can be seen from the comparison of (a) and (b) in Figs. 6.4 and 6.5 for intermediate compositions x these differences are somewhat smeared out for several reasons. The structural disorder in the alloy modifies the dipole selection rules. Symmetry-related selection rules cannot anymore be formulated for intermediate compositions. Only the global hexagonal anisotropy, which has been taken into the alloy simulation, e. g. in the hexagonal shape of the 16-atom cells, is visible as a dependence on the light polarization. However, near to the end components InN and GaN or AlN the wurzite symmetry becomes dominant for both light polarizations with different dipole selection rules.

6.5 Interband critical points

The absorption lineshapes in Figs. 6.4 and 6.5 with their pronounced peak structures suggest an analysis of the composition dependence of the peaks, at least of their positions, similar to that done interpreting experimental spectra. [200, 231, 250, 251, 255, 259] In principle, Eq. (2.90) for the DF can be approximately replaced by a sum of oscillators j with given energy E_j , oscillator strength C_j , and damping parameter Γ_j . Eq. (2.90) suggests such a division into individual oscillators. Historically, such an approach is driven by the idea that interband transitions govern the DF and because of the peculiarities in the joint density of states (see Fig. 6.1) in the vicinity of critical points of the joint band structure, so-called van-Hove singularities [243]. According to the nature of the critical points such a picture can be additionally refined also if excitonic effects are taken into account [260]. Using this or a similar procedure the composition dependence of several characteristic energies $E_{A/B}$, E_C , E_1, \dots, E_6 [200, 231, 250, 251, 259] has been derived from measured spectra.

Here, we follow this idea despite the limitations of the van-Hove singularity picture due to selection rules and, in particular, excitonic effects [101]. For the binary end components with $x = 0$ and $x = 1$, we use the direct relationship of the peak positions E_1, \dots, E_6 to inter-

Peak	Transition	Polarization	AlN	GaN	InN
E_1	$U_4 - U_1$	\perp, \parallel	–	6.57	4.63
	$M_4 - M_1$	\perp, \parallel	8.36	6.90	5.26
	$L_{1,3} - L_{1,3}$	\perp	8.58	7.26	5.27
E_2	$M_2 - M_1$	\perp	9.80	8.12	6.08
	$K_3 - K_2$	\parallel	9.27	8.49	6.92
E_3	$H_3 - H_{1,2}$	\parallel	10.56	9.38	7.29
	$K_3 - K_3$	\perp	–	10.97	8.81
	$K_3 - K_2$	\perp	11.81	10.94	8.64
	$L_{1,3} - L_{1,3}$	\perp	–	10.59	9.10
E_4	$L_{1,3} - L_{1,3}$	\perp	12.55	10.57	8.43
	$L_{1,3} - L_{1,3}$	\perp, \parallel	12.93	10.59	9.10
	$L_{2,4} - L_{1,3}$	\perp	12.66	10.58	8.48
	$A_{5,6} - A_{1,6}$	\parallel	–	12.16	9.74
E_5	$A_{5,6} - A_{1,6}$	\parallel	–	12.16	10.27
	$H_3 - H_3$	\parallel	14.23	12.15	–
	$A_{1,3} - A_{5,6}$	\parallel	–	13.51	10.87
E_6	$A_{1,3} - A_{1,6}$	\perp, \parallel	16.75	15.41	13.11

Table 6.1: Characteristic interband energies (in eV) related to the peak positions E_1, \dots, E_6 in Figs. 6.4 and 6.5 for ordinary (\perp) and extraordinary (\parallel) light polarization. The symmetry character and the position in the BZ of the valence and conduction band determining the interband energy are indicated. The interband energies follow from the LDA + U + Δ approach and hence can slightly differ from the HSE + GW values in Fig. 6.1.

band transitions at high-symmetry points Γ , M , K , A , L , and H of the hexagonal BZ. Our strategy of identification and labeling of such structures in the theoretical spectra however takes into consideration that these structures can be approximately related to one or more interband transitions that can be identified for the binary end components as illustrated in Table 6.1. Thereby, we restrict ourselves to the most visible peaks and their variation with the composition. As a first structure we follow the position $E_{A/B}$ and E_C of the absorption edge, which however is somewhat higher in energy than the average fundamental gap (see Ref. [116]). The indices A , B , and C refer to the uppermost valence bands which still can be identified for the cluster materials [54]. Because of the neglected small spin-orbit splittings A , B refer to the uppermost Γ_9 and Γ_7 bands while the lower Γ_7 band leads to C . This classification is possible for $\text{In}_x\text{Ga}_{1-x}\text{N}$ and $\text{In}_x\text{Al}_{1-x}\text{N}$ for $x \gtrsim 0.25$. For AlN-rich $\text{In}_x\text{Al}_{1-x}\text{N}$ alloys the average crystal-field splitting becomes negative and valence bands cross [109, 116]. In this limit the higher Γ_7 band [116] is related to C in Figs. 6.4 and 6.5. Nevertheless we keep the labeling according to the dipole selection rule for light polarization parallel to the hexagonal axis.

The other labels 1, ..., 6 are simply related to the energetical ordering of the peak structures. The corresponding results from LDA+U+ Δ approach in Table 6.1 allow us at least an identification that is correct for InN and GaN or AlN. Thereby, we assume that the related interband energies are slightly higher than the peak energies in order to account for the general excitonic redshift. In Table 6.1 we have listed LDA+U+ Δ results since this electronic structure approximation has been used to compute the spectra in Figs. 6.4 and 6.5. Table 6.1 shows that the peak identification E_1, \dots, E_6 and the relation of the peaks to certain interband transitions is sometimes difficult. In some cases several transitions from different high-symmetry points may contribute. For $\text{In}_x\text{Al}_{1-x}\text{N}$ it is difficult to identify transitions with the same symmetry which contribute to a particular peak varying from $x = 0$ to $x = 1$.

If at all it is possible close to the binary end components, especially for $\text{In}_x\text{Ga}_{1-x}\text{N}$ close to InN and GaN. However, already for intermediate compositions such an identification is

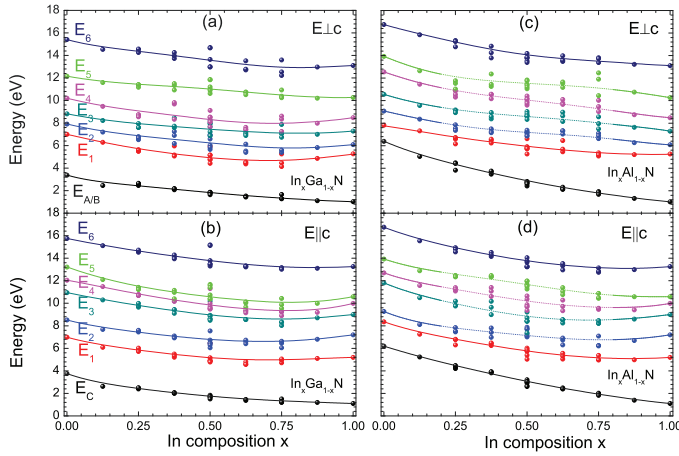


Figure 6.6: Interband transition energies taken from Figs. 6.4 and 6.5 for $\text{In}_x\text{Ga}_{1-x}\text{N}$ (a,b) and $\text{In}_x\text{Al}_{1-x}\text{Al}_{1-x}\text{N}$ (c,d) versus composition x . Energies taken from the ordinary (a,b) (extraordinary (b,d)) spectrum. The dots indicate corresponding energies for individual clusters. The dotted lines in (c,d) indicate the mentioned difficulties to identify the symmetry of the interband transitions.

questionable because of the complete loss of translational and point-group symmetries in the alloys. The situation is worse for $\text{In}_x\text{Al}_{1-x}\text{N}$ because of the stronger internal strains. Nevertheless, the development of selected peak structures can be followed with the composition also in the intermediate range of x where many classes of clusters contribute to the spectra. An example for which the identification can be done is the E_1 peak in $\text{In}_x\text{Al}_{1-x}\text{N}$ ($\text{In}_x\text{Ga}_{1-x}\text{N}$) for ordinary polarization. It varies from 8.1 eV (7.2 eV) ($x = 0$) to about 5.2 eV ($x = 1$). According to Table 6.1 and Fig. 6.1 the main contributions may be due to the lowest interband transitions on the LM line of the BZ. The identification seems to be obvious. However, for intermediate and small x a second peak occurs for both $\text{In}_x\text{Al}_{1-x}\text{N}$ and $\text{In}_x\text{Ga}_{1-x}\text{N}$ which can be described by a strong non-linear composition-dependent bowing parameter (see below). Another interpretation in terms of a huge joint density of states at these energies of the Al-rich or Ga-rich clusters $\text{In}_{n_j}\text{X}_{8-n_j}\text{N}_8$ is also possible, but will not demonstrate here.

The results for the peak positions in Figs. 6.4 and 6.5, i.e., energy E_j versus composition x , are summarized in Fig. 6.6. The corresponding peak positions of the individual cluster materials are also given. Because of the above discussed difficulties to relate all peaks for the entire composition interval in the case of $\text{In}_x\text{Al}_{1-x}\text{N}$, we focus the discussion on the composition dependence in the case of $\text{In}_x\text{Ga}_{1-x}\text{N}$.

In general, the composition dependence of the peak maxima in Fig. 6.6(a) and Fig. 6.6(b) exhibits a significant bowing which may be described by Eq. (4.4) in $P = E_j$, with a composition-dependent bowing parameter $b_i(x)$. The general bowing has been discussed in detail for the absorption edges and emission lines before [116]. In this work, we have suggested a non-linear composition dependence according to Eq. (4.5).

Here, we apply this formula also to the higher interband transitions. The fits of Eq. (4.4) to the curves in Fig. 6.6(a) and Fig. 6.6(b) lead to the coefficients b_{i0} and b_{i1} of the bowing parameter $b_i(x)$ for the higher interband transitions in $\text{In}_x\text{Ga}_{1-x}\text{N}$ as given in Table 6.2. The values in Table 6.2 clearly indicate by b_{i0} a bowing of the same order of magnitude or a somewhat larger bowing (with exception of E_5) as for the fundamental gap [116]. The non-linearity of the bowing indicated by b_{i1} in Table 6.2 is small. Only for the lowest ab-

Transition i	ordinary		extraordinary	
	b_{i0}	b_{i1}	b_{i0}	b_{i1}
1	4.43	-0.25	3.81	0.17
2	2.85	-0.44	3.98	-0.25
3	2.35	-0.34	3.51	-0.42
4	3.67	-0.43	3.83	-0.63
5	0.90	-0.54	5.16	-0.25
6	2.45	0.57	2.54	-0.43
A/B, C	2.07	1.16	3.82	1.47

Table 6.2: Coefficients of the bowing parameter (Eq. 4.4) for higher interband transitions in the optical absorption spectra of Fig. 6.4 for $\text{In}_x\text{Ga}_{1-x}\text{N}$. Values for both light polarizations are listed.

sorption peaks at $E_{A/B}$ or E_C remarkable values b_{i1} are predicted. The order of magnitude of the bowing parameters agrees with such derived from measured spectra [231, 251] but the theoretical values are somewhat larger. The strongest deviations from a constant bowing parameter $b_i(x) = b_{i0}$ occurs for the absorption edges. For higher interband transitions the composition dependence of the bowing parameters can be nearly neglected.

The bowing parameters b_i derived for higher energy peaks E_1, \dots, E_2 from measured data [231, 251] are in general somewhat smaller than the values in Table 6.1. The seemingly over-estimation of the bowing parameters by our calculations with respect to experimental values [231, 251] may be a consequence that the data in Table 6.2 have been derived from spectra in Figs. 6.4(a) and 6.4(b) which have been computed for one limiting case of the cluster statistics, the strict-regular solution model. Small contributions from other distributions of the In atoms which locally may approach the MDM statistics instead of the SRS one would lead to a significant reduction of the bowing. This explanation is somewhat in contrast to the findings for the fundamental absorption edge in Sec. 5.4 which have clearly indicated that the composition dependence of the fundamental gap, especially its bowing, measured by absorption (instead of photoluminescence) can be approximately explained using the SRS limit of the cluster statistics. However, there it is also clearly illustrated that fluctuations of observable quantities may influence the bowing for a given average composition.

6.6 Excitonic effects

We focus on $\text{In}_x\text{Al}_{1-x}\text{N}$ alloys. Because of the smaller dielectric constants of AlN, stronger excitonic effects are expected for not too large In molar fractions, i.e., for $x \rightarrow 0$. This focus is supported by the larger binding energies of the band-edge excitons of 58 meV in AlN [261] compared to the values of about 26 meV in GaN [?] and 4 meV in InN [64]. In order to illustrate the excitonic effects in Fig. 6.7 we plot the difference of $\text{Im } \epsilon_{\perp/\parallel}(\omega)$ with and without excitonic and LFEs for $\text{In}_x\text{Al}_{1-x}\text{N}$ for the two limiting cases of cluster statistics, SRS and MDM.

We show only positive differences. Negative values of the differences are ignored. In such a way the most important excitonic effects due to bound exciton states, Coulomb enhancement of the absorption edge, and redistribution of spectral strength from higher to lower photon energies are illustrated. The small vertical arrows indicate the QP gaps of the cluster

configurations of class j and n_j In atoms which significantly contribute to the spectrum for a given average composition x . This is essentially important for the case of the SRS cluster statistics in Figs. 6.7(a) and 6.7(c) because bound excitons may occur in each cluster material. They belong to the corresponding local quasiparticle gap and, therefore, may appear as resonance states in the alloy spectra for intermediate compositions x . However, such bound states are only visible in Fig. 6.7 for AlN-rich alloys since the time-evolution technique [83] used for the calculation of the spectra does not resolve bound states with too small binding energies down to the InN value (see discussion in Ref. [64]).

The two difference spectra in Figs. 6.7(b) and 6.7(d) for the MDM statistics exhibit characteristic excitonic effects in different spectral regions. For lower frequencies they indicate a redistribution of spectral strength and some Coulomb enhancement [243] in the InN-dominated part of the spectra but no bound excitons, at least within the numerical description used. In the higher energy range around 6 eV for both light polarizations a peak related to excitonic bound states is visible in the spectra below the QP gap of wz -AlN belonging to the Γ_5 or Γ_1 valence-band maximum. Because of the MDM statistics the strength of the bound states are weighted by $(1 - x)$, the AlN content.

In the case of the other limit of the alloy statistics, the SRS model, in Figs. 6.7(a) and 6.7(c) the spectral distributions are completely different for intermediate compositions x . There is a continuous variation of the absorption edge modified by excitonic effects from $x = 0$ to $x = 1$. In the AlN-rich region of the alloy spectra, in contrast to the InN-rich spectra, still excitonic effects at the absorption edges $E_{A/B}$ and E_C (more precisely, below the local quasiparticle gap) are observable. In order to illustrate these effects the fundamental energy gaps of the most contributing cluster materials are indicated by arrows. The spectral features below these arrows may be identified with bound exciton states below the corresponding QP gaps in the cluster materials, which may form resonant states in the global alloy spectrum for a given composition x . Indeed such features are visible, but seemingly not significantly shifted by varying the average composition x of the random alloy.

Such a 'bound' exciton peak indeed occurs below the edge of the $n_j = 1$ $\text{In}_1\text{Al}_7\text{N}_8$ cluster material for both light polarizations. The energy position is rather fixed whereas its intensity is drastically reduced with rising composition x . For the $n_j = 2$ edges such peaks are also resolvable. In principle, all these peaks represent resonance states since they appear at photon energies where clusters with another composition already generate some absorption. The excitonic features occurring in the spectra of Figs. 6.7(a) and 6.7(c) however represent only one possible type in alloys. They belong to a class of Wannier-Mott excitons [243] in a random alloy which are not influenced by confinement effects. In our description using the configurational average Eq. (2.91) and the calculation of spectra for isolated cluster materials only such Wannier-Mott excitons whose Bohr radius is smaller than the extent of characteristic composition fluctuations Δx are correctly described. Thereby, the Bohr radii may

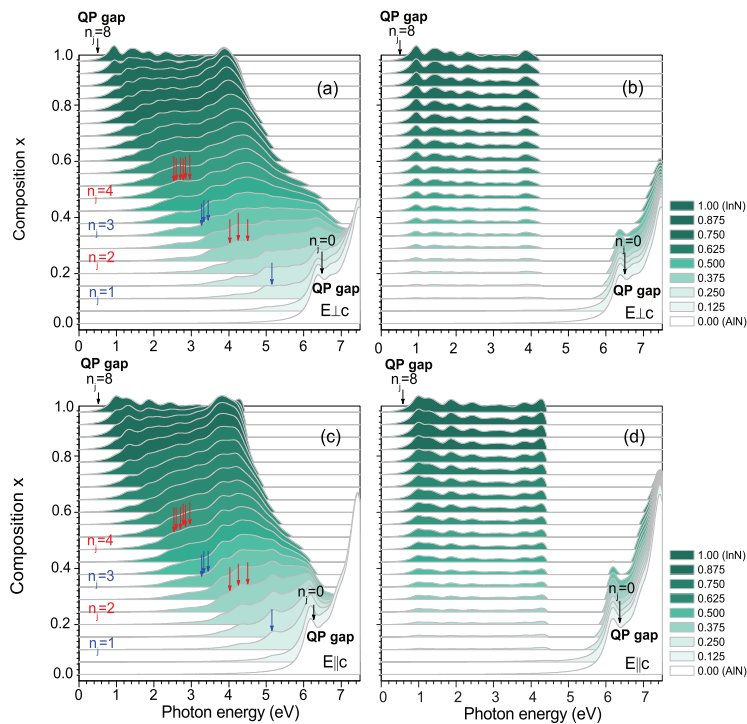


Figure 6.7: Difference of imaginary parts of dielectric function $\varepsilon_{\perp,\parallel}(\omega)$ with and without excitonic/local-field effects of $\text{In}_x\text{Al}_{1-x}\text{N}$ for (a,b) ordinary and (c,d) extraordinary polarization and two different cluster statistics, SRS (a,c) and MDM (b,d). The arrows indicate the QP gaps for $\text{In}_{n_j}\text{Al}_{8-n_j}\text{N}_8$ cluster materials.

vary in a range of about 1 nm (AlN-rich) until about 10 nm (In-rich) if a rough effective-mass approximation [243] is applied to estimate the exciton binding.

We have to inform the reader that our cluster-expansion method and computation of the alloy spectra according to the Connolly-Williams formula (2.91) cannot describe all excitonic phenomena in an alloy. When clustering and/or composition fluctuations [116, 166] occur with characteristic length scales smaller than the Bohr radii, then our approach cannot anymore correctly describe the exciton effects. Due to the calculation of the spectrum for each individual cluster material as a periodic structure with 16-atom cells local confinement effects on the electrons and/or holes are not taken into account. Quantum confinement related to strong composition fluctuations on a few nm-length scale and corresponding small InN-rich areas in the alloy are not included in the present alloy description.

6.7 Dielectric properties

The real part of the calculated DF at vanishing frequency, $\text{Re}\varepsilon_{\perp,\parallel}(\omega = 0) = \varepsilon_{\infty\perp,\parallel}$, describes the tensor of the macroscopic electronic dielectric constant that has two independent components $\varepsilon_{\infty\perp}$ and $\varepsilon_{\infty\parallel}$ in hexagonal systems. The results of the corresponding configurational average are plotted in Fig. 6.8 as functions of the average composition x in the limit of the strict-regular solution model. In order to illustrate the influence of the local geometries, also the dielectric constants for the individual cluster materials $\text{In}_{n_j}\text{X}_{8-n_j}\text{N}_8$ ($X = \text{Ga}, \text{Al}$) are depicted in Fig. 6.8. The dielectric constants are calculated including excitonic and local-field effects using the procedure described in section 2.2.5. In contrast to

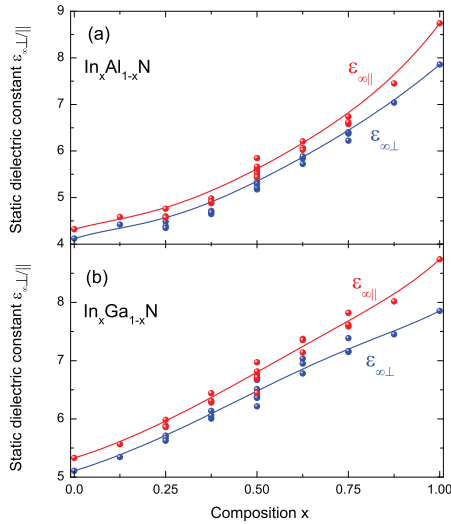


Figure 6.8: The independent components $\epsilon_{\infty\perp}$ (perpendicular to the c -axis, blue lines) and $\epsilon_{\infty\parallel}$ (parallel to the c -axis, red lines) are plotted versus the average composition x for (a) $\text{In}_x\text{Ga}_{1-x}\text{N}$ and (b) $\text{In}_x\text{Al}_{1-x}\text{N}$ alloys described within the SRS model. The values for the individual cluster materials are indicated by dots.

many other theoretical values presented in the literature here really macroscopic dielectric constants and not only such within the independent-particle or independent-quasiparticle approach [102] have been computed.

The values calculated for the end components at $x = 0$ and $x = 1$ with wurtzite structure are in excellent agreement with measured data [263, 264]. Our values are $\epsilon_{\infty\perp} = 4.12, 5.11,$ and 7.86 and $\epsilon_{\infty\parallel} = 4.32, 5.30,$ and 8.74 for AlN, GaN, and InN, respectively. The corresponding experimental values [263, 264] are $\epsilon_{\infty\perp} = 4.14, 5.19,$ and 7.83 and $\epsilon_{\infty\parallel} = 4.28, 5.32,$ and 8.03 . The agreement is excellent for all nitrides only for InN the theory slightly overestimates the electronic dielectric constant in the parallel case. Two reasons may be mentioned. The small discrepancy of 0.7 for $\epsilon_{\infty\parallel}$ in the InN case may be a consequence of the numerical treatment, for instance the used LDA+ U + Δ method, but also due to difficulties to measure precisely the dielectric constant for light polarization parallel to the c -axis in real samples. Moreover, an influence of strain and free carriers cannot be fully excluded.

The plots of the dielectric constants calculated for the SRS statistics versus composition x in Fig. 6.8 indicate some bowing similar to the fundamental energy gaps [116]. We therefore describe the variation of the dielectric constants with the composition according to Eq. 4.4 with $P = \epsilon_{\infty\perp/\parallel}$ and $P_b = \Delta\epsilon_{\infty\perp/\parallel}$ the composition-independent bowing parameters. The strongest bowing of the dielectric constants happens for the $\text{In}_x\text{Al}_{1-x}\text{N}$ alloy. The values amount to $\Delta\epsilon_{\infty\perp} = 2.54$ and $\Delta\epsilon_{\infty\parallel} = 3.77$ while roughly $\Delta\epsilon_{\infty\perp} = 0.09$ and $\Delta\epsilon_{\infty\parallel} = 1.05$ is derived for $\text{In}_x\text{Ga}_{1-x}\text{N}$. Thereby, the almost vanishing ordinary value of $\Delta\epsilon_{\infty\perp}$ is a result of a curve in Fig. 6.8(b) that is not concave and, hence, difficult to determine. The calculated composition dependence of $\epsilon_{\infty\perp}(x)$ for AlN-rich $\text{In}_x\text{Al}_{1-x}\text{N}$ alloys is close to measured variations [200]. Changes in the cluster statistics influence the bowing. If, for instance, only the 22 cluster classes indicated in Fig. 6.8 are averaged, one obtains $\Delta\epsilon_{\infty\perp} = 2.97$ and $\Delta\epsilon_{\infty\parallel} = 4.20$ ($\text{In}_x\text{Al}_{1-x}\text{N}$) or $\Delta\epsilon_{\infty\perp} = 0.14$ and $\Delta\epsilon_{\infty\parallel} = 1.16$ ($\text{In}_x\text{Ga}_{1-x}\text{N}$).

7

Summary

"Sorrir não significa necessariamente que você está feliz. Às vezes significa apenas que você é forte."

Cazuza

In this work, we modeled properties of group-III nitrides and their alloys by means of *ab initio* methods. The ground-state (energetic, structural, elastic) and excited-state (energy bands and band parameters) properties of the *zb* and the *wz* polytypes of AlN, GaN, and InN have been investigated using modern parameter-free approaches. From the comparison of different approximations of XC it has been shown that the AM05 XC functional gives rise to atomic geometries in excellent agreement with experimental data and, therefore, circumvents the overbinding (underbinding) of the LDA (PBE-GGA). Since the atomic positions are an important prerequisite for calculating the excited-state properties, all this work is based on the AM05 geometry results.

The electronic structure has been calculated by solving a QP equation which includes the XC self-energy of the electrons and holes within the G_0W_0 approximation, based on HSE eigenvalues and wave functions. The resulting gaps are in excellent agreement with experimental values. The influence of hydrostatic strain has been studied for the gaps. Especially the fundamental energy gap of InN varies dramatically with the strain as indicated by the large volume deformation potential.

The calculation of the natural band discontinuities ΔE_c and ΔE_v and the corresponding band line-up yields type-I hetero(crystalline) structures for zinc-blende and wurtzite polytypes of InN and GaN, while a type-II character has almost been found for AlN. Thereby the quantum wells of the electrons are relatively deep with $\Delta E_c = 0.1 - 0.3$ eV. For X electrons in AlN with almost vanishing wave vectors the value $\Delta E_c=1.4$ eV is significantly increased. The situation for holes is completely different. The quantum wells in the cubic inclusions are rather flat for GaN and InN with $\Delta E_v = 0.06$ or 0.09 eV. For AlN the value of ΔE_v is not exactly fixed and can even have a changed sign. However, the small $|\Delta E_v|$ do not indicate the validity of the common anion rule.

Also the influence of the relative QP corrections to the HSE eigenvalues on the VBs around Γ is small. The inclusion of the spin-orbit interaction into the HSE calculations allowed us to study the corresponding energy splittings and to determine $\mathbf{k} \cdot \mathbf{p}$ parameters. Thereby, the validity of the quasicubic approximation for wz -GaN and wz -InN has been found to be questionable, especially due to the influence of the semicore d electrons.

In addition, the effective electron and hole masses are calculated. In the case of the VBs (especially for wz polytypes) band crossings render a parabolic description unfeasible for too large \mathbf{k} regions. Treating XC within the HSE approach, tends to increase the masses and, hence, to lower the band dispersion near Γ . We demonstrate the importance of the spin-orbit interaction for the dispersion and the splittings of the bands around the BZ center and, hence, for the exact band masses. The comparison with measured effective masses shows good agreement with the computed values especially for GaN. For InN polytypes trustable effective masses have been derived.

The structural and electronic properties of wz -derived isostructural $\text{In}_x\text{Ga}_{1-x}\text{N}$ and $\text{In}_x\text{Al}_{1-x}\text{N}$ alloys are calculated using a cluster expansion approach together cluster weights derived from the extremum condition for the mixing free energy, the so-called GQCA. We mainly discussed its limiting cases for the cluster statistics, the strict-regular solution and the microscopic decomposition model. The total-energy optimizations of the cluster materials are also performed within density functional theory using the gradient-corrected AM05 XC functional. In order to obtain the electronic structures, a recently developed quasiparticle method, based on the hybrid HSE06 XC functional and subsequent G_0W_0 corrections and successfully applied for the binary end components before, is used. The branch-point energies of all individual clusters are used to align the quasiparticle energies of all clusters on a common energy scale.

We find that the cluster materials that are structurally ordered (mostly in c -axis direction) are energetically less favorable. The lowest energies are computed for the cluster classes with a high tendency for clustering, i. e., large deviation of the actual cation-site occupation of the tetrahedra from the average value $n_j/2$ and, hence, $D_j \rightarrow 1$. The influence of the cluster statistics on the structural properties is rather weak and we conclude that the deviations from Vegard's rule are small but measurable, especially for $\text{In}_x\text{Al}_{1-x}\text{N}$. In the case of the bulk modulus, the deviations are slightly larger. Overall, the energetic, structural, and elastic properties of the alloys are less sensitive to the details of the local distribution of the cations.

The electronic properties, however, are much more sensitive to the distribution of the cations over the alloy. For the two limiting cluster statistics studied in this work, the variation of the quasiparticle DOS (peak positions as well as peak intensities) with the composition x is completely different. Composition-dependent band edges as well as the positions of the three uppermost valence bands at the Γ point (along with their splittings) are derived. In this context, the difficulties, that arise from the lower symmetry of the clusters with intermediate

compositions as well as from the different band ordering in InN and AlN, are discussed.

Comparing the calculated energy gaps to measured data, clearly shows that the strict-regular solution statistics seems to yield a more realistic picture than the macroscopic decomposition model. Since the large variety of results for band gaps from optical measurements falls between the curves for the average gap $E_g(x)$ and the one reduced by the mean square deviation, $E_g(x) - \Delta E_g(x)$, we conclude that composition fluctuations in the alloys play an important role at least for absorption edges and emission lines. The measured absorption onsets appears close to $E_g(x)$, whereas the luminescence data approaches $E_g(x) - \Delta E_g(x)$. The latter fact is in agreement with the picture that excited electron-hole pairs prefer to radiatively recombine in the domains of the alloy that have the lowest band gap.

The optical properties of $wz \text{In}_x\text{Ga}_{1-x}\text{N}$ and $\text{In}_x\text{Al}_{1-x}\text{N}$ alloys have been described in the framework of two basic approximations. (i) The alloys are modeled by a cluster expansion method. Each alloy is divided into clusters of artificial materials each of which is represented by a hexagonal crystal containing 16 atoms in the unit cell. The number of cations, In and X = Ga, Al atoms, varies between 0 and 8. The cluster statistics is described by the results of two limiting cases, a complete regular solution or a complete decomposition on a microscopic length scale. The probabilities to find a certain cluster material in the alloy have been used to perform the configurational average. It allows the computation of the configurationally averaged frequency-dependent dielectric function for a given light polarization from the functions calculated for the individual cluster materials. (ii) In order to derive these individual dielectric functions we have applied the most sophisticated many-body approaches. In a first step the quasiparticle electronic structure has been derived for each cluster material. In order to fulfill the conditions for an extremely dense \mathbf{k} -point sampling calculating the optical spectra including excitonic effects in the next step an approximate QP scheme LDA + U + Δ has been adapted. Screened Coulomb attraction of quasielectrons and quasiholes as well as unscreened electron-hole exchange interaction are taken into account.

The variation of the resulting absorption spectra with the average alloy composition x seems to indicate that optically the cation distribution in the chemically (and hence somewhat structurally) disordered ternary compounds is better described by the cluster statistics of a strict regular solution. Close to the end components InN and GaN or AlN the most important spectral features can be still explained by critical points in the interband band structure. However, for intermediate average compositions x such a relation between electronic structure and optical absorption peaks becomes difficult or even impossible for $\text{In}_x\text{Al}_{1-x}\text{N}$. The bowing of such higher interband transitions energies seems to be larger than that found for the absorption edge. Excitonic and local-field effects influence the entire spectra. However, despite alloying also bound excitons remain visible below the absorption edge, especially for AlN-rich $\text{In}_x\text{Al}_{1-x}\text{N}$ alloys.

8

Future perspectives

*"É necessário que as coisas acabem,
para que coisas novas aconteçam."*

Eckhart Tolle

Owing to the high scientific interest in new technologies the research field on semiconductors based on novel materials especially nitrides, began more than three decades ago. Despite of its trouble history, especially for GaN, it became so challenging that attracted a widespread attention. Concomitantly, the modeling of semiconducting alloys whose structural, electronic and optical properties can be totally tailored blossomed as a promising area of solid-state-physics. From the theoretical point of view, along these years the evolution of computers and potential performance of softwares made possible an intense and deep research in alloys and their binary end components using the most-modern theoretical methods combined with theoretical spectroscopy techniques, inclusion of one or two particles excitations, and also many-body effects as being treated by means of many-body perturbation theory.

In a technological way, the constructions of heterojunctions composed of binary, ternary and quaternary group-III nitrides alloys have provide great freedom in optimize device structures. However, nitride-based transistors for microwave power systems still fail. They are a dare due to the problems with manufacturing and high cost of their constituents.

So far, the lack of efficient LEDs that emits in the yellow-green range part of the spectrum the, so-called *green-gap*, it is among the biggest challenges in group-III nitrides alloys. Although theoretically it is possible to perform green LEDs emitting in the wavelength range from 500 nm to 570 nm, their practical realization is a challenge. Another issue is the so-called *drop-problem*. Here, the efficiency of the green-LEDs drops when the electrical power input increases. Another problems such as presence of free carriers and their influence on absorption and emission as well as Auger recombinations are not yet clarified. Defect levels as carrier scattering and non-radiative recombination process also increase the problems of group-III nitrides specially when we come to the green-gap region or think in laser diodes. Actually these problems have been traced back by research groups in all word, however still

remains open.

Theoretically, to predict the solution of such problems is also difficult and is still under debate. The most modern *ab initio* techniques of electronic structures and powerful computers are the tools which may be used to circumvent these problems. However, actually it is not clear, if group-III nitrides and their alloys will be treated in such way, to cover the wide range spectra. In this case, the problems are different from those accounted and faced by II-VI or III-V group semiconductors. It means that a deep knowledge of III-nitrides group still needs new strands combined with that acquired actually.

Also it is important to note that collaboration between theoretical and experimental researches are fundamental in order to result opportunities and experiences. Concomitantly it is shared knowledge providing skills beyond of the achieved until nowadays.

Thus, many properties and applications of group-III nitrides and their alloys are established. However, as aforementioned, there are still many open questions in III-group nitrides and their alloys. Up to now, many possible paths have been highlighted, which can possibly inspire new projects for new researches. Furthermore, the results presented here can be also starting point for future applications and novel models based on many-body problems treated by *ab initio* methods.

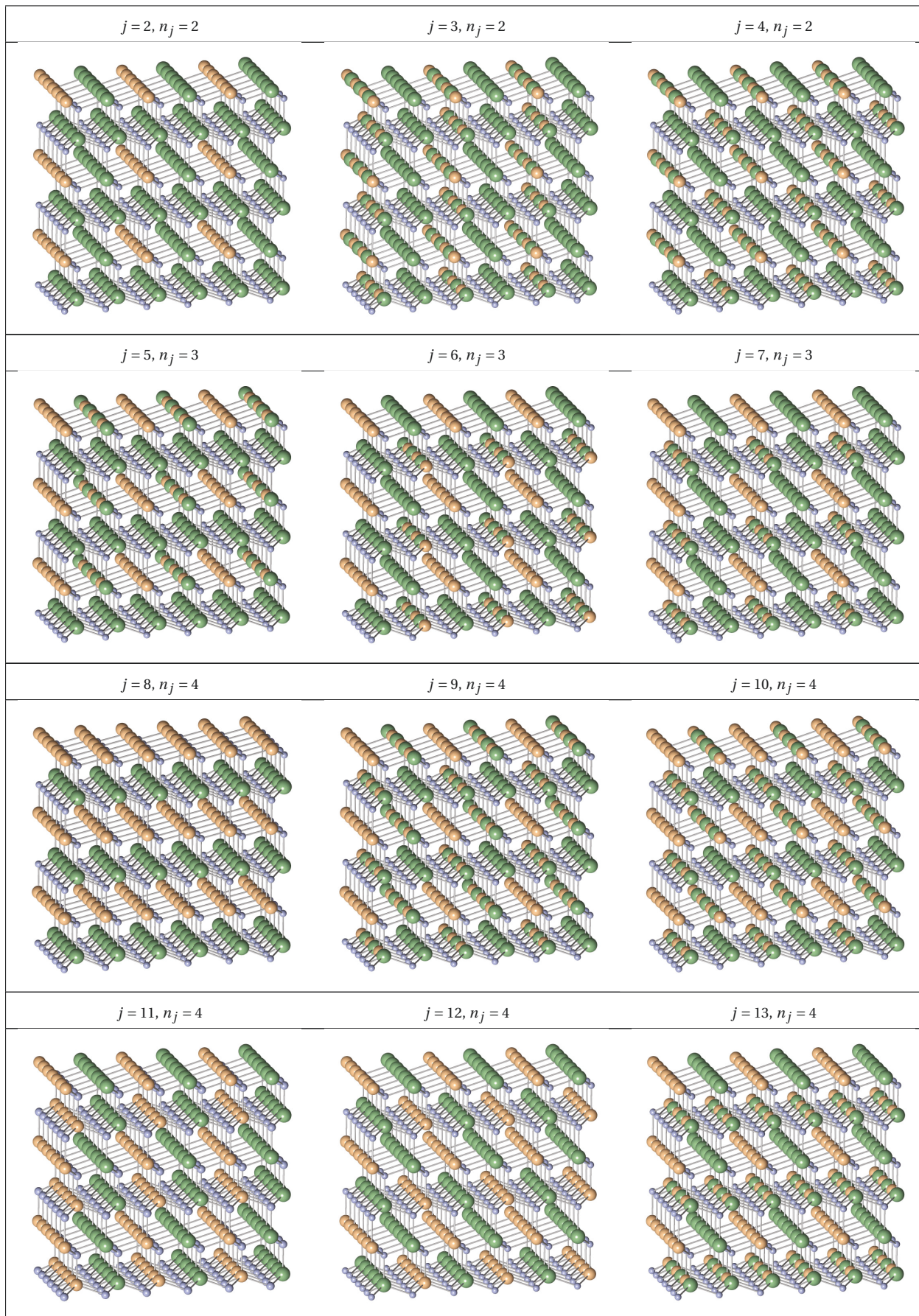
A

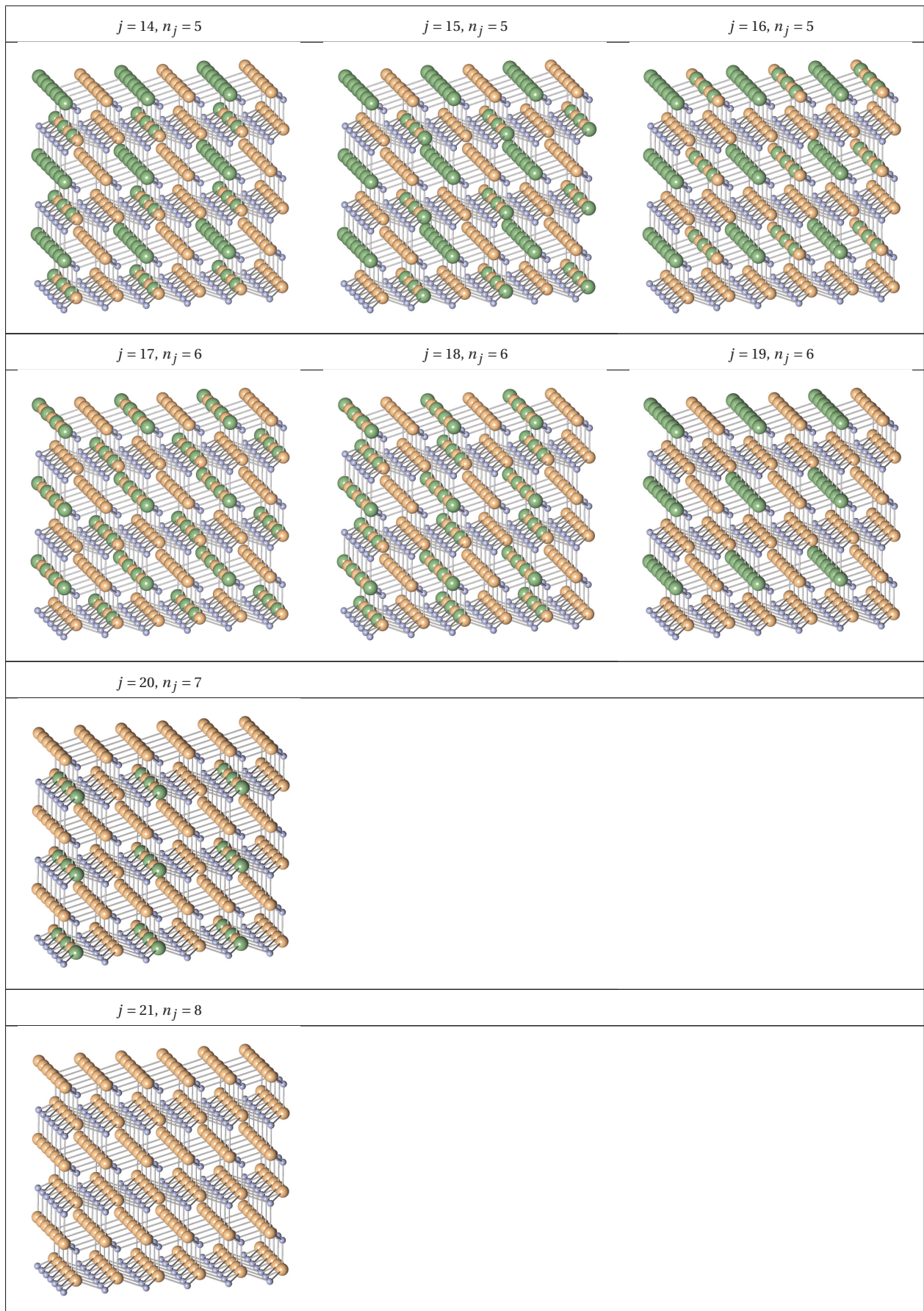
Appendix

A.1 Atomic arrangement of the 22 cluster classes

The atomic arrangement of the 22 cluster classes $j = 0, \dots, 21$ are presented with number of indium contents n_j . In Table 4.1, the properties of the 22 cluster classes for $\text{In}_{n_j}\text{Ga}_{8-n_j}\text{N}_8$ and $\text{In}_{n_j}\text{Al}_{8-n_j}\text{N}_8$ are given.







A.2 Cluster expansion for the wurtzite alloys

In this work, in order to predict the configurational average for structural, electronic and optical properties of group-III nitride alloy, it was used *ab initio* methods combined with alloys statistics, more specifically SRS and MDM, limiting case of GQCA. In this sense, for a more realistic results it is necessary a reasonable number of samples of each property in order to obtain the average. Though the smallest hexagonal crystal structure contains 4-atoms unit cell, here it have used 16-atoms supercell (cf. Fig. 2.2) that include a considerable local correlation. Considering the pseudo ternary alloy $A_xB_{1-x}C$ with $A = \text{Al, Ga or In}$, we account for a huge possibility of configurations due the arrangement of the cations. The total number accounts taking the combinatory $\binom{8}{n_j}$ where n_j is, e. g., the number of A cations [84, 90].

Taking all possibilities of arrangements into account, we obtain by

$$\sum_{n_j=0}^8 \binom{8}{n_j} \quad (\text{A.1})$$

256 possibles configurations. However, by arguments of symmetry and energy degeneracy, that 256 possibilities can be grouped in 22 (j) different classes as described below in Table A.2

j	n_j	g_j	number of cations (A)
0	0	1	-
1	1	8	1
2	2	12	1,2
3	2	12	1,5
4	2	4	1,8
5	3	8	1,2,3
6	3	24	1,2,7
7	3	24	1,2,5
8	4	2	1,2,3,4
9	4	8	1,2,3,5
10	4	24	1,2,4,5
11	4	6	1,2,5,6
12	4	6	1,2,7,8
13	4	24	1,2,5,8
14	5	24	3,4,6,7,8
15	5	24	3,4,5,6,8
16	5	8	4,5,6,7,8
17	6	4	2,3,4,5,6,7
18	6	12	2,3,4,6,7,8
19	6	12	3,4,5,6,7,8
20	7	8	2,3,4,5,6,7,8
21	8	1	1,2,3,4,5,6,7,8

Table A.2: Class j , number of cations n_j and g_j the degeneracy factor for a 16-atom unit cell in wurtzitic crystal structure. For each class j the number n_j of A cations, the degeneracy g_j of the class, and the cation sites occupied with A-type atoms (for one representative of the class) are given.

A.3 Parameters of calculations

A.3.1 Scissors operator (Δ)

j	Δ_j (eV) for $\text{In}_{n_j}\text{Ga}_{8-n_j}\text{N}_8$	Δ_j (eV) for $\text{In}_{n_j}\text{Al}_{8-n_j}\text{N}_8$
0	1.097	1.943
1	1.291	1.708
2	1.004	1.444
2	0.982	1.472
4	0.942	1.456
5	0.832	1.279
6	0.851	1.309
7	0.834	1.241
8	0.687	1.081
9	0.661	1.018
10	0.672	1.049
11	0.679	1.034
12	0.703	1.158
13	0.683	1.069
14	0.526	0.845
15	0.537	0.901
16	0.514	0.845
17	0.377	0.692
18	0.499	0.639
19	0.42	0.641
20	0.204	0.344
21	0.252	0.252

Table A.3: scissors operators Δ_j for each cluster class j in $\text{In}_{n_j}\text{Ga}_{8-n_j}\text{N}_8$ and $\text{In}_{n_j}\text{Al}_{8-n_j}\text{N}_8$ pseudobinary alloy.

Bibliography

- [1] G. Busch, *Eur. J. Phys.* **10**, 254 (1989).
- [2] A. Volta, *Del modo di render sensibilissima la più debole elettricità sia naturale, sia artificiale*, Vol. 72 (Phil. Trans. R. Soc. Lond., 1782) p. 237.
- [3] T. J. Seeback, *Abhandl. Deut. Akad. Wiss. Berlin*, 265(1822).
- [4] M. Faraday, *Experimental Researches in Electricity* **Series IV**, 433 (1833).
- [5] F. Braun, *Anal. Phys. und Chem.* **153**, 556 (1874).
- [6] C. E. Fritts, *Amer. Science* **26**, 465 (1883).
- [7] W. Smith, *I. Soc. Telegraph Engineers*, **2**, 31 (1873).
- [8] L. Lukasiak and A. Jakubowski, *J. of Telecomm. Inform. Tech.* **1**, 3 (2010).
- [9] A. H. Wilson, *Proc. Roy. Soc. London* **Ser. A**, 133:458 (1931).
- [10] A. H. Wilson, *Proc. Roy. Soc. London* **Ser. A**, 134:277 (1931).
- [11] J. Bardeen and W. H. Brattain, *Phys. Rev.* **74**, 230 (1948).
- [12] P. Hohenberg and W. Kohn, *Phys. Rev.* **136**, B864 (1964).
- [13] W. Kohn and L. J. Sham, *Phys. Rev.* **140**, A1133 (1965).
- [14] G. Onida, L. Reining, and A. Rubio, *Rev. Mod. Phys.* **74**, 601 (2002).
- [15] J. Wu, W. Walukiewicz, W. Shan, K. M. Yu, J. W. Ager, S. X. Li, E. E. Haller, H. Lu, and W. J. Schaff, *J. Appl. Phys.* **94**, 4457 (2003).
- [16] I. Gherasoiu, M. O’Steen, T. Bird, D. Gotthold, A. Chandolu, D. Y. Song, S. X. Xu, M. Holtz, S. A. Nikishin, and W. J. Schaff, *Phys. Status Solidi C* **5**, 1642 (2008).
- [17] V. Davydov, A. Klochikhin, V. Emtsev, D. Kurdyukov, S. Ivanov, V. Vekshin, F. Bechstedt, J. Furthmüller, J. Aderhold, J. Graul, A. Mudryi, H. Harima, A. Hashimoto, A. Yamamoto, and E. E. Haller, *Phys. Status Solidi B* **234**, 787 (2002).
- [18] I. Vurgaftman and J. R. Meyer, *J. Appl. Phys.* **94**, 3675 (2003).
- [19] M. Razeghi, *IEEE Photonics Journal* **3**, 263 (2011).
- [20] H. Lu, W. J. Schaff, and L. F. Eastman, *J. Appl. Phys.* **96**, 3577 (2004).
- [21] I.-K. Park and S. Park, *App. Phys. Express* **4**, 042102 (2011).
- [22] H. Ohta, S. P. DenBaars, and S. Nakamura, *J. Opt. Soc. Am. B* **27**, B45 (2010).
- [23] F. Medjdoub, J.-F. Carlin, M. Gonschorek, E. Feltin, M. A. Py, D. Ducatteau, C. Gaquiere, and E. Grandjean, *N. Kohn, IEDM Tech. Dig.* **1**, 1 (2006).
- [24] S. F. Chichibu, A. Uedono, T. Onuma, B. A. Haskell, A. Chakraborty, T. Koyama, P. T. Fini, S. Keller, S. P. Denbaars, J. S. Speck, U. K. Mishra, S. Nakamura, S. Yamaguchi, S. Kamiyama, H. Amano, I. Akasaki, J. Han, and T. Sota, *Philos. Magazine* **87**, 2019 (2007).
- [25] S. F. Chichibu, A. Uedono, T. Onuma, B. A. Haskell, A. Chakraborty, T. Koyama, P. T. Fini, S. Keller, S. P. Denbaars, J. S. Speck, U. K. Mishra, S. Nakamura, S. Yamaguchi, S. Kamiyama, H. Amano, I. Akasaki, J. Han, and T. Sota, *Nature Materials* **5**, 810 (2006).
- [26] W. Aulbur, L. Jönsson, and J. Wilkins, “Solid state physics: Advances in research and applications,” (2000) Chap. Quasiparticle calculations in solids, p. 1.
- [27] A. Tkatchenko and M. Scheffler, *Phys. Rev. Lett.* **102**, 073005 (2009).
- [28] V. A. Parsegian, *Van der Waals Forces: A Handbook for Biologists, Chemists, Engineers and Physicists* (Cambridge, 2005).
- [29] M. Born and J. R. Oppenheimer, *Ann. Phys.* **389**, 457 (1927).

- [30] W. Kohn, *Rev. Mod. Phys.* **71**, 1253 (1999).
- [31] R. M. Martin, *Electronic Structure - Basic Theory and Practical Methods* (Cambridge, 2004).
- [32] L. H. Thomas, *Proc. Cambridge Phil. Roy. Soc.* **23**, 542 (1927).
- [33] E. Fermi, *Rend. Accad. Naz. Lincei* **6**, 602 (1927).
- [34] P. A. M. Dirac, *Proc. Cambridge Phil. Roy. Soc.* **26**, 376 (1930).
- [35] J. C. Slater, *Phys. Rev.* **81**, 385 (1951).
- [36] K. Capelle, *Braz. J. Phys.* **36**, 1318 (2006).
- [37] M. M. Pant and A. K. Rajagopal, *Solid State Commun.* **10**, 1157 (1972).
- [38] U. von Barth and L. Hedin, *Journal of Physics C: Solid State Physics* **5**, 1629 (1972).
- [39] G. Kresse and J. Furthmüller, *Comp. Mater. Sci.* **6**, 15 (1996).
- [40] G. Kresse and D. Joubert, *Phys. Rev. B* **59**, 1758 (1999).
- [41] W. A. Harrison, *Electronic Structure and the Properties of Solids: The Physics of the Chemical Bond* (Freeman, 1980).
- [42] O. Gunnarsson and B. I. Lundqvist, *Phys. Rev. B* **13**, 4274 (1976).
- [43] D. M. Ceperley and B. J. Alder, *Phys. Rev. Lett.* **45**, 566 (1980).
- [44] J. P. Perdew and A. Zunger, *Phys. Rev. B* **23**, 5048 (1981).
- [45] U. von Barth and L. Hedin, *J. Phys. C Solid State* **5**, 1629 (1972).
- [46] P. Fulde, *Electron correction in molecules and solids*, 3rd ed. (Springer-Berlin, 1995).
- [47] A. R. Williams and U. von Barth, *Theory of the inhomogeneous electron gas - Applications of density functional theory to atoms, molecules and solids* (Pl, 1983).
- [48] R. O. Jones and O. Gunnarsson, *Rev. Mod. Phys.* **61**, 689 (1989).
- [49] J. P. Perdew, K. Burke, and M. Ernzerhof, *Phys. Rev. Lett.* **77**, 3865 (1996).
- [50] J. Perdew, *Electronic Structure of Solids '91* (Akademie-Verlag, Berlin, 1991).
- [51] W. Kohn and A. E. Mattsson, *Phys. Rev. Lett.* **81**, 3487 (1998).
- [52] F. Bechstedt, *Principles of Surface Physics* (Springer-Verlag, Berlin, 2003).
- [53] R. Armiento and A. E. Mattsson, *Phys. Rev. B* **72**, 085108 (2005).
- [54] L. C. de Carvalho, A. Schleife, and F. Bechstedt, *Phys. Rev. B* **84**, 195105 (2011).
- [55] J. Heyd and G. E. Scuseria, *The Journal of Chemical Physics* **121**, 1187 (2004).
- [56] A. D. Becke, *J. Chem. Phys.* **98**, 1372 (1993).
- [57] A. D. Becke, *J. Chem. Phys.* **98**, 5648 (1993).
- [58] J. P. Perdew, M. Ernzerhof, and K. Burke, *J. Chem. Phys.* **105**, 9982 (1996).
- [59] M. Ernzerhof and G. E. Scuseria, *J. Chem. Phys.* **110**, 5029 (1999).
- [60] C. Adamo and V. Barone, *J. Chem. Phys.* **110**, 6158 (1999).
- [61] F. Fuchs, J. Furthmüller, F. Bechstedt, M. Shishkin, and G. Kresse, *Phys. Rev. B* **76**, 115109 (2007).
- [62] J. Paier, M. Marsman, K. Hummer, G. Kresse, I. C. Gerber, and J. G. Ángyán, *J. Chem. Phys.* **124**, 154709 (2006).
- [63] J. Paier, M. Marsman, K. Hummer, G. Kresse, I. C. Gerber, and J. G. Ángyán, *J. Chem. Phys.* **125**, 249901 (2006).
- [64] F. Fuchs, C. Rödl, A. Schleife, and F. Bechstedt, *Phys. Rev. B* **78**, 085103 (2008).
- [65] J. Hubbard, *P. Roy. Soc. Lond. A Mat.* **276**, 238 (1963).
- [66] S. L. Dudarev, G. A. Botton, S. Y. Savrasov, C. J. Humphreys, and A. P. Sutton, *Phys. Rev. B* **57**, 1505 (1998).
- [67] J. Furthmüller, F. Fuchs, and F. Bechstedt, "Theory of indium nitride bulk band structure," (CRC, 2009) Chap. 8, pp. 273–313.
- [68] L. Hedin, *Phys. Rev.* **139**, A796 (8 1965).
- [69] L. Hedin and S. Lundqvist, *Solid State Phys.* **23**, 1 (1969).
- [70] G. Onida, L. Reining, and A. Rubio, *Rev. Mod. Phys.* **74**, 601 (2002).
- [71] F. Bechstedt, F. Fuchs, and G. Kresse, *Phys. Stat. Solidi (b)* **246**, 1877 (2009).
- [72] A. L. Fetter and J. D. Walecka, *Quantum Theory of Many-Particle Systems* (Dover, 2003).
- [73] A. Messiah, *Quantum Mechanics* (Dover, 1999).
- [74] F. Aryasetiawan and O. Gunnarsson, *Reports on Progress in Physics* **61**, 237 (1998).
- [75] J. Schwinger, *Proc. Natl. Acad. Sci. U. S.* **37**, 452 (1951).

- [76] P. C. Martin and J. Schwinger, *Phys. Rev.* **115**, 1342 (1959).
- [77] S. L. Adler, *Phys. Rev.* **126**, 413 (4 1962).
- [78] N. Wiser, *Phys. Rev.* **129**, 62 (1 1963).
- [79] G. Strinati, *Phys. Rev. B* **29**, 5718 (5 1984).
- [80] W. Hanke and L. J. Sham, *Phys. Rev. Lett.* **43**, 387 (7 1979).
- [81] C. Rödl, F. Fuchs, J. Furthmüller, and F. Bechstedt, *Phys. Rev. B* **77**, 184408 (2008).
- [82] R. Goldhahn, A. Winzer, V. Cimalla, O. Ambacher, C. Cobet, W. Richter, N. Esser, J. Furthmüller, F. Bechstedt, H. Lu, and W. J. Schaff, *Superlattice Microst.* **36**, 591 (2004).
- [83] W. G. Schmidt, S. Glutsch, P. H. Hahn, and F. Bechstedt, *Phys. Rev. B* **67**, 085307 (2003).
- [84] A. Schleife, M. Eisenacher, C. Rödl, F. Fuchs, J. Furthmüller, and F. Bechstedt, *Phys. Rev. B* **81**, 245210 (2010).
- [85] A.-B. Chen and A. Sher, *Semiconductor Alloys - Physics and Materials Engineering* (Plenum Press, 1995).
- [86] A. Sher, M. van Schilfgaarde, A.-B. Chen, and W. Chen, *Phys. Rev. B* **36**, 4279 (1987).
- [87] A. Zunger, "First-principles statistical mechanics of semiconductor alloys and intermetallic compounds," in *Statistics and Dynamics of Alloy Phase Transformations*, edited by P. E. A. Turchi and A. Gonis (Plenum Press, New York, 1994) p. 361.
- [88] S.-H. Wei, L. G. Ferreira, and A. Zunger, *Phys. Rev. B* **41**, 8240 (1990).
- [89] L. K. Teles, J. Furthmüller, L. M. R. Scolfaro, J. R. Leite, and F. Bechstedt, *Phys. Rev. B* **62**, 2475 (2000).
- [90] C. Caetano, L. K. Teles, M. Marques, A. Dal Pino, and L. G. Ferreira, *Phys. Rev. B* **74**, 045215 (2006).
- [91] J. W. D. Connolly and A. R. Williams, *Phys. Rev. B* **27**, 5169 (1983).
- [92] A. Schleife, C. Rödl, J. Furthmüller, and F. Bechstedt, *New J. Phys.* **13**, 085012 (2011).
- [93] L. Kantorovich, *Quantum Theory of the Solid State: An Introduction* (Kluwer Academic Publishers, 2004).
- [94] D. R. Hamann, M. Schlüter, and C. Chiang, *Phys. Rev. Lett.* **43**, 1494 (1979).
- [95] D. R. Hamann, *Phys. Rev. B* **40**, 2980 (Aug 1989).
- [96] D. Vanderbilt, *Phys. Rev. B* **41**, 7892 (1990).
- [97] P. E. Blöchl, *Phys. Rev. B* **50**, 17953 (1994).
- [98] D. Hobbs, G. Kresse, and J. Hafner, *Phys. Rev. B* **62**, 11556 (2000).
- [99] M. I. Aroyo, A. Kirov, C. Capillas, J. M. Perez-Mato, and H. Wondratschek, *Acta Cryst.* **A62**, 115 (2006).
- [100] H. J. Monkhorst and J. D. Pack, *Phys. Rev. B* **13**, 5188 (1976).
- [101] A. Riefer, F. Fuchs, C. Rödl, A. Schleife, F. Bechstedt, and Goldhahn, *Phys. Rev. B* **84**, 075218 (2011).
- [102] B. Adolph, V. I. Gavrilenko, K. Tenelsen, F. Bechstedt, and R. Del Sole, *Phys. Rev. B* **53**, 9797 (1996).
- [103] A. Schleife, C. Rödl, F. Fuchs, J. Furthmüller, and F. Bechstedt, *Phys. Rev. B* **80**, 035112 (2009).
- [104] B. Gil, B. O., and A. R. L., *Phys. Rev. B* **52**, R17028 (1995).
- [105] M. Cardona and N. E. Christensen, *Solid State Commun.* **116**, 421 (2000).
- [106] M. Suzuki, T. Uenoyama, and A. Yanase, *Phys. Rev. B* **52**, 8132 (1995).
- [107] K. Kim, W. R. L. Lambrecht, B. Segall, and M. van Schilfgaarde, *Phys. Rev. B* **56**, 7363 (1997).
- [108] A. Belabbes, C. Panse, J. Furthmüller, and F. Bechstedt, to be published.
- [109] L. C. de Carvalho, A. Schleife, F. Fuchs, and F. Bechstedt, *Appl. Phys. Lett.* **97**, 232101 (2010).
- [110] A. Schleife, C. Rödl, F. Fuchs, J. Furthmüller, and F. Bechstedt, *Appl. Phys. Lett.* **91**, 241915 (2007).
- [111] M. Shishkin and G. Kresse, *Phys. Rev. B* **74**, 035101 (7 2006).
- [112] F. Bechstedt, R. D. Sole, G. Cappellini, and L. Reining, *Solid State Commun.* **84**, 765 (1992).
- [113] G. Cappellini, R. Del Sole, L. Reining, and F. Bechstedt, *Phys. Rev. B* **47**, 9892 (4 1993).
- [114] F. D. Murnaghan, *P. Nat. Acad. Sci. USA* **30**, 244 (1944), <http://www.pnas.org/content/30/9/244.short>.
- [115] F. Bechstedt, in *Low-Dimensional Nitride Semiconductors* (Oxford University Press, 2002) Chap. Nitrides as seen by a theorist.
- [116] L. C. de Carvalho, A. Schleife, J. Furthmüller, and F. Bechstedt, *Phys. Rev. B* **85**, 115121 (2012).
- [117] A. Schleife, M. Eisenacher, C. Rödl, F. Fuchs, J. Furthmüller, and F. Bechstedt, *Phys. Rev. B* **81**, 245210 (2010).
- [118] P. Rinke, M. Winkelnkemper, A. Qteish, D. Bimberg, J. Neugebauer, and M. Scheffler, *Phys. Rev. B* **77**, 075202 (2008).
- [119] A. Svane, N. E. Christensen, I. Gorczyca, M. van Schilfgaarde, A. N. Chantis, and T. Kotani, *Phys. Rev. B* **82**, 115102 (2010).

- [120] A. Schleife, C. Rödl, F. Fuchs, J. Furthmüller, F. Bechstedt, P. H. Jefferson, T. D. Veal, C. F. McConville, L. F. J. Piper, A. DeMasi, K. E. Smith, H. Lösch, R. Goldhahn, C. Cobet, J. Zúñiga-Pérez, and V. Muñoz-Sanjosé, *J. Korean Phys. Soc.* **53**, 2811 (2008).
- [121] J. H. Edgar, in *EMIS Datareviews Series*, IEE INSPEC, Vol. 11, edited by J. H. Edgar (1994).
- [122] M. E. Sherwin and T. J. Drummond, *J. Appl. Phys.* **69**, 8423 (1991).
- [123] H. Landolt and R. Börnstein, *Numerical Data and Functional Relationships in Science and Technology*, Vol. III, No. 17a and 22a (Springer-Verlag, Berlin, 1982).
- [124] H. Schulz and K. H. Thiemann, *Solid State Commun.* **23**, 815 (1977).
- [125] Q. Xia, H. Xia, and A. L. Ruoff, *J. Appl. Phys.* **73**, 8198 (1993).
- [126] M. Ueno, M. Yoshida, A. Onodera, O. Shimomura, and K. Takemura, *Phys. Rev. B* **49**, 14 (1994).
- [127] A. García and M. L. Cohen, *Phys. Rev. B* **47**, 4215 (1993).
- [128] C.-Y. Yeh, Z. W. Lu, S. Froyen, and A. Zunger, *Phys. Rev. B* **46**, 10086 (1992).
- [129] Sargent-Welch, Table of Periodic Properties of Elements(1980).
- [130] S. V. Faleev, M. van Schilfgaarde, and T. Kotani, *Phys. Rev. Lett.* **93**, 126406 (2004).
- [131] M. van Schilfgaarde, T. Kotani, and S. Faleev, *Phys. Rev. Lett.* **96**, 226402 (6 2006).
- [132] P. Y. Yu and M. Cardona, *Fundamentals of Semiconductors: Physics and Material Properties* (Springer, 1995).
- [133] F. Bechstedt, F. Fuchs, and J. Furthmüller, *Phys. Stat. Solidi (a)* **207**, 1041 (2010).
- [134] L. P. Bouckaert, R. Smoluchowski, and E. Wigner, *Phys. Rev.* **50**, 58 (1936).
- [135] E. I. Rashba, *Fiz. Tverd. Tela* **1**, 407 (1959).
- [136] W. Harrison, *Electronic Structure and the Properties of Solids* (Dover Pub., New York, 1989).
- [137] S.-H. Wei and A. Zunger, *Phys. Rev. B* **37**, 8958 (1988).
- [138] C. Persson and A. Zunger, *Phys. Rev. B* **68**, 073205 (2003).
- [139] P. D. C. King, T. D. Veal, P. H. Jefferson, S. A. Hatfield, L. F. J. Piper, F. McConville, F. Fuchs, J. Furthmüller, F. Bechstedt, H. Lu, and W. J. Schaff, *Phys. Rev. B* **77**, 045316 (2008).
- [140] J. Renard, G. Tourbot, D. Sam-Giao, C. Bougerol, B. Daudin, and B. Gayral, *Appl. Phys. Lett.* **97**, 081910 (2010).
- [141] V. Consonni, M. Knelangen, U. Jahn, A. Trampert, L. Geelhaar, and H. Riechert, *Appl. Phys. Lett.* **95**, 241910 (2009).
- [142] F. Bechstedt and P. Käckell, *Phys. Rev. Lett.* **75**, 2180 (1995).
- [143] A. Schleife, F. Fuchs, C. Rödl, J. Furthmüller, and F. Bechstedt, *Appl. Phys. Lett.* **94**, 012104 (2009).
- [144] W. R. Frensley and H. Kroemer, *J. Vac. Sci. Technol.* **13**, 810 (1976).
- [145] J. Tersoff, *Phys. Rev. B* **30**, 4874 (1984).
- [146] B. Höffling, A. Schleife, F. Fuchs, C. Rödl, and F. Bechstedt, *Appl. Phys. Lett.* **97**, 032116 (2010).
- [147] F. Bechstedt and R. Enderlein, *Semiconductor Surfaces and Interfaces* (Akademie-Verlag, Berlin, 1998).
- [148] J. O. MacCaldin, T. C. MacGill, and C. A. Mead, *Phys. Rev. Lett.* **36**, 56 (1976).
- [149] C. F. Shih, N. C. Chen, P. H. Chang, and K. S. Liu, *Jpn. J. Appl. Phys.* **44**, 7892 (2005).
- [150] P. D. C. King, T. D. Veal, P. H. Jefferson, P. C. F. McConville, T. Wang, P. J. Parbrook, H. Lu, and W. J. Schaff, *Appl. Phys. Lett.* **90**, 132105 (2007).
- [151] M. Murayama and T. Nakayama, *Phys. Rev. B* **49**, 4710 (1994).
- [152] C.-Y. Yeh, S. H. Lu, Wei, and A. Zunger, *Phys. Rev. B* **50**, 2715 (1994).
- [153] G. M. Dalpian and S. H. Wei, *Phys. Rev. Lett.* **93**, 216401 (2004).
- [154] C. Stampfl and C. G. V. de Walle, *Phys. Rev. B* **57**, R15052 (1998).
- [155] J. Majewski and P. Vogl, *J. Nitride Semicond. Res.* **3**, 21 (1998).
- [156] J. A. Majewski and M. Städele, *Mat. Res. Soc. Symp. Proc.* **482**, 917 (1997).
- [157] Z. Z. Bandić, T. C. MacGill, and Z. Ikonić, *Phys. Rev. B* **56**, 3564 (1997).
- [158] A. Belabbes, L. C. de Carvalho, A. Schleife, and F. Bechstedt, *Phys. Rev. B* **84**, 125108 (2011).
- [159] C. Mietze, M. Landmann, E. Rauls, H. Machhadani, S. sakr, M. Tchernycheva, F. H. Julien, W. G. schmidt, K. Lischka, and D. J. As, *Phys. Rev. B* **83**, 195301 (2011).
- [160] P. G. Moses, M. Miao, Q. Yan, and C. G. Van de Walle, *J. Chem. Phys.* **134**, 084703 (2011).
- [161] A. Alkauskas, P. Broqvist, F. Devynck, and A. Pasquarello, *Phys. Rev. Lett.* **101**, 106802 (2008).
- [162] C. Panse, D. Kriegner, and F. Bechstedt, *Phys. Rev. B* **84**, 075217 (2011).

- [163] M. Röppischer, R. Goldhahn, G. Rossbach, P. Schley, C. Cobet, N. Esser, T. Schupp, K. Lischka, and D. J. As, *J. Appl. Phys.* **106**, 076104 (2009).
- [164] J. Schörmann, D. J. As, K. Lischka, P. Schley, R. Goldhahn, S. F. Li, W. Löffler, M. Hetterich, and H. Kalt, *Appl. Phys. Lett.* **89**, 261903 (2006).
- [165] F. Litimein, B. Bouhafs, G. Nouet, and P. Ruterana, *phys. stat. sol. (b)* **243**, 1577 (2006).
- [166] J. Furthmüller, P. H. Hahn, F. Fuchs, and F. Bechstedt, *Phys. Rev. B* **72**, 205106 (2005).
- [167] A. Schleife, F. Fuchs, C. Rödl, J. Furthmüller, and F. Bechstedt, *Phys. Status Solidi B* **246**, 2150 (2009).
- [168] I. Vurgaftman and J. R. Meyer, *J. Appl. Phys.* **94**, 3675 (2003).
- [169] J. P. Desclaux, *Atom. Data Nucl. Data* **12**, 311 (1973).
- [170] M. Cardona, N. E. Christensen, and G. Fasol, *Phys. Rev. B* **38**, 1806 (1988).
- [171] S. L. Chuang and C. S. Chang, *Phys. Rev. B* **54**, 2491 (1996).
- [172] A. Punya and W. R. L. Lambrecht, *Phys. Rev. B* **85**, 195147 (2012).
- [173] R. Enderlein and N. J. M. Horing, *Fundamentals of Semiconductor Physics and Devices* (World Scientific Publishing, 1997).
- [174] G. Dresselhaus, *Phys. Rev.* **100**, 580 (1955).
- [175] M. Cardona, N. E. Christensen, and G. Fasol, *Phys. Rev. Lett.* **56**, 2831 (1986).
- [176] M. P. Surh, M.-F. Li, and S. G. Louie, *Phys. Rev. B* **43**, 4286 (1991).
- [177] L. C. Lew Yan Voon, M. Willatzen, M. Cardona, and N. E. Christensen, *Phys. Rev. B* **53**, 10703 (1996).
- [178] J. Wu, W. Walukiewicz, W. Shan, K. M. Yu, J. W. Ager, E. E. Haller, H. Lu, and W. J. Schaff, *Phys. Rev. B* **66**, 201403 (2002).
- [179] S. P. Fu and Y. F. Chen, *Appl. Phys. Lett.* **85**, 1523 (2004).
- [180] A. V. Rodina and B. K. Meyer, *Phys. Rev. B* **64**, 245209 (2001).
- [181] S. Shokhovets, G. Gobsch, and O. Ambacher, *Appl. Phys. Lett.* **86**, 161908 (2005).
- [182] D. Fritsch, H. Schmidt, and M. Grundmann, *Phys. Rev. B* **67**, 235205 (2003).
- [183] D. Fritsch, H. Schmidt, and M. Grundmann, *Phys. Rev. B* **69**, 165204 (2004).
- [184] L. E. Ramos, L. K. Teles, L. M. R. Scolfaro, J. L. P. Castineira, A. L. Rosa, and J. R. Leite, *Phys. Rev. B* **63**, 165210 (2001).
- [185] M. Fanciulli, T. Lei, and T. D. Moustakas, *Phys. Rev. B* **48**, 15144 (1993).
- [186] P. Schley, C. Napierala, R. Goldhahn, G. Gobsch, J. Schörmann, D. J. As, K. Lischka, M. Feneberg, K. Thonke, F. Fuchs, and F. Bechstedt, *Phys. Status Solidi C* **5**, 2342 (2008).
- [187] M. Goano, E. Bellotti, E. Ghillino, G. Ghione, and K. F. Brennan, *J. Appl. Phys.* **88**, 6467 (2000).
- [188] Y. C. Yeo, T. C. Chong, and M. F. Li, *J. Appl. Phys.* **83**, 1429 (1998).
- [189] J. S. Im, A. Moritz, F. Steuber, V. Härle, F. Scholz, and A. Hangleiter, *Appl. Phys. Lett.* **70**, 631 (1997).
- [190] M. Steube, K. Reimann, D. Fröhlich, and S. J. Clarke, *Appl. Phys. Lett.* **71**, 948 (1997).
- [191] B. Rezaei, A. Asgari, and M. Kalafi, *Physica B* **371**, 107 (2006).
- [192] M. Goiran, M. Millot, J.-M. Pomirol, I. Gherasoiu, W. Walukiewicz, and J. Leotin, *Appl. Phys. Lett.* **96**, 052117 (2010).
- [193] J. M. Cowley, *J. Appl. Phys.* **21**, 24 (1950).
- [194] J. A. Chan, J. Z. Liu, and A. Zunger, *Phys. Rev. B* **82**, 045112 (2010).
- [195] M. Lopuszyński and J. Majewski, *Phys. Rev. B* **85**, 035211 (2012).
- [196] J. Z. Liu and A. Zunger, *Phys. Rev. B* **77**, 205201 (May 2008).
- [197] M. Sanati, G. L. W. Hart, and A. Zunger, *Phys. Rev. B* **68**, 155210 (2003).
- [198] J. Adhikari and D. A. Kofke, *J. Appl. Phys.* **95**, 6129 (2004).
- [199] L. Vegard, *Z. Phys.* **5**, 17 (1921).
- [200] E. Sakalauskas, H. Behmenburg, C. Hums, P. Schley, G. Rossbach, C. Giesen, M. Heuken, H. Kalisch, R. H. Jansen, J. Bläsing, A. Dadgar, A. Krost, and R. Goldhahn, *J. Phys. D: Appl. Phys.* **43**, 365102 (2010).
- [201] A. F. Wright and J. S. Nelson, *Phys. Rev. B* **51**, 7866 (1995).
- [202] K. Osamura, S. Naka, and Y. Murakami, *J. Appl. Phys.* **46**, 3432 (1975).
- [203] I. Gorczyca, S. P. Łepkowski, T. Suski, N. E. Christensen, and A. Svane, *Phys. Rev. B* **80**, 075202 (2009).
- [204] S. Nakamura and G. Fasol, *The blue laser diode: GaN based light emitters and lasers* (Springer, Berlin, 1997).
- [205] S. Chichibu, T. Azuhata, T. Sota, and S. Nakamura, *Appl. Phys. Lett.* **70**, 2822 (1997).
- [206] L. K. Teles, L. M. R. Scolfaro, J. R. Leite, J. J. Furthmüller, and F. Bechstedt, *J. Appl. Phys.* **92**, 7109 (2002).

- [207] M. Ferhat and F. Bechstedt, *Phys. Rev. B* **65**, 075213 (2002).
- [208] M. Marques, L. K. Teles, L. M. R. Scolfaro, J. R. Leite, J. Furthmüller, and F. Bechstedt, *Appl. Phys. Lett.*, 890(2003).
- [209] P. G. Moses and C. G. V. de Walle, *Appl. Phys. Lett.*, 021908(2010).
- [210] R. R. Pela, C. Caetano, M. Marques, L. G. Ferreira, J. Furthmüller, and L. K. Teles, *Appl. Phys. Lett.* **98**, 151907 (2011).
- [211] P. Hohenberg and W. Kohn, *Phys. Rev.* **136**, B864 (1964).
- [212] W. Kohn and L. J. Sham, *Phys. Rev.* **140**, A1133 (1965).
- [213] W. Mönch, *Semiconductor Surfaces and Interfaces* (Springer, Berlin, 2001).
- [214] F. Flores and C. Tejedor, *J. Phys. C Solid State* **12**, 731 (1979).
- [215] C. Tejedor and F. Flores, *J. Phys. C Solid State* **11**, L19 (1977).
- [216] V. Popescu and A. Zunger, *Phys. Rev. Lett.* **104**, 236403 (2010).
- [217] P. D. C. King, T. D. Veal, C. F. McConville, F. Fuchs, J. Furthmüller, F. Bechstedt, J. Schörmann, D. J. As, K. Lischka, H. Lu, and W. J. Schaff, *Phys. Rev. B* **77**, 115213 (2008).
- [218] I. Gorczyca, T. Suski, N. E. Christensen, and A. Svane, *Phys. Rev. B* **83**, 153301 (2011).
- [219] M. Ferhat, J. Furthmüller, and F. Bechstedt, *Appl. Phys. Lett.* **80**, 1394 (2002).
- [220] L. G. Ferreira, M. Marques, and L. K. Teles, *Phys. Rev. B* **78**, 125116 (2008).
- [221] H. Naoi, K. Fujiwara, S. Takado, M. Kurouchi, D. Muto, T. Araki, H. Na, and Y. Nanishi, *J. Electron. Mater.* **36**, 1313 (2007).
- [222] S. Pereira, M. R. Correia, T. Monteiro, E. Pereira, E. Alves, A. D. Sequeira, and N. Franco, *Appl. Phys. Lett.*, 2137(2001).
- [223] M. D. McCluskey, C. G. V. de Walle, L. T. Romano, B. S. Krusor, and N. M. Johnson, *J. Appl. Phys.* **93**, 4340 (2003).
- [224] K. P. O'Donnell, I. Fernandez-Torrente, P. R. Edwards, and R. W. Martin, *Proceedings of the First ONR International Indium Nitride Workshop, J. Crystal Growth* **269**, 100 (2004).
- [225] F. Scholz, J. Off, A. Sohmer, V. Syganow, A. Dörnen, and O. Ambacher, *J. Crystal Growth* **189-190**, 8 (1998).
- [226] W. Shan, W. Walukiewicz, E. E. Haller, B. D. Little, J. J. Song, M. D. McCluskey, N. M. Johnson, Z. C. Feng, M. Schurman, and R. A. Stall, *J. Appl. Phys.* **84**, 4452 (1998).
- [227] T. Takeuchi, H. Takeuchi, S. Sota, H. Sakai, H. Amano, and I. Akasaki, *Jpn. J. Appl. Phys.* **36**, L177 (1997).
- [228] C. Wetzel, T. Takeuchi, S. Yamaguchi, H. Katoh, H. Amano, and I. Akasaki, *Appl. Phys. Lett.* **73**, 1994 (1998).
- [229] M.-H. Kim, J.-K. Cho, I.-H. Lee, and S.-J. Park, *Phys. Stat. Solidi (a)* **176**, 269 (1999).
- [230] K. P. O'Donnell, J. F. W. Mosselmanns, R. W. Martin, S. Pereira, and M. E. White, *J. Phys.: Condens. Matter.* **13**, 6977 (2001).
- [231] R. Goldhahn, P. Schley, A. Winzer, G. Gobsch, V. Cimalla, O. Ambacher, M. Rakel, C. Cobet, N. Esser, H. Lu, and W. Schaff, *Phys. Stat. Solidi (a)* **203**, 42 (2006).
- [232] E. Iliopoulos, A. Adikimenakis, C. Giesen, M. Heuken, and A. Georgakilas, *Appl. Phys. Lett.* **92**, 191907 (2008).
- [233] R. E. Jones, R. Broesler, K. M. Yu, I. J. W. Ager, E. E. Haller, W. Walukiewicz, X. Chen, and W. J. Schaff, *J. Appl. Phys.*, 123501(2008).
- [234] W. Walukiewicz, S. X. Li, J. Wu, K. M. Yu, J. W. Ager, E. E. Haller, H. Lu, and W. J. Schaff, *Proceedings of the First ONR International Indium Nitride Workshop, J. Crystal Growth* **269**, 119 (2004).
- [235] J.-F. Carlin, C. Zellweger, J. Dorsaz, S. Nicolay, G. Christmann, E. Feltn, R. Butt, and N. Grandjean, *Phys. Stat. Solidi (b)* **242**, 2326 (2005).
- [236] T. Onuma, S. Chichibu, Y. Uchinuma, T. Sota, S. Yamaguchi, S. Kamiyama, H. Amano, and I. Akasaki, *J. Appl. Phys.* **94**, 2449 (2003).
- [237] S. Albrecht, L. Reining, R. Del Sole, and G. Onida, *Phys. Rev. Lett.* **80**, 4510 (5 1998).
- [238] L. X. Benedict, E. L. Shirley, and R. B. Bohn, *Phys. Rev. Lett.* **80**, 4514 (5 1998).
- [239] M. Rohlfing and S. G. Louie, *Phys. Rev. Lett.* **81**, 2312 (9 1998).
- [240] P. H. Hahn, W. G. Schmidt, and F. Bechstedt, *Phys. Rev. Lett.* **88**, 016402 (12 2001).
- [241] M. Bruno, M. Palummo, A. Marini, R. D. Sole, and S. Ossicini, *Phys. Rev. Lett.* **98**, 036807 (2007).
- [242] M. Rohlfing and S. G. Louie, *Phys. Rev. B* **62**, 4927 (2000).
- [243] P. Yu and M. Cardona, *Fundamentals of Semiconductors* (Springer-Verlag, Berlin, 1999).
- [244] R. Laskowski, N. E. Christensen, G. Santi, and C. Ambrosch-Draxl, *Phys. Rev. B* **72**, 035204 (2005).
- [245] L. Benedict, T. Wethkamp, K. Wilmers, C. Cobet, N. Esser, E. Shirley, W. Richter, and M. Cardona, *Solid State Commun.*

- 112, 129 (1999).
- [246] L. X. Benedict and E. L. Shirley, *Phys. Rev. B* **59**, 5441 (2 1999).
- [247] F. Bechstedt, K. Seino, P. H. Hahn, and W. G. Schmidt, *Phys. Rev. B* **72**, 245114 (2005).
- [248] P. H. Hahn, K. Seino, W. G. Schmidt, J. Furthmüller, and F. Bechstedt, *Phys. Status Solidi B* **242**, 2720 (2005).
- [249] P. Schley, R. Goldhahn, A. T. Winzer, G. Gobsch, V. Cimalla, O. Ambacher, M. Rakel, C. Cobet, N. Esser, H. Lu, and W. J. Schaff, *Phys. Status Solidi B* **243**, 1572 (2006).
- [250] P. Schley, R. Goldhahn, A. T. Winzer, G. Gobsch, V. Cimalla, O. Ambacher, H. Lu, M. Schaff, W. J. and Kurouchi, Y. Nishi, M. Rakel, and N. Cobet, C. and Esser, *Phys. Rev. B* **75**, 205204 (2007).
- [251] E. Sakalauskas, H. Behmenburg, P. Schley, G. Gobsch, C. Giesen, H. Kalisch, R. H. Jansen, M. Heuken, and R. Goldhahn, *Phys. Status Solidi A* **208**, 1517 (2011).
- [252] C. Buchheim, R. Goldhahn, M. Rakel, C. Cobet, N. Esser, U. Rossow, D. Fuhrmann, and A. Hangleiter, *Phys. Status Solidi B* **242**, 2610 (2005).
- [253] P. Schley, J. Räthel, E. Sakalauskas, G. Gobsch, M. Wieneke, J. Bläsing, A. Krost, G. Koblemüller, J. S. Speck, and R. Goldhahn, *Phys. Stat. Solidi (a)* **207**, 1062 (2010).
- [254] M. Röppischer, *Optische Eigenschaften von Aluminium-Galliumnitride-Halbleitern*, Ph.D. thesis, TU-Berlin (2011).
- [255] M. Feneberg, M. Röppischer, C. Cobet, N. Esser, N. B., K. Thonke, M. Bickermann, R. M. E., and R. Goldhahn (Unpublished).
- [256] C. Cobet, R. Goldhahn, W. Richter, and N. Esser, *Phys. Status Solidi B* **246**, 1440 (2009).
- [257] G. Rossbach, M. Röppischer, P. Schley, G. Gobsch, C. Werner, C. Cobet, N. Esser, A. Dadgar, M. Wieneke, A. Krost, and R. Goldhahn, *Phys. Status Solidi B* **247**, 1679 (2010).
- [258] G. Grosso and G. Pastori Parravicini, *Solid State Physics* (Academic Press, Amsterdam, San Diego, 2000).
- [259] E. Sakalauskas, O. Tuna, A. Kraus, H. Bremers, U. Rossow, C. Giesen, M. Heuken, A. Hangleiter, G. Gobsch, and R. Goldhahn, *Phys. Status Solidi B* **247**, 1679 (2012).
- [260] D. E. Aspnes, *Phys. Rev. Lett.* **28**, 168 (1972).
- [261] G. Rossbach, M. Feneberg, M. Röppischer, C. Werner, N. Esser, C. Cobet, T. Meisch, K. Thonke, A. Dadgar, B. J., A. Krost, and G. R., *Phys. Rev. B* **83**, 195202 (2011).
- [262] A. V. Rondina, M. Dietrich, A. Göldner, L. Eckey, A. Hoffman, A. L. Efros, M. Rosen, and B. K. Meyer, *Phys. Rev. B* **64**, 115204 (2001).
- [263] P. Schley, R. Goldhahn, G. Gobsch, M. Feneberg, K. Thonke, X. Wang, and A. Yoshikawa, *phys. stat. sol. (b)* **246**, 1177 (2009).
- [264] S. Shokhovets, R. Goldhahn, G. Gobsch, S. Piekh, R. Lantier, A. Rizzi, V. Lebedev, and W. Richter, *J. Appl. Phys* **94**, 307 (2003).

My Curriculum Vitae

• Personal Information

- **Nome:** Luiz Cláudio de Carvalho
- **Birth information:** 31/07/1970 - São João del Rei - MG
- **Residential address:** Charlottenstr. 23/CE02 - Humboldthaus, 07749, Jena - Germany
- **Phone:** +49 (0) 3641 930711
- **Professional Address:** Institut für Festkörpertheorie - IFTO Max-Wien-Platz,1 07743, Jena - Germany
- **Phone:** +49 (0) 3641 947163
- **e-mail:** lccfisica@gmail.com or luiz-claudio.de-carvalho@uni-jena.de

• Formal Education

- **2009 - 2012:** Phd in physics, Friedrich Schiller Universität-Jena - Germany
Advisor: Prof. Dr. Friedhelm Bechstedt
Thesis: Modeling of III-nitride alloys by *ab-initio* methods
- **2001 - 2004:** Master in physics, Federal University of São João del Rei - Brazil
Advisor: Prof. Dr. José Luiz Aarestrup Alves
Master-Thesis: Structural, electronic, and optical properties of semiconducting polymers
- **1995 - 2000:** Graduation in physics,
- **1992 - 1994:** High education, Escola Estadual Dr. Garcia de Lima, São João del Rei - Brazil
- **1980 - 1987:** Primary and secondary education, Escola Estadual Cônego Osvaldo Lustosa

• Professional Experience

- **2005 - 2009:** Collaborator, Position: Research, Federal University of São João del Rei - Brazil
- **2004 - 03/2009:** Lectures: President Antônio Carlos University - Brazil

• Languages

- **Portuguese:** Understand fluent, speak fluent, write fluent, read fluent
- **English:** Understand fluent, speak functional, write functional, read fluent
- **French:** Understand functional, read functional
- **Spanish:** Understand functional, speak functional, read functional

• Awards

- **1999:** Honra ao Mérito - scientific initiation - Vacancies and substitutional impurities on III-Nitrides - CNPq

Ehrenwörtliche Erklärung

Hiermit erkläre ich ehrenwörtlich, dass ich die vorliegende Arbeit selbständig ohne unzulässige Hilfe Dritter und ohne Benutzung anderer als der angegebenen Hilfsmittel und Literatur angefertigt habe. Die aus anderen Quellen direkt oder indirekt übernommenen Daten und Konzepte sind unter Angabe der Quelle gekennzeichnet.

Bei der Auswahl und Auswertung folgenden Materials haben mir die nachstehend aufgeführten Personen in der jeweils beschriebenen Weise unentgeltlich geholfen:

1. Prof. Dr. sc. nat. Friedhelm Bechstedt (Betreuer)
2. Dr. rer. nat. Jürgen Furthmüller (Koautor von Publikation)
3. Dr. rer. nat. André Schleife (Koautor von Publikation)

Weitere Personen waren an der inhaltlich-materiellen Erstellung der vorliegenden Arbeit nicht beteiligt. Insbesondere habe ich hierfür nicht die entgeltliche Hilfe von Vermittlungs- bzw. Beratungsdiensten (Promotionsberater oder anderer Personen) in Anspruch genommen. Niemand hat von mir unmittelbar oder mittelbar geldwerte Leistungen für Arbeiten erhalten, die im Zusammenhang mit dem Inhalt der vorgelegten Dissertation stehen.

Die Arbeit wurde bisher weder im In- noch im Ausland in gleicher oder ähnlicher Form einer anderen Prüfungsbehörde vorgelegt.

Die geltende Promotionsordnung der Physikalisch-Astronomischen Fakultät ist mir bekannt.

Ich versichere ehrenwörtlich, dass ich nach bestem Wissen die reine Wahrheit gesagt und nichts verschwiegen habe.

Jena, den 4. Dezember 2012

Acknowledgments

Firstly my acknowledgments is to God that make everything possible in our life.

Secondly, my advisor, Prof. Dr. Friedhelm Bechstedt, for the opportunity to do my PhD in Germany, his efforts for everything be right (financial support, home, computers at work, etc.) was my motivation to this work. Concomitantly, his discussions, ideas and teachings, owing his wide theoretical experience on semiconductors, especially nitrides, and the theoretical methods were very important to me.

Also I wish to acknowledge and to say THANK YOU VERY MUCH for all people that directly or indirectly contributed to this work during the three and half years of work, especially:

- Simeon Sauer that was my tutor when I arrived in Jena;
- my former advisors Prof. Dr. José Luiz Aarestrup Alves and Prof. Dr. Horácio Wagner Leite Alves for discussions and friendship;
- my mentor within the EU ITN RAINBOW Prof. Dr. Rudiger Goldhahn for discussions;
- Sylvia Hennig, Heike Möckel and Marion Fiedler for their support in bureaucracies and computers, also their friendship;
- all members that belonged and still belong to our group (IFTO, FSU-Jena);
- European Union (Marie Curie Foundation), Deutsch Forschungsgemeinschaft (SRK 1523) and Friedrich Schiller Universität for the financial support by means of scholarships.

I am very grateful to Dr. André Schleife for productive discussions and important help in the analysis of results and also, how to handle the most of computational codes used in this work.

My friend Dr. Abderrezak Belabbes (Abdo) for the productive and long discussions about group-III nitrides, methods, and aid in the difficult moments.

I would like to thank so much Andreas Schrön for all discussions and supports: german language, programming, fill out documents and the most diverse situations during my life in Germany.

Finally, my sincerely acknowledgment is especially to my wife Tânia, my parents Galdino e Zenite, and my sisters Cláudia Luiza and Cátia Regina; they are the stem of my life.